NOTE TO USERS

Speed-Sensorless Torque Control of Induction Motors for Hybrid Electric Vehicles

Tianjun Fu

A Thesis

in

The Department

of

Mechanical and Industrial Engineering

Presented in Partial Fulfillment of the Requirements
for the Degree of Master of Applied Science at
Concordia University
Montreal, Quebec, Canada

August 2005

Your file Votre référence
ISBN: 0-494-10263-2
Our file Notre référence
ISBN: 0-494-10263-2

Abstract

Speed-Sensorless Torque Control of Induction Motors for Hybrid Electric Vehicles

Tianjun Fu

Hybrid Electric Vehicles (HEVs) are exciting new additions to the car markets since they combine the best features of conventional and electric cars to improve environmental performance and reduce fuel consumption. HEVs get their driving power from both an internal combustion engine and an electric motor. Many researches have demonstrated the induction motor is one of the right electric motor candidates for the most HEVs due to its low cost, robustness and low maintenance.

The objective of this research work is to develop a new speed-sensorless control method for induction motors to optimize torque response and improve robustness in order to meet the requirement of HEV applications. The proposed new control method is based on Sliding-Mode Control (SMC) combined with Space Vector Modulation (SVM) technique. The SMC contributes to the robustness of induction motor drives, and the SVM improves the torque, flux, and current steady-state performance by reducing the ripple. The Lyapunov direct method is used to ensure the reaching and sustaining of sliding-mode and stability of the control system. A sliding-mode observer is proposed to estimate the rotor flux and speed. Computer simulation results show that the proposed control scheme owns very good dynamic characteristics, high accuracy in torque tracking to various reference signals and strong robustness to external load disturbances.

Acknowledgements

I would like to express my sincere appreciation to my supervisor, Dr. Wen-Fang Xie, for her invaluable help, patience, guidance and support during all stages of this research work.

I would also like to thank the System Analyst Group and the Technical Support Group of the Department of Mechanical and Industrial Engineering at Concordia University for their continuous help and support. In particular I would like to mention a technician, Mr. Gilles Huard.

Special thanks go to Mr. Dan Li, who works in the Department of Electrical and Computer Engineering, for his help in the experiment setup.

Thanks also go to my colleagues, friends and fellow students for their help and useful discussions during this work.

Finally, I express my deepest gratitude to my parents, wife, brothers and other family members. Without their love, support and encouragement, I would never have reached this level.

Table of Contents

List of Figures

List of Tables

List of Abbreviations and Symbols

DTC	Direct torque control
EV	Electric vehicle
FOC	Field oriented control
FSMC	Fuzzy sliding-mode control
HEV	Hybrid electric vehicle
ICE	Internal combustion engine
IGBT	Insulated gate bipolar transistor
MRAS	Model-reference adaptive system
NSFC	Nonlinear state feedback control
PMSM	Permanent magnet synchronous motor
PWM	Pulse width modulation
SRM	Switched reluctance motor
SMC	Sliding-mode control
SVM	Space vector modulation
THD	Total harmonic distortion
VSI	Voltage source inverter
i_a , i_b, i_c	Stator current in a three-phase system (A)
i_α , i_β	Stator current in the (α, β) system (A)
$\hat{i}_\alpha$, $\hat{i}_\beta$	Estimated stator current in the (α, β) system (A)

$\bar{i}_\alpha$, $\bar{i}_\beta$	Estimation error of stator current in the (α, β) system (A)
i_d , i_q	Stator current in the (d, q) system (A)
$\boldsymbol{i}_r$	Rotor current space vector
i_{ra} , i_{rb} , i_{rc}	Rotor current in a three-phase system (A)
$\boldsymbol{i}_s$	Stator current space vector
ψ_α , ψ_β	Rotor flux in the (α, β) system (Wb)
$\hat{\psi}_\alpha$, $\hat{\psi}_\beta$	Estimated rotor flux in the (α, β) system (Wb)
$\overline{\psi}_\alpha$, $\overline{\psi}_\beta$	Estimation error of the rotor flux in the (α, β) system (Wb)
ψ_d , ψ_q	Rotor flux in the (d, q) system (Wb)
$\boldsymbol{\psi}_r$	Rotor flux space vector
ψ_{ref}	Rotor reference flux (Wb)
$\boldsymbol{\psi}_s$	Stator flux space vector
B	Friction coefficient ($\mathrm{N \cdot m \cdot s/rad}$)
J	Inertia of the rotor ($\mathrm{N \cdot m \cdot s^2}$)
L_s	Stator inductance (H)
L_r	Rotor inductance (H)
L_m	Mutual inductance (H)
P	The number pole pairs
u_a , u_b , u_c	Stator voltage in a three-phase system (V)
u_{oN}	Neutral point potential of the motor (V)

$u_{Li},\ i=1,2,3$	Pole voltages of the inverter (V)
$\boldsymbol{u}_s$	Stator voltage space vector
$\boldsymbol{u}_i$, i=0, 1, …, 7	Voltage vectors corresponding to S_i
V_{dc}	DC-link voltage of the inverter (V)
ω	Rotor angle velocity (rad/sec)
$\hat{\omega}$	Estimated rotor angle velocity (rad/sec)
ω_0	The selected constant for $\hat{\omega}$
$\overline{\omega}$	Estimation error of the rotor angle velocity (rad/sec)
ω_{eq}	The equivalent value of rotor angle velocity (rad/sec)
R_r	Rotor resistance (Ω)
R_s	Rotor resistance (Ω)
S_i, i=0, 1, …, 7	Active switch states of the inverter
s_1, s_2	Sliding surfaces
s_ω, s_μ	Nonlinear functions of the stator current errors
T	Torque of the motor ($\mathrm{N}\cdot\mathrm{m}$)
T_L	Load torque of the motor ($\mathrm{N}\cdot\mathrm{m}$)
T_{ref}	Reference torque of the motor ($\mathrm{N}\cdot\mathrm{m}$)
T_i, i=0, 1, …, 7	The turn-on times of the voltage vectors $\boldsymbol{u}_i$ (sec)
T_s	Sampling time of the control system (sec)
t_i, i=1, 2, …, 6	The required time periods to spend in a T_s (sec)
τ	Rotor time constant
τ_f	Time constant of the low-pass filter

σ	Total leakage coefficient of the motor
μ	Auxiliary variable of the SMC observer
μ_{eq}	The equivalent value of the auxiliary variable
μ_0	The selected constant for μ

Chapter 1
Literature Review and Objectives

Environmental issues and oil crisis compel to develop clean, efficient vehicles for urban transportation. The Electric Vehicle (EV) is the first consideration for its zero emissions. However, the source of energy and battery technologies level in EVs hindered the EVs development. From 1990s, a number of auto industries have started to develop Hybrid Electric Vehicles (HEVs) to overcome the battery and range problem of pure electric vehicles [1]. Now HEVs are becoming an increasingly popular alternative to conventional vehicles due to the potential for lower energy consumption and lower pollutant emissions [2-7]. The power train of a HEV combines both the Internal Combustion Engine (ICE) of a conventional vehicle and the electric motor of an EV, so the HEV owns the benefits of the EV with the features of a gas combustion engine.

Many researches have been done on modeling, control and monitoring of HEV power systems [8-12]. As a result of these researches, the induction motor is considered as the right electric motor candidate for the most HEVs due to its low cost, robustness and low maintenance.

1.1 HEV background

According to the statistic data of greenhouse gas emission, 13.4% of Canada's total emissions are due to transportation sources mainly from vehicles. America and Europe issued emissions legislation for passenger cars [13], and the standards are becoming

stringent. As consumers and the government continue to demand increased fuel economy and reduced emissions from their vehicles, auto manufactures are increasingly exploring new technologies to meet this demand. One solution under consideration is that of HEVs. Compared with the conventional ICE vehicles, the HEV has significant fuel economy and lower emissions [14-17].

In a HEV system, the ICE and the electric motor are optimally controlled to increase fuel efficiency. When powerful acceleration is needed, the high-output electric motor and the ICE generate optimum power. Therefore, the vehicle output is efficiently improved, and the vehicle can have smooth, seamless and powerful running performance. The acceleration sensation comparison of the Toyota HEVs (THS II and Prius) and a conventional vehicle is shown in Figure 1.1.

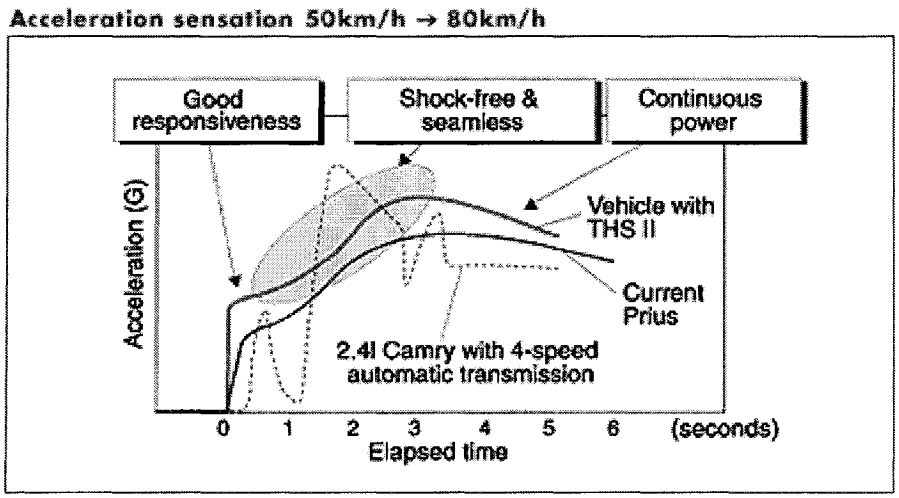

Figure 1.1: HEVs' acceleration sensation [18]

Currently, the following three major types of hybrid system are being used in the hybrid vehicles: series, parallel, and series/parallel hybrid systems. The most common types of HEV are the parallel and the series/parallel types. A series/parallel HEV system is shown in Figure 1.2.

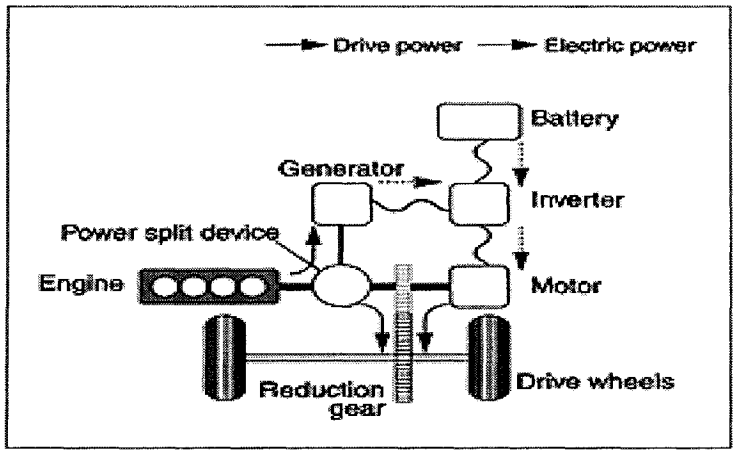

Figure 1.2: Series/parallel HEV system [18]

A parallel HEV control system scheme is shown as Figure 1.3.

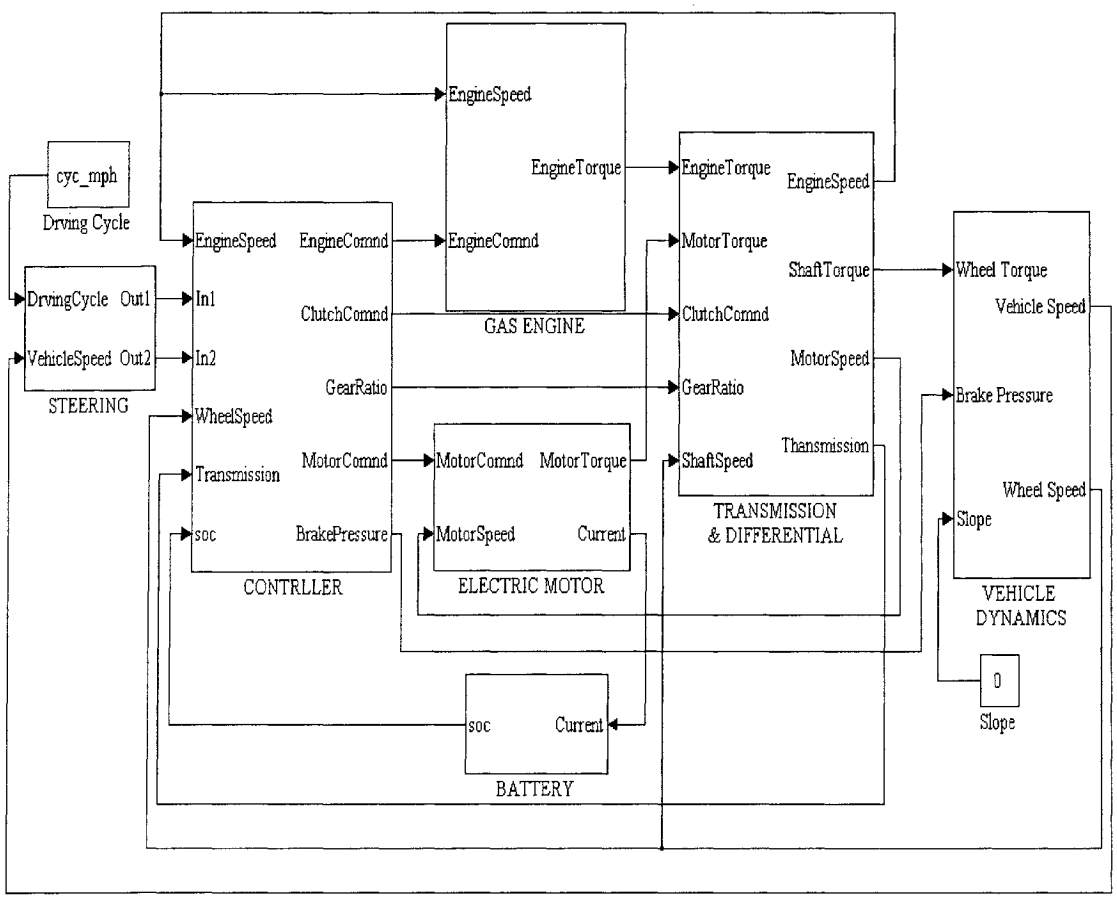

Figure 1.3: A HEV control system scheme [19]

1.2 Induction motor control for HEV applications

Motors are the "work horses" of HEV drive systems. In a HEV, an electric motor converts electrical energy from the energy storage unit to mechanical energy that drives the wheels of the vehicle. Unlike a traditional vehicle, where the engine must "ramp up" before full torque can be provided, an electric motor provides full torque at low speeds. This characteristic gives the vehicle excellent "off the line" acceleration. Important characteristics of a HEV motor include good drive control and fault tolerance, as well as low noise and high efficiency [12]. Other characteristics include flexibility in relation to voltage fluctuations and, of course, acceptable mass production costs.

Currently, front-running motors for HEV applications mainly include Permanent Magnet Synchronous Motors (PMSMs) and Switched Reluctance Motors (SRMs). Table 1.1 shows the electric motors currently used in some HEVs [20-24].

Table 1.1: Electric motors used in HEVs

HEV Model	Manufacturer	Electric Motor			
		Type	Power (kW)	Voltage (V)	Speed (rpm)
Escape	Ford	PMSM	70	400max	3000-5000
Prius	Toyota	PMSM	50	500max	1200-1540
Civic	Honda	PMSM	10	144	2500-4000
Insight (CVT)	Honda	PMSM	9.7	144	2000
Getz	Hyundai	PMSM	12	144	6000max
LEV	AXcess (Australia)	SRM	50	250max	6000max
ECOmmodore	Holden (Australia)	SRM	35	250max	6000max

The PMSM is popular for it has high power density, high efficiency and comparatively easier control. However, the magnetic materials used in the PMSM are expensive, and the PMSM produces torque only when it is running at synchronous speed [1]. The SRM is a promising candidate for its simple construction, fault tolerant operation, low cost, and capability of operating over a wide speed range at constant power [1, 12]. However, the disadvantages of a SRM are its high audible noise, high torque ripple and low motor efficiency. Thanks to the advances in power electronic devices and the advent of Digital Signal Processing (DSP) technology. The fast, reliable and cost-effective control of induction motors is being developed now. Over the past five years, the area of induction motor control has continued to expand because of the following advantages of induction motors:

- Simple structure
- Rigidness
- Maintenance free operation
- Relatively low cost
- High transient torque capacity

Many researches [8-12] have proved the induction motor is one of the right electric motor candidates for the most future HEVs.

1.3 The challenges of induction motor control

Despite their benefits, induction motors have one major drawback, which is that their speed is determined by the frequency of the power supply. The reason for this can be

better understood when the operating principle of the motor is studied. Unlike DC motors, the dynamics of an induction motor is nonlinear and of high order. It is difficult to obtain decoupled control of the torque and flux producing components of the stator current. The issue is further complicated because there is no direct access to rotor quantities such as rotor flux and currents, the electric rotor variables are not measurable, and the physical parameters are most often imprecisely known. Therefore, the control of induction motors represents a theoretical and technical challenge problem.

1.4 The speed-sensorless induction motor control approaches

1.4.1 The conventional control methods

The control of the induction motor has attracted much attention in the past few decades; especially the speed-sensorless control of induction motors has been a popular area due to the low system cost and the strong robustness. The V/Hz control for induction motors is the simplest control method, and it is still widely used in industrial applications. However, the V/Hz control is normally used in the applications that don't require precise speed control, and it does not offer torque control or high torque values at low speed. The Field Oriented Control (FOC) is a simple method used in control of induction motor drives because of its intrinsic PI controllers. The classical FOC has simple structure of controller. It is constructed by four PI regulators [25], two of which are used for current signals regulation while another two of which are used for voltage signals regulation. The Nonlinear State Feedback Control (NSFC) system is introduced by A. Benchaib *et al.* [26]. The FOC is reinterpreted as a state feedback transformation into a control system of simpler structure, in which flux amplitude dynamics and torque dynamics are both linear.

Therefore, the input-output decoupling controls for induction motor can be obtained by using multiple PI controllers. The main drawbacks of FOC are the sensitivity of the performance to the system parameters variations and inadequate rejection of external disturbances and load changes [27, 28]. The Direct Torque Control (DTC) was proposed by M. Depenbrock [29] and I. Takahashi [30] in 1985. The DTC is an entirely different approach to induction motor torque control that was developed to overcome FOC's relatively poor transient response and reliance on induction motor parameters. Classical DTC is a popular torque control method for induction motors; therefore it is widely used in the area of the EV's motor control. Unfortunately the classical DTC algorithm has some significant limitations. It is difficult to distinguish between small and large variations in reference values. Also the variation of flux and torque over one sector is considerable. Another problem is that adapting classical DTC to the confines of a DSP's sampling period can significantly deteriorate its performance. Conventional Sliding-Mode Control (SMC) is a robust control because the high gain feedback control input suppresses the influence of the disturbances and uncertainties [31]. Due to SMC technique's strong robustness, and simple hardware/software implementation by means of power inverter, it has attracted much people's attention in electric drive systems, and is one of prospective control methodologies for induction motor drives [32].

Various SMC techniques for induction motors have been proposed in many literatures. The linearization method used in SMC techniques was suggested in References [26, 27, 33]. Linear reference models or input-output linearization techniques were used to control the dynamics of the nonlinear system. A fuzzy technique combining the SMC method was developed in References [28, 34]. The SMC acts in a transient state to enhance the

stability, while fuzzy techniques are used in the steady state to reduce chattering. In References [35 - 37], the Lyapunov direct method is used to ensure the reaching and sustaining of the sliding mode. These SMC methods result in a good transient performance, sound disturbance rejection, and strong robustness in control system. However, the chattering is a problem in SMC and causes the torque, flux, and current ripple in the systems. In Reference [36], sliding-mode concepts were used to implement Pulse Width Modulation (PWM). This implementation method is simple and efficient by mean of power inverter since both implementation of SMC and PWM imply high-frequency switching. However, this method causes severe ripple in the torque signal due to the irregular logic control signals for inverter. To overcome this problem, an rms torque-ripple equation was developed in Reference [38] to minimize torque ripple. In Reference [39], a DTC is combined with Space Vector Modulation (SVM) techniques to improve the torque, flux, and current steady-state waveforms through ripple reduction. Although the torque ripple can be reduced by using these methods, the robustness of control systems is hard to be ensured. Thus, a new control method combining SMC with SVM techniques proposed in this thesis is the potential candidate for ensuring the robustness of control systems and meanwhile reducing the torque ripple.

1.4.2 Observer design methods

In the past, several observer design methods for speed-sensorless control of induction motors have been proposed [40, 41]. Magnetic-Salience-Based methods [42, 43] are very promising for standstill and low-speed operation. Their main disadvantage is the need for high precision voltage and current measurements. Also, these methods require a proper

motor design. Model-Reference Adaptive Systems (MRASs) [44-47] are methods that have a good performance over a large speed range. Their disadvantage is the large influence of parameter deviation at low speed and standstill operation. Also, the use of PI controllers with complicated gains creates difficulties in their implementation using a DSP or microcontrollers. The extended Kalman filter [48-50] has been used as the most appropriate solution for speed-sensorless drives for several years. Unfortunately, this stochastic observer has some inherent disadvantages, such as the influence of the noise characteristic, the absence of design and tuning criteria. The current harmonic spectral estimation method [51] estimates the rotor speed from current harmonics. Since the current harmonics arise from rotor mechanical and magnetic saliencies, they are independent of motor parameters, and their magnitudes are also independent of the source frequency. This method seems to have a very good performance at low speed, even at 1Hz, but it needs a complicated hardware/software setup for measuring and filtering the currents. Artificial intelligence methods [52] that use artificial intelligence techniques such as fuzzy logic and neural networks are very promising candidates to be robust to parameter deviation and measurement noise. However, they need long development period and the expertise in several artificial intelligence procedures. Sliding-mode control theory, due to its order reduction, disturbance rejection, and strong robustness, is one of the prospective control methodologies for electrical machines. The sliding-mode observer for speed-sensorless control proposed in References [25, 36, 53] has been proved being strong robust and accurate torque tracking, and having a very good transient performance over the full speed range. Thus it is one of prospective observers for induction motor drives.

1.4.3 PWM techniques

PWM has been studied extensively during the past decades. For a long period, carrier-based PWM methods were widely used in most applications. The earliest modulation signals for carrier-based PWM are sinusoid wave signals. The use of an injected zero-sequence signal for a three-phase inverter [54] initiated the research on nonsinusoidal carrier-based PWM [55-58]. Different zero-sequence signals lead to different non-sinusoidal PWM modulators. Compared with sinusoidal three-phase PWM, nonsinusoidal three-phase PWM can extend the linear modulation range for line-to-line voltages. With the development of microprocessors and DSP techniques, the SVM technique has become one of the most important PWM methods for the Voltage Source Inverter (VSI). It uses the space vector concept to compute the duty cycle of the switches. It simplifies the digital implementation of PWM modulations. An aptitude for easy digital implementation and wide linear modulation range for output line-to-line voltages are the notable features of SVM [55, 59]. Thus, the SVM becomes a potential technique for the VSI.

1.5 Research objectives

The objectives of this research work are defined as:

1) Develop a robust and accurate flux/speed observer.

Speed sensor decreases the reliability of a drive system and increases its price; furthermore, it is not desirable for an electric motor drive after a speed sensor failure. A common trend in motor control is to eliminate them and use a rotor speed observer to calculate the speed. It is known that the rotor flux is needed for the implementation of

torque or speed control. Unfortunately, the rotor flux cannot be measured directly. If the angle speed is available, the flux can be estimated with a second-order observer and its convergence is guaranteed for any speed. However, if no information about the mechanical variables is acquired, the design of the observer is no longer a trivial problem. In order to achieve the objective of sensorless control of induction motors, it is necessary to design a flux/speed observer to estimate the flux and speed simultaneously based on the measurement of the stator currents and voltages, and then design a corresponding controller to guarantee that the real torque or speed tracks the desired torque or speed.

2) Develop an efficient PWM method for an inverter.

The PWM technique is used to generate the required voltage or current to feed the motor. This method is increasingly used for AC drives with the condition that the harmonic current is as small as possible and the maximum output voltage is as large as possible. An efficient PWM method should achieve the following aims: wide linear modulation range; less switching loss; less Total Harmonic Distortion (THD) in the spectrum of switching waveform; and easy implementation with less computation time.

3) Find reliable control solutions for induction motor to meet HEV system requirements.

Important characteristics of a HEV motor include good drive control and fault tolerance, as well as low noise with high efficiency, flexibility in relation to voltage fluctuation and acceptable mass production costs. The induction motor is one of the right electric motor candidates for the most HEVs because of its low cost, robustness and low maintenance. However, unlike the traditional industrial setting, in which the induction

motor operates mostly at steady state, the HEV applications require high performance control to obtain fast transient responses and energy efficiency. A good induction motor control system for the HEV application should result in a fast transient performance, disturbance rejection, small torque ripple and strong robustness.

1.6 Overview of the thesis

The thesis is organized as follows. The dynamic model of induction motors is given in Chapter 2, and the sliding-mode observer is analyzed and developed in Chapter 3. SVM techniques in induction motor drives are discussed in Chapter 4. Details of control system design are described in Chapter 5, while the simulation results are presented in Chapter 6. Finally, conclusions and recommendations for future work are given in Chapter 7.

Chapter 2
Induction Motor Modeling

2.1 Introduction to induction motors

Three-phase induction motors are rugged, cheap to produce and easy to maintain. They can run at a nearly constant speed from zero to full load. Their design is relatively simple and consists of two main parts, a stationary stator and a rotating rotor. There are two main classes of the induction motor differing in the way how their rotors are wound. The rotor windings in a conventional wound rotor are similar to the stator windings and are usually connected in a uniformly distributed Wye (also known as Star) [60]. The squirrel cage motor has a very different arrangement from this. A cage rotor consists of bare aluminum bars that are short circuited together by being welded to two aluminum end rings. No current supply is needed from outside the rotor to create a magnetic field in the rotor. This is the reason why this motor is so robust and inexpensive. The motor used in this thesis is a three-phase squirrel cage induction motor.

The structure of a squirrel cage induction motor is shown in Figure 2.1. In an induction motor, the alternating currents from the three-phase source flow through the stator windings producing a rotating stator flux. The speed of rotation of this field is determined by the number of poles in the motor and the frequency of power supply. The field induces a voltage in the rotor bars, which leads to a large circulating current. Because the induced rotor current is in the presence of the rotating magnetic field, it is subject to Lorentz's

force. The sum of the Lorentz forces on the rotor bars produces a torque that drives the rotor in the direction of the rotating field.

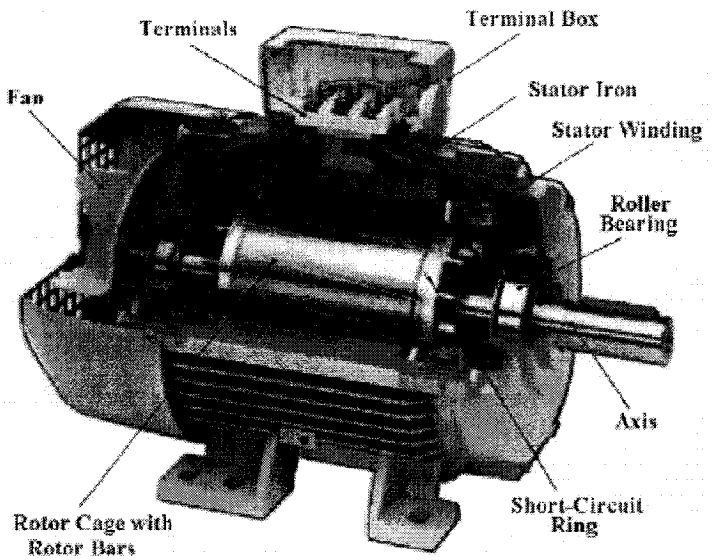

Figure 2.1: Squirrel cage induction motor cross section

When the field is first generated, the rotor is at rest. It rapidly accelerates to keep up with the rotating flux. As the rotor speed increases, the rotor bars are not cut as much by the rotating field, so the voltage in the rotor bars decreases. If the rotor speed equals to the flux speed, the rotor bars will no longer be cut by the field and the rotor will start to slow down. This is why induction motors are referred to as being asynchronous motor because the rotor speed never equals the synchronous speed [60]. The difference between the stator and rotor speed is called slip speed.

2.2 Definitions of space vectors

The usage of space vectors as complex state variables is an efficient method for induction motor modeling. The three-phase voltages, currents and fluxes of induction

motors can be analyzed in terms of complex space vectors [61]. Consider a symmetrical three-phase winding of an induction motor reduced to a two-pole arrangement for simplicity. The three-phase axes are defined by the unity vectors $\boldsymbol{1}$, $\boldsymbol{a}$, and $\boldsymbol{a}^2$, where $\boldsymbol{a} = e^{j(2\pi/3)}$ and $\boldsymbol{a}^2 = e^{j(4\pi/3)}$. The stator windings and stator current space vector in the complex plane is shown in Figure 2.2.

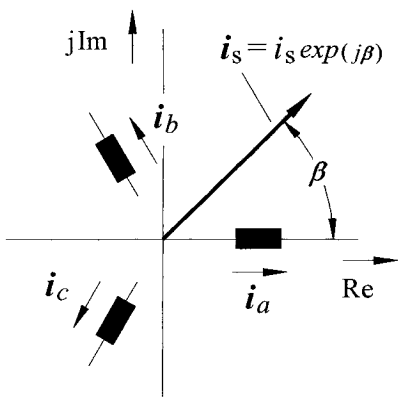

Figure 2.2: Stator windings and stator current space vector

The space vector of the stator current $\boldsymbol{i}_s$ can be described by

$$\boldsymbol{i}_s = \frac{2}{3}(\boldsymbol{i}_a + \boldsymbol{a}\boldsymbol{i}_b + \boldsymbol{a}^2\boldsymbol{i}_c), \tag{2.1}$$

where subscript s refers to the stator of the induction motor; a, b and c are the three-phase system axes.

The flux space vector of the stator winding can be written as

$$\boldsymbol{\psi}_s = L_s\, \boldsymbol{i}_s . \tag{2.2}$$

In the general case, when the induction motor develops nonzero torque, both space vectors $\boldsymbol{i}_s$ of the stator current, and $\boldsymbol{i}_r$ of the rotor current are nonzero, yielding the stator flux and the rotor flux vectors as

$$\boldsymbol{\psi}_s = L_s\, \boldsymbol{i}_s + L_m\, \boldsymbol{i}_r, \tag{2.3}$$

$$\boldsymbol{\psi}_r = L_m\, \boldsymbol{i}_s + L_r\, \boldsymbol{i}_r, \tag{2.4}$$

where L_s, L_r are the stator inductance and the rotor inductance, respectively; L_m is the mutual inductance between the stator and rotor windings. Furthermore,

$$\boldsymbol{i}_r = \frac{2}{3}(\boldsymbol{i}_{ra} + \boldsymbol{a}\boldsymbol{i}_{rb} + \boldsymbol{a}^2\boldsymbol{i}_{rc}) \tag{2.5}$$

is the rotor current space vector, $\boldsymbol{i}_{ra}$, $\boldsymbol{i}_{rb}$, and $\boldsymbol{i}_{rc}$ are the three-phase rotor currents.

The rotating stator flux wave $\boldsymbol{\psi}_s$ generates induced voltages in the stator windings which are described by

$$\boldsymbol{u}_s = \frac{d\boldsymbol{\psi}_s}{dt}, \tag{2.6}$$

where

$$\boldsymbol{u}_s = \frac{2}{3}(\boldsymbol{u}_a + \boldsymbol{a}\boldsymbol{u}_b + \boldsymbol{a}^2\boldsymbol{u}_c) \tag{2.7}$$

is the space vector of the stator voltages, and $\boldsymbol{u}_a$, $\boldsymbol{u}_b$, and $\boldsymbol{u}_c$ are the three-phase voltages at the stator winding terminals.

The individual phase quantities associated with any space vector are obtained as the projections of the space vector on the respective phase axis. Given the space vector $\boldsymbol{u}_s$, for example, the phase voltages are obtained as

$$\begin{aligned} u_a &= Re\ \{\boldsymbol{u}_s\}, \\ u_b &= Re\ \{\boldsymbol{a}^2 \cdot \boldsymbol{u}_s\}, \\ u_c &= Re\ \{\boldsymbol{a} \cdot \boldsymbol{u}_s\}. \end{aligned} \tag{2.8}$$

2.3 The transformation of space vectors

The transformation of space vectors is important for various induction motor controls since it can simplify the control design by transferring a complex three-coordinate system to a two-coordinate system or transferring a time variant system to an invariant system [62]. This transformation mainly includes following two steps:

1). Clarke transformation: $(a, b, c) \Rightarrow (\alpha, \beta)$

It outputs a two-coordinate time variant system.

2). Park transformation: $(\alpha, \beta) \Rightarrow (d, q)$

It outputs a two-coordinate time invariant system.

A diagram of stator current and rotor flux space vectors in three systems is shown in Figure 2.3. $\boldsymbol{\psi}_r = [\boldsymbol{\psi}_\alpha \ \boldsymbol{\psi}_\beta]^T$ and $\boldsymbol{i}_s = [\boldsymbol{i}_\alpha \ \boldsymbol{i}_\beta]^T$ are rotor flux vector and stator current vector in the (α, β) coordinate, respectively; $\boldsymbol{i}_s = [\boldsymbol{i}_d \ \boldsymbol{i}_q]^T$ is stator current vector in the (d, q) coordinate.

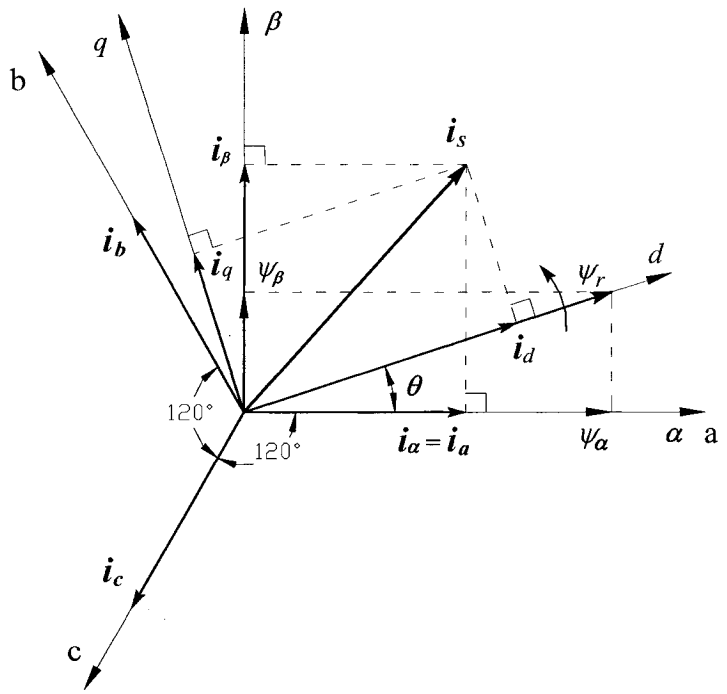

Figure 2.3: Stator current and rotor flux space vectors in three systems

The Clarke transformation for current vectors can be written as

$$\begin{bmatrix} i_\alpha \\ i_\beta \end{bmatrix} = \begin{bmatrix} \frac{2}{3} & -\frac{1}{3} & -\frac{1}{3} \\ 0 & \frac{\sqrt{3}}{3} & -\frac{\sqrt{3}}{3} \end{bmatrix} \cdot \begin{bmatrix} i_a \\ i_b \\ i_c \end{bmatrix}. \tag{2.9}$$

The Park transformation for current vectors can be written as

$$\begin{bmatrix} i_d \\ i_q \end{bmatrix} = \begin{bmatrix} \cos\theta & \sin\theta \\ -\sin\theta & \cos\theta \end{bmatrix} \cdot \begin{bmatrix} i_\alpha \\ i_\beta \end{bmatrix}. \tag{2.10}$$

2.4 Dynamic model of induction motors

2.4.1 Dynamic model of induction motors in the (α,β) system

Assume that three-phase inputs' AC voltages are balanced, and stator windings are uniformly distributed and based on the well-known two-phase equivalent motor representation. The non-saturated symmetrical induction motor can be described in the stationary coordinate system (α,β) by a set of fifth-order non-linear differential equations with respect to rotor velocity ω, the components of rotor magnetic flux ψ_α, ψ_β and of stator current i_α, i_β [31]:

$$
\begin{aligned}
\frac{d\psi_\alpha}{dt} &= -\frac{1}{\tau}\psi_\alpha - \omega\psi_\beta + \frac{L_m}{\tau} i_\alpha, \\
\frac{d\psi_\beta}{dt} &= -\frac{1}{\tau}\psi_\beta + \omega\psi_\alpha + \frac{L_m}{\tau} i_\beta, \\
\frac{di_\alpha}{dt} &= \frac{1}{\sigma L_s}\left(-\frac{L_m}{L_r}\frac{d\psi_\alpha}{dt} - R_s i_\alpha + u_\alpha\right), \\
\frac{di_\beta}{dt} &= \frac{1}{\sigma L_s}\left(-\frac{L_m}{L_r}\frac{d\psi_\beta}{dt} - R_s i_\beta + u_\beta\right), \\
\frac{d\omega}{dt} &= \frac{P}{J}(T - T_L), \\
T &= \frac{3P}{2}\frac{L_m}{L_r}(i_\beta\psi_\alpha - i_\alpha\psi_\beta),
\end{aligned}
\tag{2.11}
$$

where ω is the electrical rotor angle velocity; u_α, u_β are stator voltages in the (α,β) coordinate; T and T_L are the torque of motor and load torque; J is the inertia of the rotor; P is the number of pole pairs. R_r and R_s are rotor and stator resistances; L_r and L_s are rotor and stator inductances; L_m is the mutual inductance; $\tau = L_r / R_r$ is rotor time constant, and $\sigma = 1 - L_m^2/(L_s L_r)$ is total leakage coefficient.

2.4.2 Dynamic model of induction motors in the (*d, q*) system

Some control strategies involve the transformations of the vectors (i_α, i_β) and $(\psi_\alpha, \psi_\beta)$ in the fixed stator coordinates (α, β) into vectors in the coordinates (*d, q*), which rotate along with the rotor flux vector ψ_r. The dynamic model of induction motor in the rotating coordinates (*d, q*) system can be obtained by the following transformations.

From Figure 2.3, the rotor flux position angle θ and the rotor flux amplitude ψ_r can be calculated as

$$\begin{aligned} \sin\theta &= \frac{\psi_\beta}{\psi_r}, \\ \cos\theta &= \frac{\psi_\alpha}{\psi_r}, \\ \psi_r &= \sqrt{\psi_\alpha^2 + \psi_\beta^2}. \end{aligned} \tag{2.12}$$

From Figure 2.3, rotor flux components in the (*d, q*) coordinate ψ_d, ψ_q can be obtained as

$$\begin{aligned} \psi_d &= \psi_r, \\ \psi_q &= 0. \end{aligned} \tag{2.13}$$

From Equations (2.10), (2.12) and (2.13), the following equations can be yielded:

$$\begin{aligned} i_d &= \frac{\psi_\alpha i_\alpha + \psi_\beta i_\beta}{\psi_r}, \\ i_q &= \frac{\psi_\alpha i_\beta - \psi_\beta i_\alpha}{\psi_r}, \\ \psi_d &= \sqrt{\psi_\alpha^2 + \psi_\beta^2} = \psi_r, \\ \psi_q &= 0. \end{aligned} \tag{2.14}$$

From Figure 2.3, the inverse Park transformation of voltage vectors is derived as

$$\begin{bmatrix} u_\alpha \\ u_\beta \end{bmatrix} = \frac{1}{\psi_r} \cdot \begin{bmatrix} \psi_\alpha & -\psi_\beta \\ \psi_\beta & \psi_\alpha \end{bmatrix} \cdot \begin{bmatrix} u_d \\ u_q \end{bmatrix}. \tag{2.15}$$

Considering Equations (2.14), (2.15), and the induction motor dynamic model (2.11), one can obtain the following equations:

$$\begin{aligned} \frac{d\psi_d}{dt} &= \frac{1}{2}(\psi_\alpha^2 + \psi_\beta^2)^{-\frac{1}{2}} \cdot (2\psi_\alpha \cdot \frac{d\psi_\alpha}{dt} + 2\psi_\beta \cdot \frac{d\psi_\beta}{dt}) \\ &= -\frac{1}{\tau}\psi_d + \frac{L_m}{\tau} \cdot \frac{(\psi_\alpha i_\alpha + \psi_\beta i_\beta)}{\psi_d} \\ &= -\frac{1}{\tau}\psi_d + \frac{1}{\tau} L_m i_d, \end{aligned} \tag{2.16}$$

$$\begin{aligned} \frac{di_d}{dt} &= \frac{1}{\psi_d}(\frac{d\psi_\alpha}{dt} \cdot i_\alpha + \frac{di_\alpha}{dt} \cdot \psi_\alpha + \frac{d\psi_\beta}{dt} \cdot i_\beta + \frac{di_\beta}{dt} \cdot \psi_\beta) \\ &= \frac{1}{\psi_d}\Bigg[-\frac{1}{\tau}(\psi_\alpha i_\alpha + \psi_\beta i_\beta) + \frac{1}{\tau} L_m (i_d^2 + i_q^2) + \frac{1}{\sigma\tau} \cdot \frac{L_m}{L_r L_s} \psi_d^2 + \omega(\psi_\alpha i_\beta - \psi_\beta i_\alpha) \\ &\quad -\frac{1}{\sigma}(\frac{R_s}{L_s} + \frac{L_m^2}{\tau L_s L_r})(\psi_\alpha i_\alpha + \psi_\beta i_\beta) + \frac{1}{\sigma L_s}(\psi_\alpha u_\alpha + \psi_\beta u_\beta) \Bigg] \\ &= -\frac{1}{\sigma}(\frac{1}{\tau} + \frac{R_s}{L_s}) i_d + \frac{1}{\sigma\tau L_m}\psi_d + \omega i_q + \frac{L_m i_q^2}{\tau \psi_d} + \frac{1}{\sigma L_s} u_d, \end{aligned} \tag{2.17}$$

$$\begin{aligned} \frac{di_q}{dt} &= \frac{1}{\psi_d}(\frac{d\psi_\alpha}{dt} \cdot i_\beta + \frac{di_\beta}{dt} \cdot \psi_\alpha - \frac{d\psi_\beta}{dt} \cdot i_\alpha - \frac{di_\alpha}{dt} \cdot \psi_\beta) \\ &= \frac{1}{\psi_d}\Bigg[-\frac{1}{\tau}(\psi_\alpha i_\beta - \psi_\beta i_\alpha) - \omega \cdot (\psi_\alpha i_\alpha + \psi_\beta i_\beta) - \frac{1}{\sigma\tau} \cdot \frac{L_m}{L_r L_s} \psi_d^2 \\ &\quad -\frac{1}{\sigma}(\frac{R_s}{L_s} + \frac{L_m^2}{\tau L_s L_r})(\psi_\alpha i_\beta - \psi_\beta i_\alpha) + \frac{1}{\sigma L_s}(\psi_\alpha u_\beta - \psi_\beta u_\alpha) \Bigg] \end{aligned}$$

$$= -\frac{1}{\sigma}(\frac{1}{\tau} + \frac{R_s}{L_s})i_q - \frac{L_m}{\sigma L_s L_r}\omega\psi_d - \omega i_d + \frac{1}{\sigma L_s}u_q, \tag{2.18}$$

$$\frac{d\omega}{dt} = \frac{P}{J}(T - T_L) = \frac{3P^2}{2J}\cdot\frac{L_m}{L_r}(\psi_\alpha i_\beta - \psi_\beta i_\alpha) - \frac{P}{J}T_L$$

$$= \frac{3P^2}{2J}\cdot\frac{L_m}{L_r}\psi_d i_q - \frac{P}{J}T_L, \tag{2.19}$$

$$T = \frac{3P}{2}\cdot\frac{L_m}{L_r}(\psi_\alpha i_\beta - \psi_\beta i_\alpha) = \frac{3P}{2}\frac{L_m}{L_r}\psi_d i_q. \tag{2.20}$$

Using Equations (2.16) – (2.20), we obtain the dynamic model of induction motors in the (*d, q*) coordinate:

$$\begin{aligned}
&\frac{d\psi_d}{dt} = -\frac{1}{\tau}\psi_d + \frac{1}{\tau}L_m i_d,\\
&\frac{di_d}{dt} = -\frac{1}{\sigma}(\frac{1}{\tau} + \frac{R_s}{L_s})i_d + \frac{1}{\sigma\tau L_m}\psi_d + \omega i_q + \frac{L_m i_q^2}{\tau\psi_d} + \frac{1}{\sigma L_s}u_d,\\
&\frac{di_q}{dt} = -\frac{1}{\sigma}(\frac{1}{\tau} + \frac{R_s}{L_s})i_q - \frac{L_m}{\sigma L_s L_r}\omega\psi_d - \omega i_d + \frac{1}{\sigma L_s}u_q,\\
&\frac{d\omega}{dt} = \frac{3P^2}{2J}\cdot\frac{L_m}{L_r}\psi_d i_q - \frac{P}{J}T_L,\\
&T = \frac{3P}{2}\frac{L_m}{L_r}\psi_d i_q.
\end{aligned} \tag{2.21}$$

Based on the above induction motor models, we will design the sliding-model observer, the SVM for the motor drive and the sliding-model controller for HEV applications.

Chapter 3
Sliding-Mode Observer Design

It is known that the rotor flux is needed for the implementation of torque or speed control. Unfortunately, the rotor flux cannot be measured directly. If the angle speed is available, the flux can be estimated with a second-order observer and its convergence is guaranteed for any speed [31, 32]. However, if no information about the mechanical variables is acquired, the design of the observer is no more a trivial problem. In order to implement speed-sensorless control of induction motors, it is necessary to design a flux/speed observer to estimate the flux and speed simultaneously based on the measurement of the stator currents and voltages. Afterwards, a corresponding controller is designed to guarantee that the real torque or speed tracks the desired torque or speed.

Sliding-mode control theory, due to its order reduction, disturbance rejection, and strong robustness, is one of the prospective control methodologies for electrical machines. A sliding-mode observer for speed-sensorless control has been proposed in References [32, 36]. This observer has been proved being strong robust and accurate with a fast convergence, and having a very good estimation performance over the full speed range. Therefore, this observer is discussed, developed and implemented in this Chapter.

3.1 Sliding-mode rotor flux, stator current and speed observer

Applying the same structure of the induction motor described in the stationary coordinate system (α,β) (see Equation 2.11), the sliding-mode rotor flux, stator current and speed observer is proposed as

$$\begin{aligned}
\frac{d\hat{\psi}_\alpha}{dt} &= -\frac{1}{\tau}\hat{\psi}_\alpha - \hat{\omega}\hat{\psi}_\beta + \frac{L_m}{\tau} i_\alpha + C\hat{\psi}_\beta \mu, \\
\frac{d\hat{\psi}_\beta}{dt} &= -\frac{1}{\tau}\hat{\psi}_\beta + \hat{\omega}\hat{\psi}_\alpha + \frac{L_m}{\tau} i_\beta - C\hat{\psi}_\alpha \mu, \\
\frac{d\hat{i}_\alpha}{dt} &= \frac{1}{\sigma L_s}\left(-\frac{L_m}{L_r}\frac{d\hat{\psi}_\alpha}{dt} - R_s i_\alpha + u_\alpha + C\frac{L_m}{L_r}\hat{\psi}_\beta \mu - \frac{L_m}{L_r}\hat{\psi}_\alpha \mu\right), \\
\frac{d\hat{i}_\beta}{dt} &= \frac{1}{\sigma L_s}\left(-\frac{L_m}{L_r}\frac{d\hat{\psi}_\beta}{dt} - R_s i_\beta + u_\beta - C\frac{L_m}{L_r}\hat{\psi}_\alpha \mu - \frac{L_m}{L_r}\hat{\psi}_\beta \mu\right).
\end{aligned} \tag{3.1}$$

Substituting Equation (2.11) into Equation (3.1), one can obtain the equations:

$$\begin{aligned}
\frac{d\hat{\psi}_\alpha}{dt} &= -\frac{1}{\tau}\hat{\psi}_\alpha - \hat{\omega}\hat{\psi}_\beta + \frac{L_m}{\tau} i_\alpha + C\hat{\psi}_\beta \mu, \\
\frac{d\hat{\psi}_\beta}{dt} &= -\frac{1}{\tau}\hat{\psi}_\beta + \hat{\omega}\hat{\psi}_\alpha + \frac{L_m}{\tau} i_\beta - C\hat{\psi}_\alpha \mu, \\
\frac{d\hat{i}_\alpha}{dt} &= \frac{1}{\sigma L_s}\left(\frac{L_m}{\tau \cdot L_r}\hat{\psi}_\alpha + \frac{L_m}{L_r}\hat{\omega}\hat{\psi}_\beta - \frac{L_m^2 R_r + L_r^2 R_s}{L_r^2} i_\alpha + u_\alpha - \frac{L_m}{L_r}\hat{\psi}_\alpha \mu\right), \\
\frac{d\hat{i}_\beta}{dt} &= \frac{1}{\sigma L_s}\left(\frac{L_m}{\tau \cdot L_r}\hat{\psi}_\beta - \frac{L_m}{L_r}\hat{\omega}\hat{\psi}_\alpha - \frac{L_m^2 R_r + L_r^2 R_s}{L_r^2} i_\beta + u_\beta - \frac{L_m}{L_r}\hat{\psi}_\beta \mu\right),
\end{aligned} \tag{3.2}$$

where continuous time function $\hat{\psi}_\alpha$ and $\hat{\psi}_\beta$ represent the estimated rotor fluxes , and $\hat{i}_\alpha$ and $\hat{i}_\beta$ represent the estimated stator currents. C is a parameter to be selected. The estimate of the angle speed $\hat{\omega}$ and the auxiliary variable μ are discontinuous parameters given by

$$\hat{\omega} = \omega_0 sign(s_\omega),$$
$$\mu = \mu_0 sign(s_\mu), \tag{3.3}$$

where ω_0 and μ_0 are constants; s_ω and s_μ are nonlinear functions of the stator current errors and the estimated rotor flux, and

$$s_\omega = (\hat{i}_\beta - i_\beta)\bar{\psi}_\alpha - (\hat{i}_\alpha - i_\alpha)\bar{\psi}_\beta,$$
$$s_\mu = (\hat{i}_\alpha - i_\alpha)\bar{\psi}_\alpha + (\hat{i}_\beta - i_\beta)\bar{\psi}_\beta. \tag{3.4}$$

The method of selecting s_ω and s_μ is nothing but the conventional approach to control design based on the equation in the frame rotating with the rotor flux [63]. It enables one to decouple the design problem of making the estimates $\hat{i}_\alpha$ and $\hat{i}_\beta$ track i_α and i_β into two independent ones.

First, it will be shown that there exist constant values ω_0 and μ_0 such that sliding modes occur in the surfaces of $s_? = 0$ and $s_\mu = 0$. And, as a result, the estimation errors

$$\bar{i}_\alpha = \hat{i}_\alpha - i_\alpha,$$
$$\bar{i}_\beta = \hat{i}_\beta - i_\beta \tag{3.5}$$

are equal to zero, and the flux estimation errors

$$\overline{\psi}_\alpha = \bar{\psi}_\alpha - \psi_\alpha,$$
$$\overline{\psi}_\beta = \bar{\psi}_\beta - \psi_\beta \tag{3.6}$$

will approach to zero. Thus, the average value of the discontinuous function $\hat{\omega}$ will converge to the real speed ω.

3.2 Analysis of the current tracking

To analyze convergence of the estimates to the real values for the proposed observer structure, one needs to analyze the stator current tracking property first. Following from the induction motor model (2.11) and Equation (3.2), the sliding-mode observer equations with respect to the errors $\bar{i}_\alpha$, $\bar{i}_\beta$, $\bar{\psi}_\alpha$ and $\bar{\psi}_\beta$ can be written as

$$\begin{aligned}
\frac{d\bar{\psi}_\alpha}{dt} &= -\frac{1}{\tau}\bar{\psi}_\alpha - \omega\bar{\psi}_\beta - \bar{\omega}\hat{\psi}_\beta + C\hat{\psi}_\beta\mu \\
\frac{d\bar{\psi}_\beta}{dt} &= -\frac{1}{\tau}\bar{\psi}_\beta + \omega\bar{\psi}_\alpha + \bar{\omega}\hat{\psi}_\alpha - C\hat{\psi}_\alpha\mu, \\
\frac{d\bar{i}_\alpha}{dt} &= \frac{L_m}{\sigma L_s L_r}\left(\frac{1}{\tau}\bar{\psi}_\alpha + \omega\bar{\psi}_\beta + \bar{\omega}\hat{\psi}_\beta - \hat{\psi}_\alpha\mu\right), \\
\frac{d\bar{i}_\beta}{dt} &= \frac{L_m}{\sigma L_s L_r}\left(\frac{1}{\tau}\bar{\psi}_\beta - \omega\bar{\psi}_\alpha - \bar{\omega}\hat{\psi}_\alpha - \hat{\psi}_\beta\mu\right).
\end{aligned} \tag{3.7}$$

The combination of Equations (3.2) and (3.7) yields the following equations:

$$\dot{s}_\omega = \dot{\bar{i}}_\beta\hat{\psi}_\alpha - \dot{\bar{i}}_\alpha\hat{\psi}_\beta + \dot{\bar{i}}_\beta\dot{\hat{\psi}}_\alpha - \bar{i}_\alpha\dot{\hat{\psi}}_\beta, \tag{3.8}$$

$$\dot{\bar{i}}_\beta\hat{\psi}_\alpha - \dot{\bar{i}}_\alpha\hat{\psi}_\beta = \frac{L_m}{\sigma L_s L_r}\left[(\omega - \hat{\omega})\hat{\psi}_r^2 + \frac{1}{\tau}e_2 - \omega e_1\right], \tag{3.9}$$

$$\bar{i}_\beta\dot{\hat{\psi}}_\alpha - \bar{i}_\alpha\dot{\hat{\psi}}_\beta = -\hat{\omega}s_\mu + \frac{L_m}{\tau}(\bar{i}_\beta i_\alpha - \bar{i}_\alpha i_\beta) + Cs_\mu\mu. \tag{3.10}$$

Then,

$$\dot{s}_\omega = -\left(\frac{L_m}{\sigma L_s L_r}\hat{\psi}_r^2 + s_\mu\right)\cdot\omega_0 sign\, s_\omega + f(\omega, \bar{i}_\alpha, \bar{i}_\beta, e_1, e_2), \tag{3.11}$$

where $\hat{\psi}_r = \sqrt{\hat{\psi}_\alpha^2 + \hat{\psi}_\beta^2}$,

$$f(\omega, \bar{i}_\alpha, \bar{i}_\beta, e_1, e_2) = \frac{L_m}{\sigma L_s L_r}\omega\hat{\psi}_r^2 + \frac{L_m}{\tau}(\bar{i}_\beta i_\alpha - \bar{i}_\alpha i_\beta) + \frac{L_m}{\sigma L_s L_r}\left(\frac{1}{\tau}e_2 - \omega e_1\right) + Cs_\mu\mu,$$

and

$$e_1 = \overline{\psi}_\alpha \hat{\psi}_\alpha + \overline{\psi}_\beta \hat{\psi}_\beta ,$$
$$e_2 = \overline{\psi}_\beta \hat{\psi}_\alpha - \overline{\psi}_\alpha \hat{\psi}_\beta . \tag{3.12}$$

It follows from Equation (3.11) that, if the condition

$$\frac{L_m}{\sigma L_s L_r} \hat{\psi}_r^2 + s_\mu > 0 \tag{3.13}$$

holds, then for high enough ω_0, $s_\omega \dot{s}_\omega < 0$, i.e., sliding mode will occur on surface $s_\omega = 0$.

Similarly, the derivative of s_μ can be derived

$$\dot{s}_\mu = \dot{\bar{i}}_\alpha \hat{\psi}_\alpha + \dot{\bar{i}}_\beta \hat{\psi}_\beta + \dot{\bar{i}}_\alpha \dot{\hat{\psi}}_\alpha + \bar{i}_\beta \dot{\hat{\psi}}_\beta$$

$$= \frac{L_m}{\sigma L_s L_r}\left(\frac{1}{\tau} e_1 + \omega e_2\right) + \frac{L_m}{\tau}\left(i_\alpha \bar{i}_\alpha + i_\beta \bar{i}_\beta\right) - \frac{L_m}{\sigma L_s L_r} \mu_0 \hat{\psi}_r^2 sign\, s_\mu . \tag{3.14}$$

From Equation (3.14), it is noted if μ_0 is high enough, $s_\mu \dot{s}_\mu < 0$, and sliding mode will occur on the surface $s_\mu = 0$.

After sliding mode arises on the intersection of both surfaces $s_\omega = \bar{i}_\beta \hat{\psi}_\alpha - \bar{i}_\alpha \hat{\psi}_\beta = 0$ and $s_\mu = \bar{i}_\alpha \hat{\psi}_\alpha + \bar{i}_\beta \hat{\psi}_\beta = 0$, the current errors will approach to zero, i.e., $\bar{i}_\alpha = 0$ and $\bar{i}_\beta = 0$ under the assumption $\hat{\psi}_r^2 \neq 0$, which means that the estimated currents $\hat{i}_\alpha$ and $\hat{i}_\beta$ converge to the real currents i_α and i_β.

The sliding-mode equations on s_ω =0 and s_μ =0 can be derived by replacing the discontinuous functions $\omega_0 sign(s_\omega)$ and $\mu_0 sign(s_\mu)$ by the equivalent values ω_{eq} and μ_{eq}, which are the solutions of the algebraic equations $\dot{s}_\omega$ =0 and $\dot{s}_\mu$ =0 [32]. For this case,

$$\omega_{eq} = \omega - \frac{\omega}{\hat{\psi}_r^2} e_1 + \frac{1}{\tau \hat{\psi}_r^2} e_2 . \tag{3.15}$$

From Equation (3.15), if the estimated rotor flux converges to the real flux, also the equivalent rotor speed will converge to the real speed. However, ω_{eq} cannot be evaluated by Equation (3.15), since it contains unknown real rotor flux in the errors e_1 and e_2. Because the estimated rotor angle speed $\hat{\omega}$ has slow and high-frequencies components, of which the slow component is equal to ω_{eq}, ω_{eq} may be obtained through a low-pass filter [31] with discontinuous value $\hat{\omega}$ as the input, that is,

$$\omega_{eq} \approx \frac{\hat{\omega}}{1+\tau_f s}, \tag{3.16}$$

where τ_f is the time constant of the low-pass filter.

Remark: τ_f should be chosen small enough as compared with the slow component of the real control $\hat{\omega}$, but large enough to filter out the high rate component [31] .

3.3 Analysis of the observer design

From the analysis of the current tracking, it is noted that the condition $\frac{L_m}{\sigma L_s L_r} \hat{\psi}_r^2 + s_\mu > 0$ for the sliding mode to occur on the surface s_ω =0 is not very

restrictive. The reasons are that the stator currents i_α and i_β are measurable. The initial conditions $\hat{i}_\alpha(0)$ and $\hat{i}_\beta(0)$ can always be chosen close enough to the true stator currents $i_\alpha(0)$ and $i_\beta(0)$ such that the initial errors $\bar{i}_\alpha(0)$ and $\bar{i}_\beta(0)$ or s_μ are small enough to guarantee that the condition (3.13) holds.

Although the flux/speed observer is of the fourth order, the error equations of the sliding-mode observer are actually of the second order after sliding mode arises on the surfaces s_ω =0 and s_μ =0. This order reduction property of the sliding mode is very helpful for the asymptotic stability analysis of the nonlinear time-varying error system.

To facilitate the analysis of the observer tracking error system, the errors e_1 and e_2 are defined in Equation (3.12) as the state variables of the error system. The error dynamic models of rotor flux estimation are obtained by differentiating the transformed flux errors e_1 and e_2:

$$\begin{aligned} \dot{e}_1 &= \dot{\bar{\psi}}_\alpha \hat{\psi}_\alpha + \dot{\bar{\psi}}_\beta \hat{\psi}_\beta + \bar{\psi}_\alpha \dot{\hat{\psi}}_\alpha + \bar{\psi}_\beta \dot{\hat{\psi}}_\beta , \\ \dot{e}_2 &= \dot{\bar{\psi}}_\beta \hat{\psi}_\alpha - \dot{\bar{\psi}}_\alpha \hat{\psi}_\beta + \bar{\psi}_\beta \dot{\hat{\psi}}_\alpha - \bar{\psi}_\alpha \dot{\hat{\psi}}_\beta . \end{aligned} \tag{3.17}$$

$\bar{\psi}_\alpha$ and $\bar{\psi}_\beta$ are found from Equation (3.12),

$$\begin{aligned} \bar{\psi}_\alpha &= \frac{\hat{\psi}_\alpha}{\hat{\psi}_r^2} e_1 - \frac{\hat{\psi}_\beta}{\hat{\psi}_r^2} e_2 , \\ \bar{\psi}_\beta &= \frac{\hat{\psi}_\beta}{\hat{\psi}_r^2} e_1 - \frac{\hat{\psi}_\alpha}{\hat{\psi}_r^2} e_2 . \end{aligned} \tag{3.18}$$

Combining Equations (3.2), (3.7), (3.17) and (3.18), one can obtain the following equations:

$$\dot{e}_1 = \frac{1}{\tau}(-2 + \frac{L_m i_d}{\hat{\psi}_r})e_1 + (\frac{1}{\tau}\frac{L_m i_q}{\hat{\psi}_r} + \overline{\omega})e_2 - C\mu e_2 ,$$
$$\dot{e}_2 = \frac{1}{\tau}(-1 + \frac{L_m i_d}{\hat{\psi}_r})e_2 - (\omega - \overline{\omega} + \frac{1}{\tau}\frac{L_m i_q}{\hat{\psi}_r})e_1 - C\hat{\psi}_r^2\mu + C\mu e_1 , \tag{3.19}$$

where

$$i_d = \frac{\hat{\psi}_\alpha}{\hat{\psi}_r} i_\alpha + \frac{\hat{\psi}_\beta}{\hat{\psi}_r} i_\beta ,$$
$$i_q = \frac{\hat{\psi}_\alpha}{\hat{\psi}_r} i_\beta - \frac{\hat{\psi}_\beta}{\hat{\psi}_r} i_\alpha . \tag{3.20}$$

After sliding mode occurs, $\hat{\omega}$ should be replaced by ω_{eq} in the motion equations. Therefore, the speed deviation $\overline{\omega}$ can be calculated from Equation (3.15)

$$\overline{\omega} = -\frac{\omega}{\hat{\psi}_r^2} e_1 + \frac{R_r}{L_r \hat{\psi}_r^2} e_2 . \tag{3.21}$$

Substitution of Equation (3.21) into Equation (3.19) results in the error dynamics in matrix form:

$$\begin{bmatrix} \dot{e}_1 \\ \dot{e}_2 \end{bmatrix} = \frac{1}{\tau} \cdot \begin{bmatrix} -2 + \frac{L_m i_d}{\hat{\psi}_r} & \frac{L_m i_q}{\hat{\psi}_r} \\ -\tau\omega - \frac{L_m i_q}{\hat{\psi}_r} & -1 + \frac{L_m i_d}{\hat{\psi}_r} \end{bmatrix} \cdot \begin{bmatrix} e_1 \\ e_2 \end{bmatrix}$$
$$+ C\mu \cdot \begin{bmatrix} -e_2 \\ -\hat{\psi}_r{}^2 + e_1 \end{bmatrix} + \frac{1}{\hat{\psi}_r{}^2} \cdot \begin{bmatrix} \omega e_1 e_2 + \frac{1}{\tau} e_2^2 \\ \omega e_1^2 - \frac{1}{\tau} e_1 e_2 \end{bmatrix} . \tag{3.22}$$

Assuming that sliding mode also arises on manifold s_μ=0, one solves the algebraic equation $\dot{s}_\mu$=0 (3.14) with respect to μ ,

$$\mu_{eq} = \frac{1}{\tau \hat{\psi}_r^2} e_1 + \frac{\omega}{\hat{\psi}_r^2} e_2 . \tag{3.23}$$

The discontinuous parameter μ can be eliminated from the error dynamics. Since the estimates $\hat{\psi}_r^2$ and $\hat{T}$ track the reference inputs, we infer:

$$\psi_{ref} = \hat{\psi}_r , \tag{3.24}$$

$$\frac{d\hat{\psi}_r}{dt} = \frac{d\psi_{ref}}{dt} , \tag{3.25}$$

$$T_{ref} = \frac{3P}{2} \frac{L_m}{L_r} (i_\beta \hat{\psi}_\alpha - i_\alpha \hat{\psi}_\beta) . \tag{3.26}$$

To express Equations (3.2), (3.25) and (3.26) in the (d, q) frame, one finds i_α, i_β from Equation (3.20):

$$\begin{aligned} i_\alpha &= \frac{\hat{\psi}_\alpha}{\hat{\psi}_r} i_d - \frac{\hat{\psi}_\beta}{\hat{\psi}_r} i_q , \\ i_\beta &= \frac{\hat{\psi}_\alpha}{\hat{\psi}_r} i_q + \frac{\hat{\psi}_\beta}{\hat{\psi}_r} i_d . \end{aligned} \tag{3.27}$$

For constant ψ_{ref}, after substituting the above two equations and Equations (3.2) and (3.24) into Equations (3.25) and (3.26), one can yield

$$i_q = \frac{2L_r T_{ref}}{3PL_m \psi_{ref}} , \tag{3.28}$$

$$i_d = \frac{\hat{\psi}_r}{L_m} . \tag{3.29}$$

Finally, the error dynamic model can be simplified by substituting Equations (3.23), (3.24), (3.28) and (3.29) into the error dynamic system (3.22), and performing linearization.

$$\begin{bmatrix} \dot{e}_1 \\ \dot{e}_2 \end{bmatrix} = \begin{bmatrix} -\frac{1}{\tau} & \frac{2T_{ref}R_r}{3P\psi_{ref}^2} \\ -\omega_{eq} - \frac{2T_{ref}R_r}{3P\psi_{ref}^2} - \frac{C}{\tau} & -C\omega_{eq} \end{bmatrix} \cdot \begin{bmatrix} e_1 \\ e_2 \end{bmatrix}. \tag{3.30}$$

Note that the linearized error system does not depend on the real speed, real rotor flux and real stator current. It depends only on the reference torque, the magnitude of the reference flux, the equivalent angle speed and the adjustable parameter C. As one follows from Equation (3.30), for large C, the motion of the error dynamic system can be decomposed into the slow and fast motion [64]. The fast component $\frac{1}{\tau}e_1 + \omega_{eq}e_2$ decays rapidly with

$$\lim_{t\to\infty} e_2 = -\frac{1}{\tau\omega_{eq}}e_1. \tag{3.31}$$

The slow motion is governed by

$$\dot{e}_1 = -\frac{1}{\tau}(1 + \frac{2T_{ref}R_r}{3P\psi_{ref}^2\omega_{eq}})e_1. \tag{3.32}$$

One of the sufficient conditions for the asymptotic stability of the slow motion for any time-varying speed is

$$1 + \frac{2T_{ref}R_r}{3P\psi_{ref}^2\omega_{eq}} > 0. \tag{3.33}$$

It is clear that

$$\frac{2T_{ref}R_r}{3P\psi_{ref}^2\omega_{eq}} > 0 \tag{3.34}$$

is a sufficient condition as well. It means that the solution to Equation (3.32) is stable and $\lim_{t\to\infty} e_1 = 0$ if the reference torque and the equivalent speed have the same sign. From Equation (3.31), one may infer $\lim_{t\to\infty} e_2 = 0$.

3.4 Chattering-free sliding-mode observer

The sliding-mode design method for an observer is a robust nonlinear design technique which introduces discontinuities in the observer differential equations. Due to these discontinuities, sliding-mode design method suffers from chattering. The term "chattering" describes the phenomenon of finite-frequency, finite-amplitude oscillations appearing in many sliding-mode implementations. These oscillations are caused by the high frequency switching of sliding-mode components exciting un-modeled dynamics in the closed loop. The un-modeled dynamics are generally significantly faster than the main system dynamics.

There are essentially two ways of producing chattering-free performance in sliding mode. One technique for producing chattering-free sliding mode utilizes higher order sliding modes. In that technique the state equation is differentiated to produce a differential equation which consists of the derivative of the control input. The derivative is utilized as a new control variable. Hence, this new control variable can be discontinuous while producing a continuous control input. The difficulty with this technique is that the derivative of the state variable is not available for measurement, and hence other observers have to be designed to estimate that variable. One simple approach

for chattering reduction involves introducing a boundary layer around the switching surface and using a continuous control within the boundary layer.

The boundary layer solution, proposed by *Slotine* and *Sastry* [65] and *Slotine* [66], seeks to avoid control discontinuities and switching action in the control loop. The concept of a boundary layer around a sliding surface is illustrated in Figure 3.1.

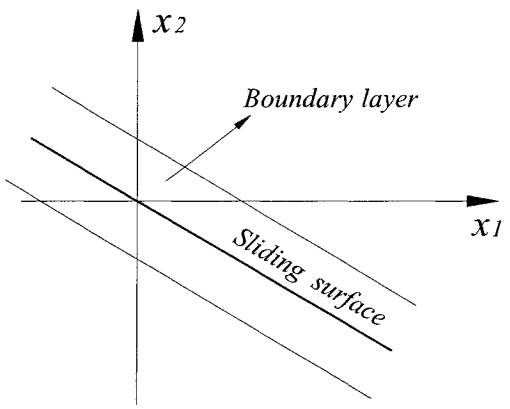

Figure 3.1: A boundary layer around a sliding surface

The discontinuous control law is replaced by a saturation function which approximates the *sign*(*s*) term in a boundary layer of the sliding manifold $s(t)=0$. The saturation function is illustrated in Figure 3.2.

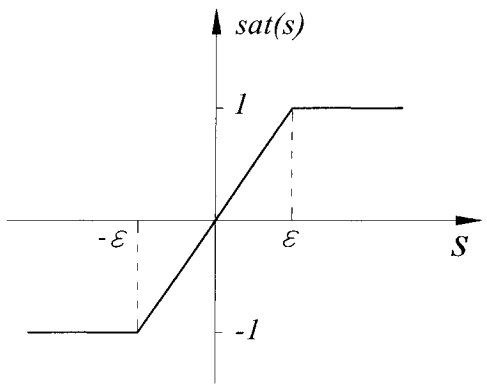

Figure 3.2: Saturation type function

That is, the sign functions in the control are to be replaced by saturation functions where

$$sat(s)=\begin{cases}1, & s/\varepsilon > 1\\ s, & -1 \le s/\varepsilon \le 1.\\ -1, & s/\varepsilon < -1\end{cases} \tag{3.35}$$

"In the large", i.e., for $|s(t)| > \varepsilon$, $sat(s)=sign(s)$. However, in a small ε-vicinity of the origin, the so-called boundary layer, $sat(s) \neq sign(s)$ is continuous. The control signal that results from using the saturation type of function is no different from the switching control whenever the state is outside of the boundary layer. Therefore, one can expect that the system state will be driven to the boundary layer of the sliding surface.

One of the benefits of the boundary layer approach is that sliding-mode design methodologies can be exploited to derive a continuous controller. The invariance property of sliding-mode control is partially preserved in the sense that the system trajectories are confined to ε-vicinity of the sliding manifold $s(t)=0$, instead of exactly to $s(t)=0$ as in the ideal sliding mode. Within the ε-vicinity, however, the system behavior is not determined, i.e., further convergence to zero is not guaranteed. Note that no real sliding mode takes place since the switching action is replaced by a continuous approximation.

3.5 Sliding-mode observer implementation

Based on the model of observer proposed in Section 3.1 and design analysis in Sections 3.2 and 3.3, a simplified block diagram of the observer structure is implemented in Figure 3.3.

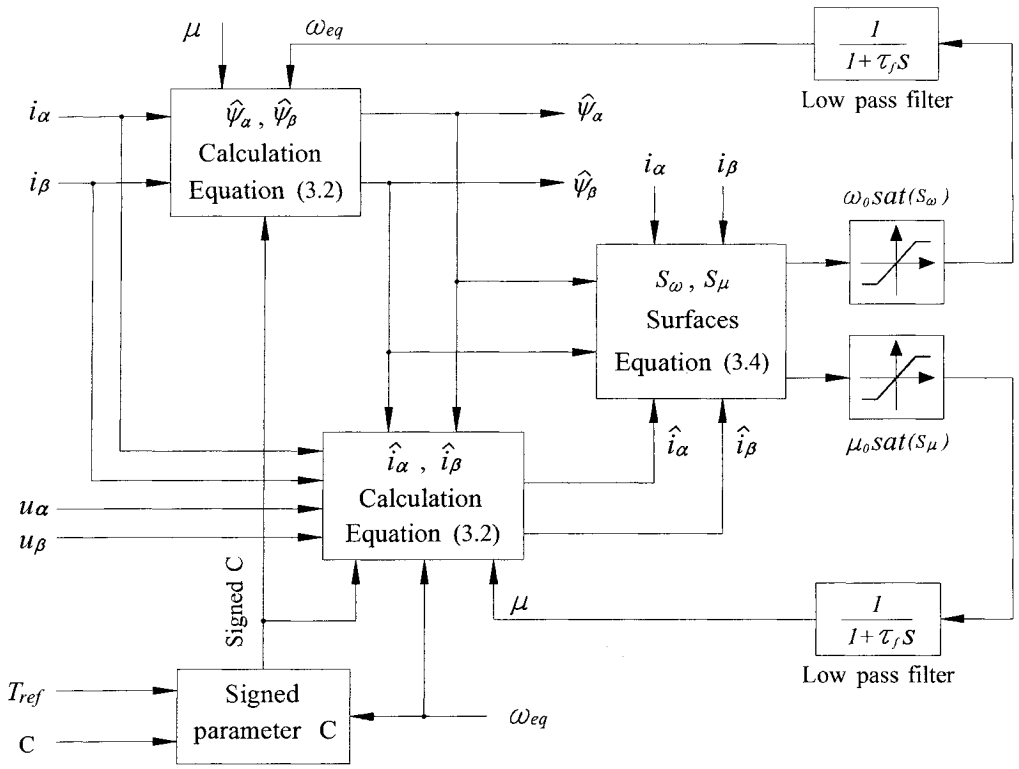

Figure 3.3: Sliding-mode observer structure

3.6 The test of sliding-mode observer

The simplified test block diagram is shown in Figure 3.4.

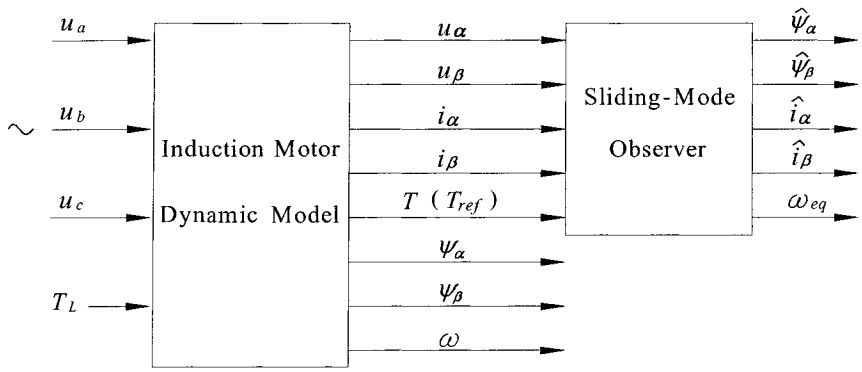

Figure 3.4: Sliding-mode observer test block diagram

u_a, u_b and u_c are three-phase balance sinusoidal signals, and

$$u_a = 10\sin(100\pi t + 4\pi/3),$$

$$u_b = 10\sin(100\pi t + 2\pi/3),$$

$$u_c = 10\sin(100\pi t).$$

T_L is load torque of the induction motor, and T_L=*0.5Nm*. The nominal parameters of the test induction motor are listed in Table 3.1 [36].

Table 3.1: Induction motor nominal parameters

Ls=590 μ H	P=1
Lr=590 μ H	J=4.33e-4N.m.s^2
Lm=555 μ H	B=0.04N.m.s/rad
Rs=0.0106 Ω	Rated voltage=24V
Rr=0.0118 Ω	

Based the analysis in Sections 3.2 and 3.3, the constants ω_0 and μ_0 should be selected high enough so that sliding modes can occur on the surfaces $s_\omega = 0$ and $s_\mu = 0$. The time constant of the low-pass filter τ_f should be chosen small enough as compared with the slow component of the estimated speed, but large enough as compared with high rate component. The parameter C determines the convergent speed of rotor flux. In this test block diagram, constants ω_0 and μ_0 are selected as $\omega_0 = 600$ and $\mu_0 = 800$; the time constant of the low-pass filter is given as $\tau_f = 0.00015$; parameter *C* is chosen as *C=30.*

The test is implemented by using MATLAB/SIMULINK. The test results are shown in Figures 3.5 – 3.7.

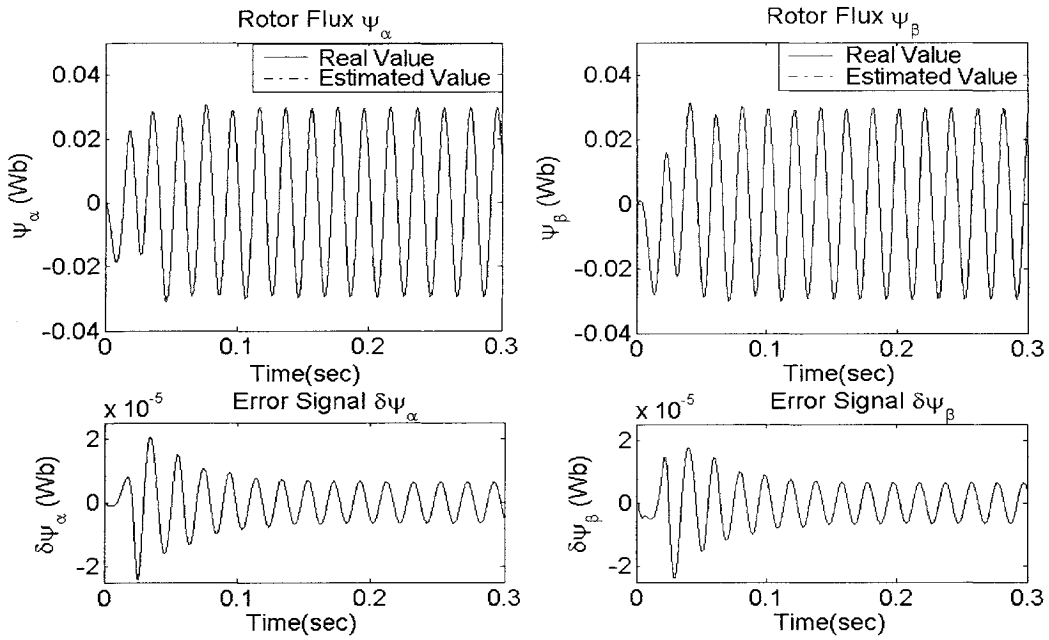

Figure 3.5: Estimated and real rotor flux

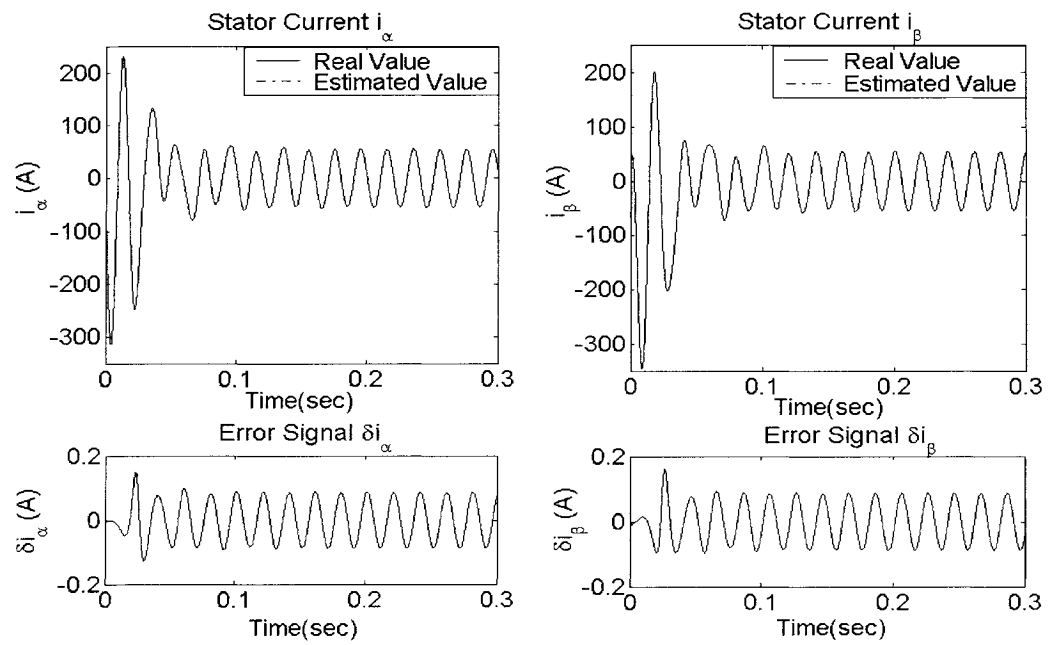

Figure 3.6: Estimated and real stator current

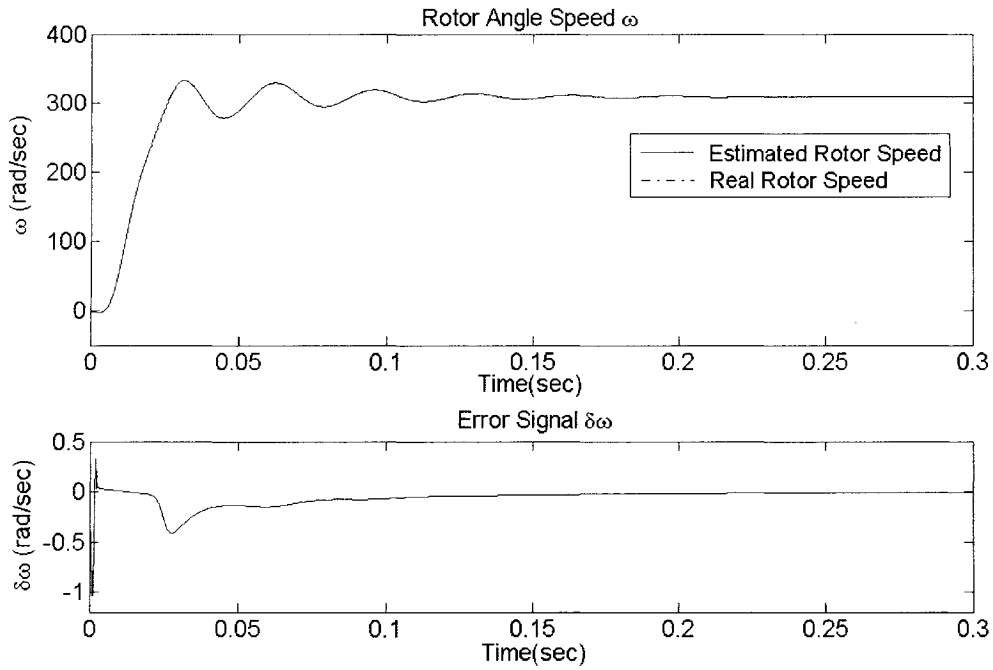

Figure 3.7: Estimated and real rotor angle speed

Figures 3.5–3.7 show that the estimated rotor flux, stator current and rotor angle speed track the real values with small errors. These test results show the proposed sliding-mode observer has good convergence and asymptotic performance.

The tests are performed in an open-loop system. The test purpose is only to show when the parameters are selected properly, the sliding modes can occur, and the estimated rotor flux, stator current and rotor speed can converge to the real values. The simulations in the close-loop system will be performed in Chapter 6.

Chapter 4
SVM Techniques for Induction Motor Drives

4.1 Introduction

Due to the advances in solid state power devices and microprocessors, switching power inverters are widely used in modern motor drives to convert and deliver the required energy to the motor. The energy that a switching power inverter delivers to a motor is controlled by PWM signals applied to the gates of the Insulated Gate Bipolar Transistors (IGBTs). PWM signals are pulse trains with fixed frequency and magnitude and variable pulse width. There is one pulse of fixed magnitude in every PWM period. However, the width of the pulses changes from pulse to pulse according to a modulating signal. When a PWM signal is applied to the gate of an IGBT, it causes the turn-on and turn-off intervals of the IGBT to change from one PWM period to another PWM period according to the same modulating signal. The frequency of a PWM signal must be much higher than that of the energy delivered to the motor and its load depends mostly on the modulating signal. The advantages of PWM based switching power inverter over linear power amplifier are [67]:

- Easy to implement and control.
- No temperature variation-caused and aging-caused drifting or degradation in linearity.
- Compatible with today's digital microprocessors.
- Lower power dissipation.

PWM technique is used to generate the required voltage or current to feed the motor. This method is increasingly used for AC drives with the condition that the harmonic current is as small as possible and the maximum output voltage is as large as possible. PWM has been studied extensively during the past decades. Many different PWM methods have been developed to achieve the following objectives: wide linear modulation range; less switching loss; less THD in the spectrum of switching waveform; and easy implementation and less computation time. For a long period, carrier-based PWM methods were widely used in most applications. The modulation signals of carrier-based PWM include two types: sinusoidal and nonsinusoidal signals. Compared with sinusoidal three-phase PWM, nonsinusoidal three-phase PWM can extend the linear modulation range for line-to-line voltages. With the development of microprocessors and DSP techniques, the SVM technique has become one of the most important PWM methods for VSI. It uses the space vector concept to compute the duty cycle of the switches. It simplifies the digital implementation of PWM modulations. An aptitude for easy digital implementation and wide linear modulation range for output line-to-line voltages are the notable features of SVM. Therefore, SVM is discussed, developed and implemented in this Chapter.

4.2 The structure of PWM drives

PWM drives provide the sinusoidal current output to control frequency and voltage supplied to an induction motor. A basic PWM drive consists of a converter, DC link, control logic, and an inverter. The structure of a typical two-level PWM drive is shown in Figure 4.1.

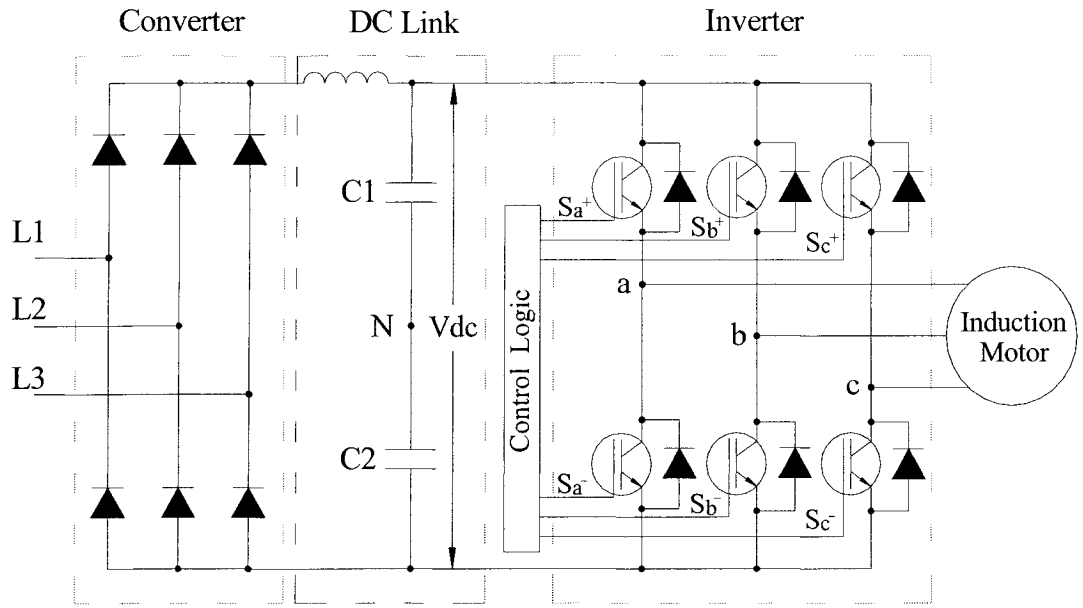

Figure 4.1: Two-level PWM drive

Converter and DC Link

The converter section consists of a fixed diode bridge rectifier which converts the three-phase power supply to a DC voltage. The L choke and C1 and C2 capacitors smooth the converted DC voltage. The rectified DC value is approximately 1.35 times the line-to-line value of the supply voltage.

Control logic and inverter

The output voltage and frequency to the motor are controlled by the control logic and inverter section. The inverter section consists of six switching devices. Various devices can be used such as thyristors, bipolar transistors, and IGBTs. Figure 4.1 shows an inverter that utilizes IGBTs. The control logic uses a microprocessor or a DSP to switch the IGBTs on and off providing a variable voltage and frequency to the motor.

IGBTs

IGBTs provide a high switching speed necessary for PWM inverter operation. IGBTs are capable of switching on and off several thousand times a second. An IGBT can turn on in less than 400 nanoseconds and off in approximately 500 nanoseconds. An IGBT consists of a gate, collector and emitter. When a positive voltage (typically +15VDC) is applied to the gate, the IGBT will turn on. This is similar to closing a switch. Current will flow between the collector and emitter. An IGBT is turned off by removing the positive voltage from the gate. During the off state the IGBT gate voltage is normally held at a small negative voltage (-15VDC) to prevent the device from turning on. The structure of an IGBT is shown in Figure 4.2.

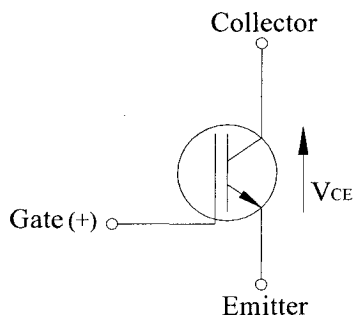

Figure 4.2: IGBT structure

4.3 SVM techniques for the PWM inverter

The SVM technique is more preferable scheme to the PWM voltage source inverter since it gives a large linear control range, less harmonic distortion and fast transient response [55, 59]. A scheme of the three-phase two-level PWM inverter with a star-connection load is shown in Figure 4.3.

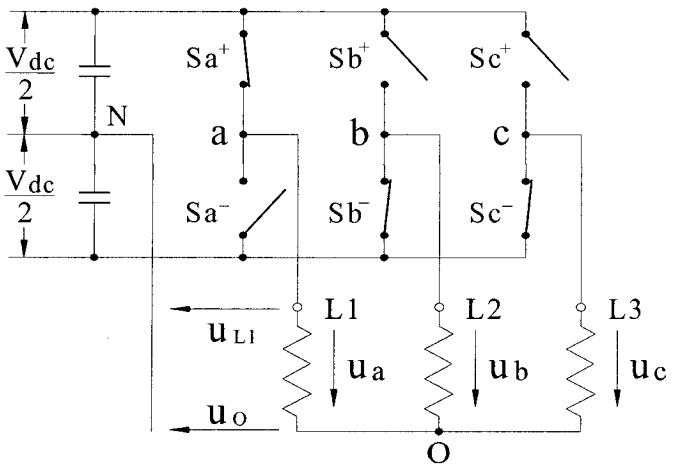

Figure 4.3: Three-phase two-level inverter with a star-connection load

From Figure 4.3, the switched three-phase waveforms for a star-connection three-phase induction motor being fed from a switched power inverter and receiving the symmetrical rectangular three-phase voltages are shown in Figure 4.4.

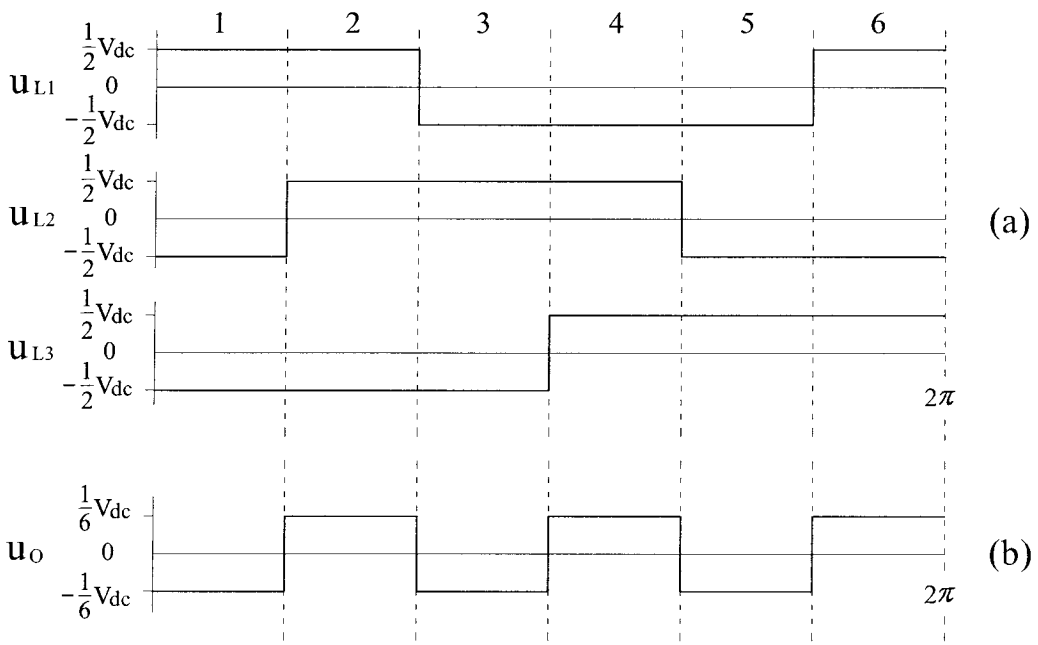

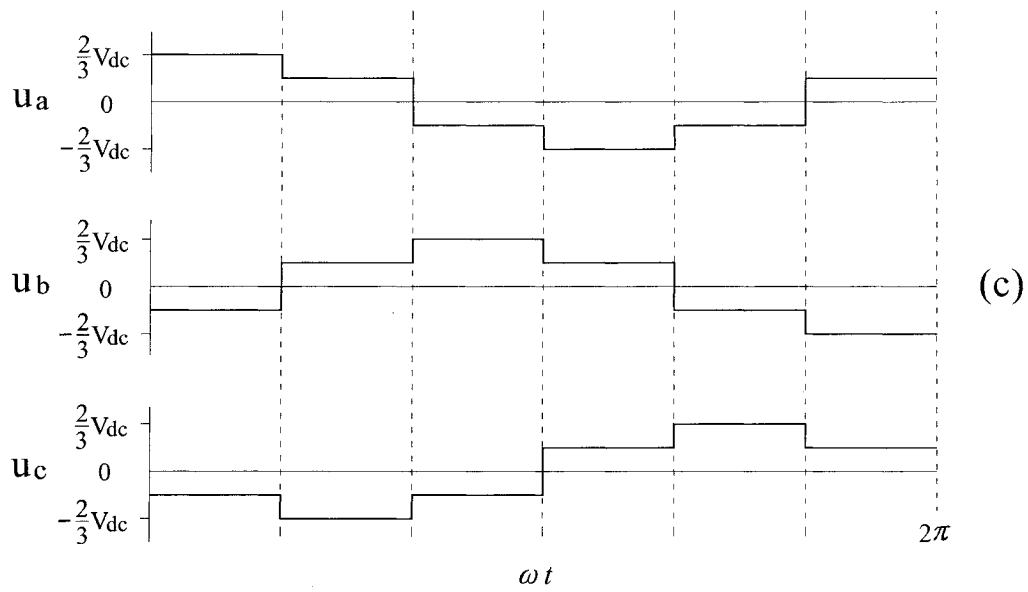

Figure 4.4: Switched three-phase waveforms (a) Pole voltages
(b) Neutral point potential (c) Phase voltages

The three-phase pole voltages, which are the voltages from the inverter output to the neutral point (N point), are constants over every sixth of the fundamental period, assuming one of the two voltage levels is $+V_{dc}/2$ or $-V_{dc}/2$, at a given time. The neutral point potential u_{oN} is either positive with more than one upper half-bridge switch closed, or negative with more than one lower half-bridge switch closed. The respective voltage levels shown in Figure 4.4 (b) hold for symmetrical load impedances.

The waveform of the phase voltage $u_a = u_{L1} - u_{oN}$ is displayed in the upper trace of Figure 4.4(c). It forms a symmetrical, nonsinusoidal three-phase voltage system along with the other phase voltages u_b and u_c. Since the waveform u_{oN} has three times the frequency of $u_{Li}, i = 1,2,3$, and its amplitude equals exactly one third of the amplitudes of u_{Li}, this waveform contains exactly all the third harmonic components of u_{Li}. Since

u_a is equal to $u_{L1} - u_{oN}$, third harmonics are eliminated from the phase voltages. This is also true for the general case of three-phase symmetrical PWM waveforms. As all the third harmonics form zero-sequence systems, they don't produce currents in the induction motor windings. Thus there is no electrical connection to the star-point of the load, i.e., the point *O* and point *N* in Figure 4.3 must not be shorted.

For a three-phase voltage source inverter (Figure 4.3), each pole voltage may assume one of two values (1 or 0) depending on whether the upper or lower switch is turned on. Consequently there are only eight possible operating states for the inverter, i.e., S_0, S_1, ... S_7. For example, with the inverter in active state 1, the inverter state is represented as S_1=100, where "1" indicates that point "*a*" is connected to the upper rail, and "0" indicates that point "*b*" and "*c*" are connected to the lower voltage rail. Therefore, there are six active states for the inverter, i.e., S_1=100, S_2=110, S_3=010, S_4=011, S_5=001 and S_6=101. The two zero states of the inverter occur when the top three switches are closed, or the bottom tree switches are closed, corresponding to state *0*: S_0=000 and state *7*: S_7=111.

The output voltages of the inverter are composed of these eight switch states. Define eight voltage vectors $\boldsymbol{u_0}$, $\boldsymbol{u_1}$, ... , $\boldsymbol{u_7}$ corresponding to the switch states S_0, S_1, ... , S_7, respectively.

From Figure 4.3, the vector $\boldsymbol{u_1}$, for the inverter operating in state S_1 =100, can be calculated as follows.

$$\begin{bmatrix} u_{L1}(t) \\ u_{L2}(t) \\ u_{L3}(t) \end{bmatrix} = \begin{bmatrix} \frac{V_{dc}}{2} \\ -\frac{V_{dc}}{2} \\ -\frac{V_{dc}}{2} \end{bmatrix}. \tag{4.1}$$

Considering the transformation of space vectors discussed in the Chapter 2, we can obtain the following equation:

$$\begin{bmatrix} u_{\alpha}(t) \\ u_{\beta}(t) \end{bmatrix} = \begin{bmatrix} V_{dc} \\ 0 \end{bmatrix}. \tag{4.2}$$

Thus, $\boldsymbol{u_1}$ is a vector lying along the real axis of the complex space of length V_{dc}. Similar calculations can be performed for the remaining seven states of the inverter. The resulting vectors are given in Table 4.1.

Table 4.1: Space vector coordinates

$\boldsymbol{u_s = (u_\alpha, u_\beta)}$							
$\boldsymbol{u_0}$	$\boldsymbol{u_1}$	$\boldsymbol{u_2}$	$\boldsymbol{u_3}$	$\boldsymbol{u_4}$	$\boldsymbol{u_5}$	$\boldsymbol{u_6}$	$\boldsymbol{u_7}$
(0,0)	$(V_{dc},0)$	$(\frac{V_{dc}}{2},\frac{\sqrt{3}V_{dc}}{2})$	$(-\frac{V_{dc}}{2},\frac{\sqrt{3}V_{dc}}{2})$	$(-V_{dc},0)$	$(-\frac{V_{dc}}{2},-\frac{\sqrt{3}V_{dc}}{2})$	$(\frac{V_{dc}}{2},-\frac{\sqrt{3}V_{dc}}{2})$	(0,0)

From Table 4.1, the following operation rules are obtained:

$$\begin{aligned} &\boldsymbol{u_1 = -u_4}, \\ &\boldsymbol{u_2 = -u_5}, \\ &\boldsymbol{u_3 = -u_6}, \\ &\boldsymbol{u_0 = u_7 = 0}, \\ &\boldsymbol{u_1 + u_3 + u_5 = 0}, \\ &\boldsymbol{u_2 + u_4 + u_6 = 0}. \end{aligned} \tag{4.3}$$

The SVM principle is based on the switching between two adjacent active vectors and two zero vectors during one switching period [55, 59]. The vectors discussed above can be plotted on the complex plane as shown in Figure 4.5.

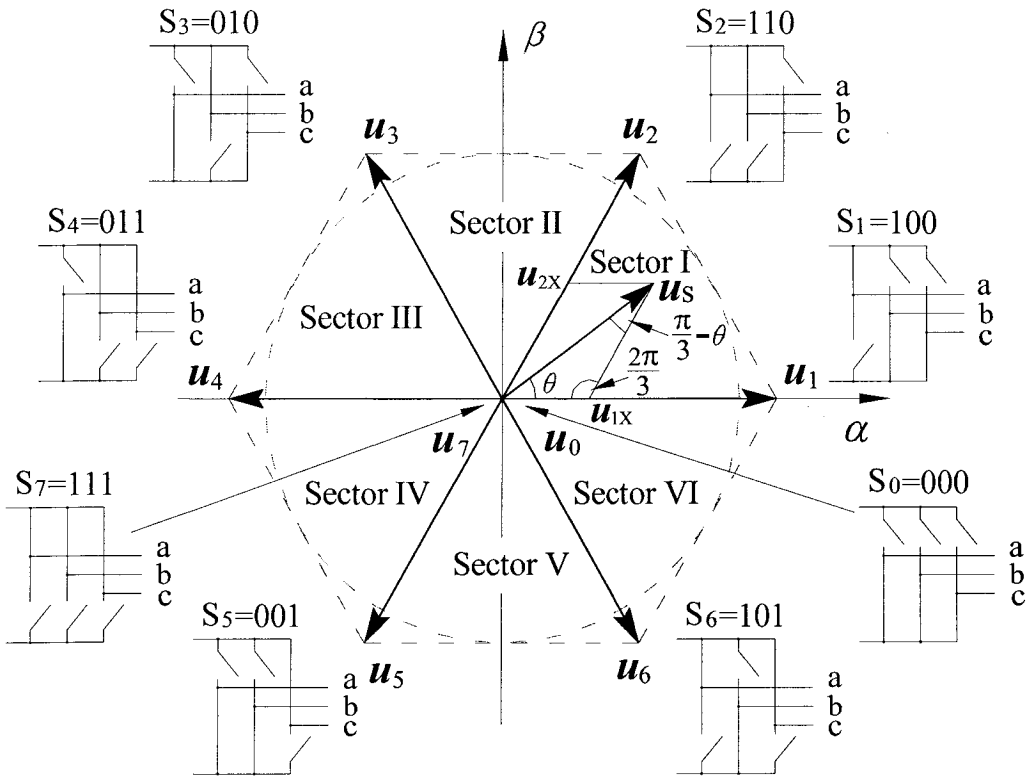

Figure 4.5: Space vectors

Figure 4.5 also shows the position of the inverter switches corresponding to each active states of the inverter. It can be seen that the six active vectors subdivide the space vector plane into six equal sectors.

The rotating voltage vector within the six sectors can be approximated by sampling the vector, then switching between different inverter states during the sampling period. This will produce an approximation of the sampled rotating space vector. By continuously sampling the rotating vector and high frequency switching, the output of the inverter will

be a series of pulses that have a dominant fundamental sine-wave component, corresponding to the rotation frequency of the vector [59]. Instantaneously, the actual vectors produced are not the same as the desired vector; and these instantaneous voltage deviations represent voltage harmonics.

In one sampling interval, the output voltage vector $\boldsymbol{u}_s(t)$ can be written as

$$\boldsymbol{u}_s(t) = \frac{T_0}{T_s}\boldsymbol{u}_0 + \frac{T_1}{T_s}\boldsymbol{u}_1 + \ldots + \frac{T_7}{T_s}\boldsymbol{u}_7, \tag{4.4}$$

where T_0, T_1, ... , T_7 are the turn-on time of the vectors $\boldsymbol{u}_0$, $\boldsymbol{u}_1$, … , $\boldsymbol{u}_7$; T_0, T_1, ... , $T_7 \geq 0$, $\sum_{i=0}^{7} T_i = T_s$, and T_s is the sampling time.

According to Equation (4.3), the decomposition of $\boldsymbol{u}_s$ into $\boldsymbol{u}_0$, $\boldsymbol{u}_1$, … , $\boldsymbol{u}_7$ has infinite ways. However, in order to reduce the number of switching actions and make full use of active turn-on time for space vectors, the vector $\boldsymbol{u}_s$ is commonly split into two nearest adjacent voltage vectors and zero vectors $\boldsymbol{u}_0$ and $\boldsymbol{u}_7$ in an arbitrary sector. For example, in Sector I, and in one sampling interval, vector $\boldsymbol{u}_s$ can be expressed as

$$\boldsymbol{u}_s(t) = \frac{T_0}{T_s}\boldsymbol{u}_0 + \frac{T_1}{T_s}\boldsymbol{u}_1 + \frac{T_2}{T_s}\boldsymbol{u}_2 + \frac{T_7}{T_s}\boldsymbol{u}_7, \tag{4.5}$$

where T_s-T_1-T_2=T_0+$T_7 \geq 0$, $T_0 \geq 0$ and $T_7 \geq 0$.

The required time T_1 to spend in active state $\boldsymbol{u}_1$ is given by the fraction of $\boldsymbol{u}_1$ mapped by the decomposition of the required space vector $\boldsymbol{u}_s$ onto the $\boldsymbol{u}_1$ axis, shown in Figure 4.5 as $\boldsymbol{u}_{1X}$. Therefore,

$$\frac{T_1}{T_s} = \frac{|\boldsymbol{u}_{1X}|}{|\boldsymbol{u}_1|},$$

and similarly

$$\frac{T_2}{T_s} = \frac{|\boldsymbol{u}_{2X}|}{|\boldsymbol{u}_2|}.$$

From Figure 4.5, the amplitude of vector $\boldsymbol{u}_{1X}$ and $\boldsymbol{u}_{2X}$ are obtained in terms of $|\boldsymbol{u}_s|$ and θ.

$$\frac{|\boldsymbol{u}_S|}{\sin(2\pi/3)} = \frac{|\boldsymbol{u}_{2X}|}{\sin(\theta)} = \frac{|\boldsymbol{u}_{1X}|}{\sin(\pi/3 - \theta)}. \tag{4.6}$$

Based on the above equations, the required times to spend in each of the active and zero states are given by

$$T_1 = \frac{T_s |\boldsymbol{u}_s| \sin(\pi/3 - \theta)}{|\boldsymbol{u}_1| \sin(2\pi/3)}, \tag{4.7}$$

$$T_2 = \frac{T_s |\boldsymbol{u}_s| \sin(\pi/3 - \theta)}{|\boldsymbol{u}_2| \sin(2\pi/3)}, \tag{4.8}$$

$$T_z = T_0 + T_7 = T_s - (T_1 + T_2). \tag{4.9}$$

Having computed necessary times to spend in the active and zero states, one can generate the switching signals now. There are various switching sequences that will result in the correct total time slot spent in the required states. If the transition from one switching state to another is made by switching a single switch only, minimum inverter switching frequency is obtained. It is also convenient to begin and end a switching cycle in a zero state. Figure 4.6 shows the rotating vector in Sector I. Two different pulse patterns are shown in Figure 4.7, for a rotating vector sampled in Sector I.

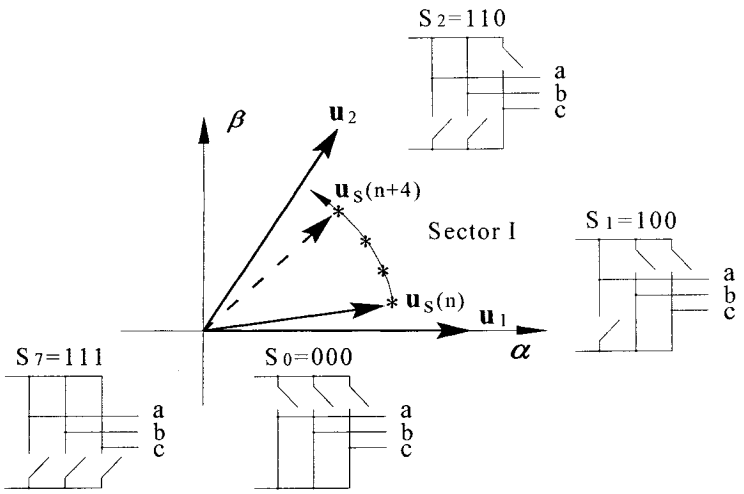

Figure 4.6: A rotating vector in Sector I

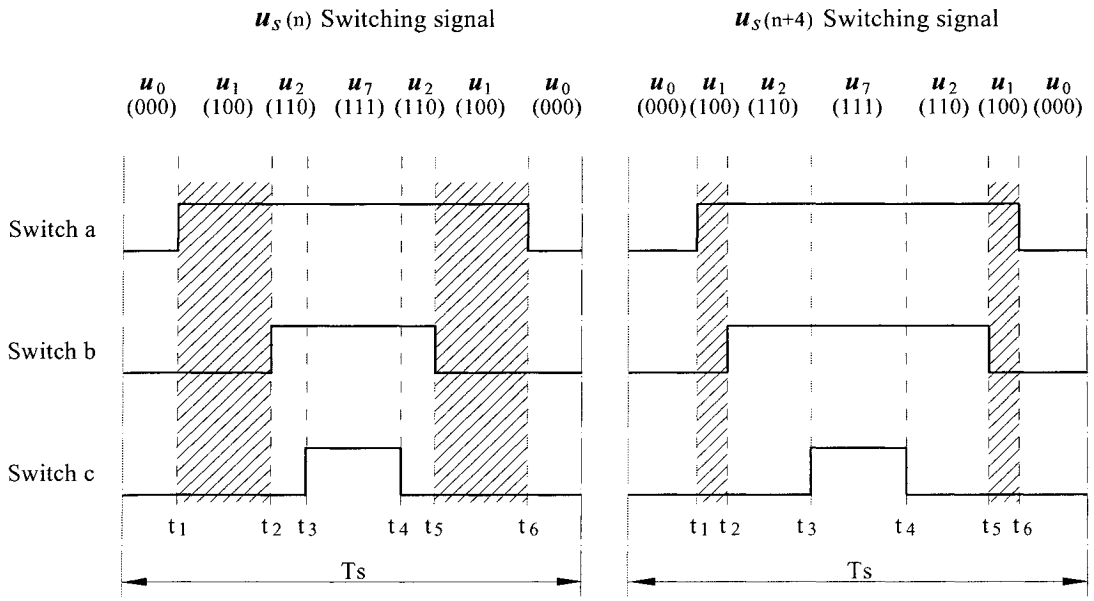

Figure 4.7: Pulse pattern

From Figure 4.7, it can be seen that the inverter starts and ends a switching period T_s in the zero state. It switches for the required length of time into state *1*, then through state *2*

to the other zero state. The reverse of this pattern is then selected to return the inverter to the starting zero state. It can also be seen by the shaded portions in Figure 4.7, that as the reference vector moves towards Sector II, the inverter will spend less switching period in active state *1*.

The vector sequence and timing during one switching period is given in Table 4.2. The requirement of minimal number of commutations per cycle is met when the $\boldsymbol{u}_m$ and $\boldsymbol{u}_n$ vectors are selected regarding to Table 4.3, where $\boldsymbol{u}_m$, $\boldsymbol{u}_n$ are two adjacent voltage vectors in space vector diagram; m, n = 1, 2, 3, 4, 5, 6.

Table 4.2: Time duration for selected vectors

$\boldsymbol{u}_0$	$\boldsymbol{u}_m$	$\boldsymbol{u}_n$	$\boldsymbol{u}_7$	$\boldsymbol{u}_n$	$\boldsymbol{u}_m$	$\boldsymbol{u}_0$
$T_0/4$	$T_m/2$	$T_n/2$	$T_0/2$	$T_n/2$	$T_m/2$	$T_0/4$

Table 4.3: Vector selections in different sectors

Sector	θ	$\boldsymbol{u}_m$	$\boldsymbol{u}_n$
I	0 to $\pi/3$	$\boldsymbol{u}_1$	$\boldsymbol{u}_2$
II	$\pi/3$ to $2\pi/3$	$\boldsymbol{u}_3$	$\boldsymbol{u}_2$
III	$2\pi/3$ to π	$\boldsymbol{u}_3$	$\boldsymbol{u}_4$
IV	π to $4\pi/3$	$\boldsymbol{u}_5$	$\boldsymbol{u}_4$
V	$4\pi/3$ to $5\pi/3$	$\boldsymbol{u}_5$	$\boldsymbol{u}_6$
VI	$5\pi/3$ to 2π	$\boldsymbol{u}_1$	$\boldsymbol{u}_6$

For any vector, the required switching pattern can be determined by the sector in which the reference vector lies. From this information the necessary time to spend in each active and zero state can be calculated based on Equations (4.7), (4.8) and (4.9). Then based on the sector of operation, the necessary inverter switching pulses can be produced.

Figure 4.8 shows the pulse command signals pattern for the inverter when different vectors u_m, u_n and zero vectors u_0 and u_7 are applied.

Sector I (u_1, u_2)

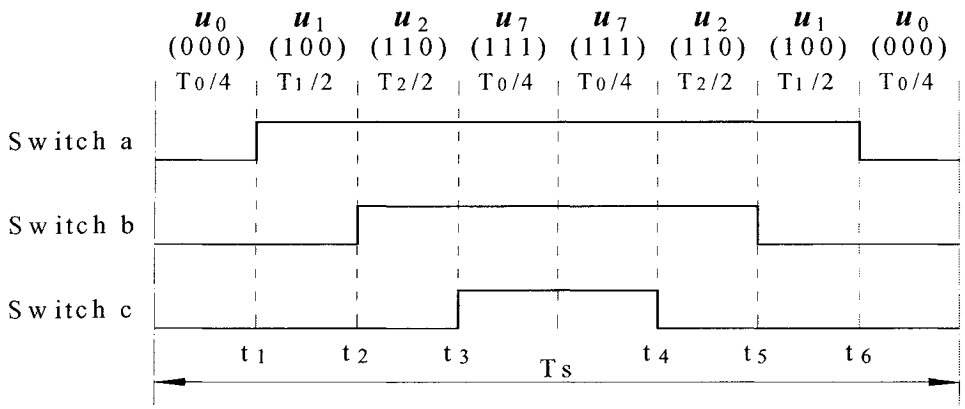

Sector II (u_3, u_2)

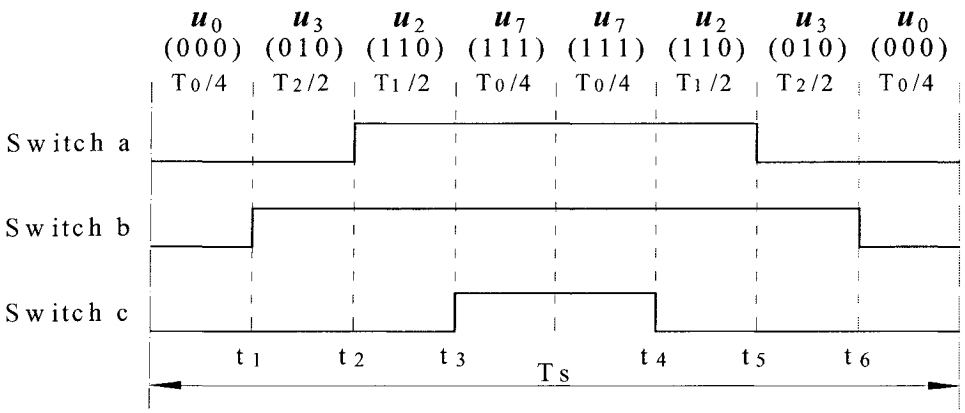

Sector III (u_3, u_4)

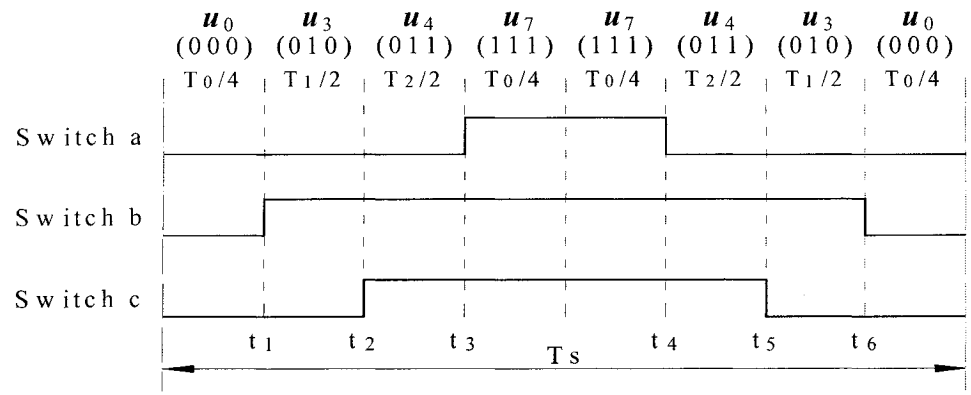

Sector IV (u_5, u_4)

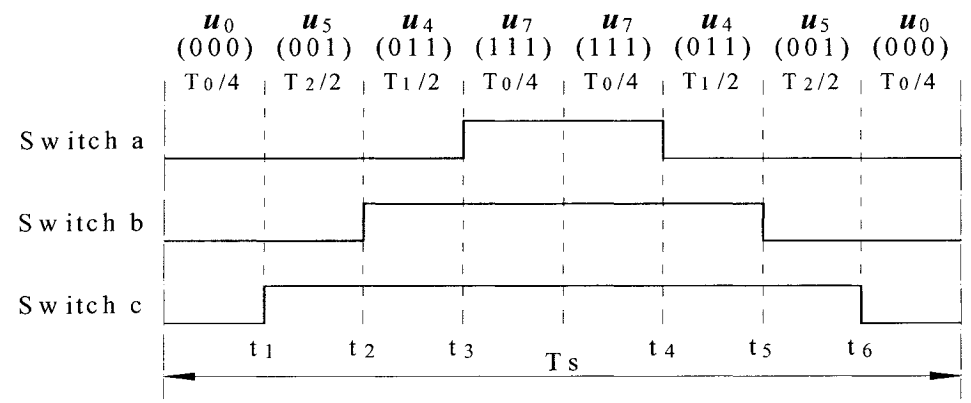

Sector V (u_5, u_6)

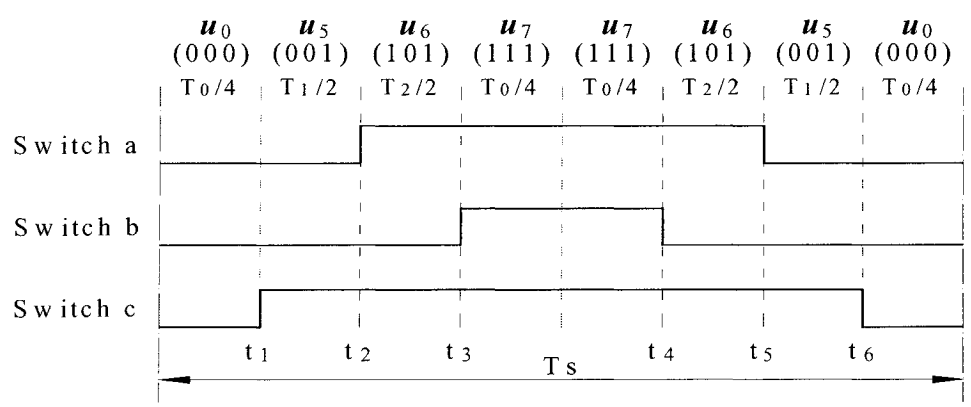

Sector VI (u_1, u_6)

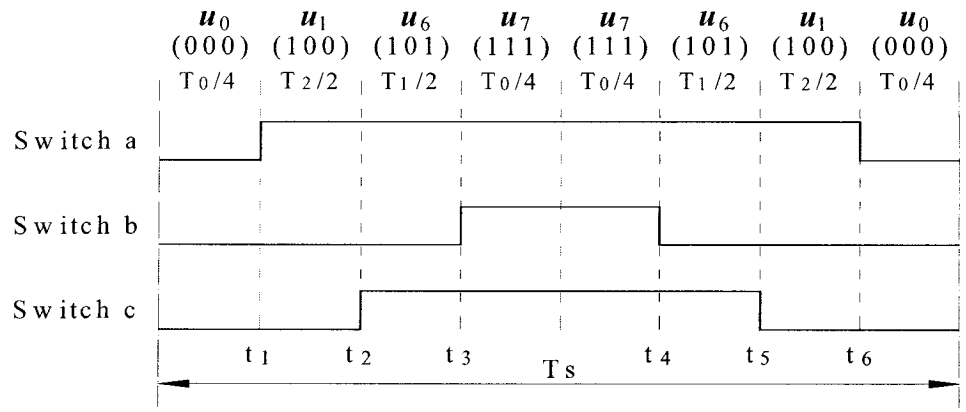

Figure 4.8: Pulse command signals patterns

Based on Figure 4.8, the required time periods to spend in a sampling interval can be given by

$$
\begin{aligned}
t_1 &= \frac{T_z}{4}, \\
t_2 &= \begin{cases} \frac{T_z}{4} + \frac{T_m}{2}, & \text{sec}tor = I,III,V; m = 1,3,5, \ \textit{respectively} \\ \frac{T_z}{4} + \frac{T_n}{2}, & \text{sec}tor = II,IV,VI; n = 3,5,1, \ \textit{respectively} \end{cases}, \\
t_3 &= \frac{T_z}{4} + \frac{T_m + T_n}{2}, \\
t_4 &= \frac{3T_z}{4} + \frac{T_m + T_n}{2}, \\
t_5 &= \begin{cases} \frac{3T_z}{4} + \frac{T_m}{2} + T_{m+1}, & \text{sec}tor = I,III,V; m = 1,3,5, \ \textit{respectively} \\ \frac{3T_z}{4} + \frac{T_n}{2} + T_m, & \text{sec}tor = II,IV,VI; \\ & m = 2,4,6 \ \textit{and} \ n = 3,5,1, \ \textit{respectively} \end{cases}, \\
t_6 &= \frac{3T_z}{4} + T_m + T_n .
\end{aligned}
\tag{4.13}
$$

4.4 The test of the SVM simulation block

The SVM simulation block is implemented in both SIMULINK blocks and M-file S-function. The test model is shown as Figure 4.9.

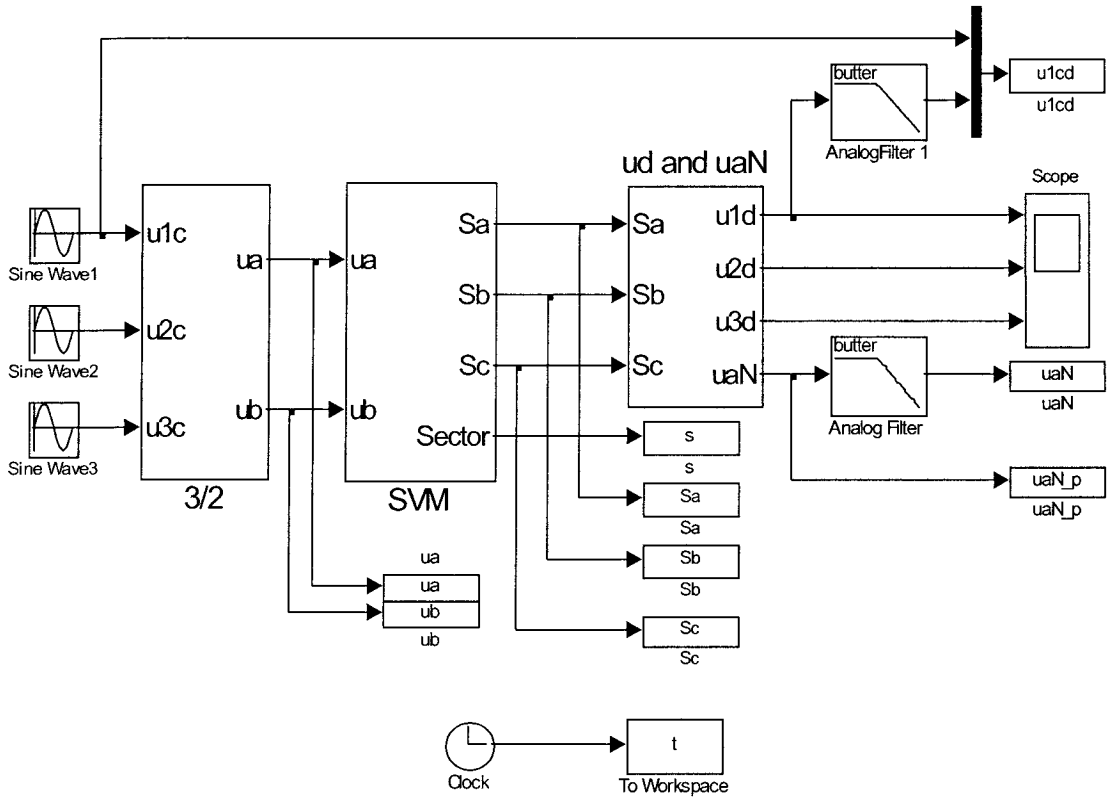

Figure 4.9: Test model of the SVM block

The inputs are three-phase balanced sinusoidal signals:

$$u_{1c} = \sin(2\pi f \cdot t + 4\pi/3),$$

$$u_{2c} = \sin(2\pi f \cdot t + 2\pi/3),$$

$$u_{3c} = \sin(2\pi f \cdot t).$$

Sa, *Sb*, and *Sc* are the switching control signals of the inverter; u_{1d}, u_{2d} and u_{3d} are phase voltages of the induction motor, which are the outputs of the inverter; u_{aN} is pole voltage of phase *a*. The analog filters are 8th order Butterworth low-pass filters, with a passband edge frequency of 159.2Hz (1000rad/sec). The sampling time is 0.001sec.

When the frequency of the input signals *f*=95.5Hz (600rad/sec), the sampled two-phase voltages u_α and u_β are shown in Figure 4.10.

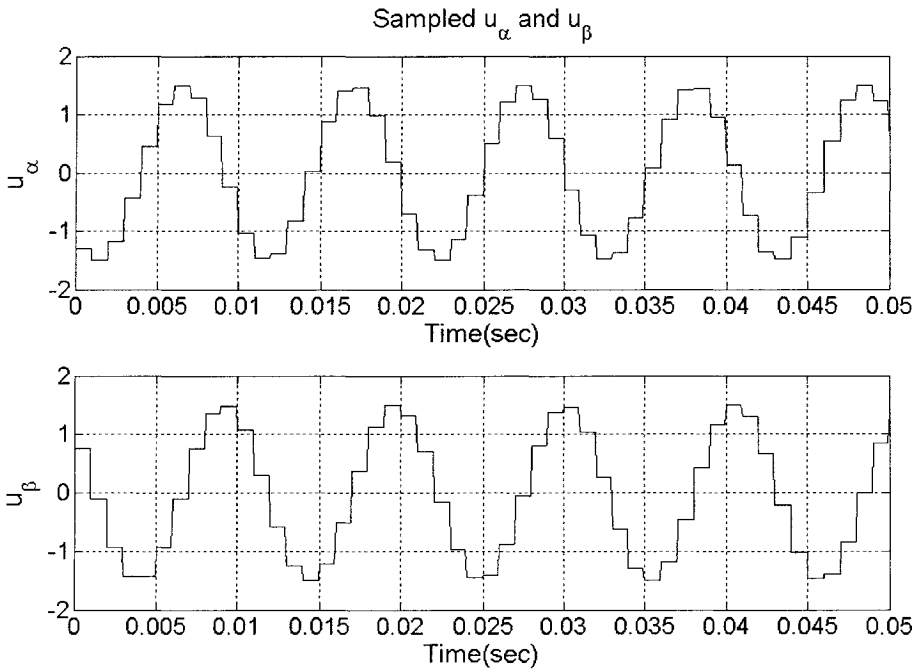

Figure 4.10: Sampled two-phase voltages u_α and u_β

When the frequency of the input signals *f*=95.5Hz (600rad/sec), the switching control signals and the number of sectors mapped by the rotating vector are shown in Figure 4.11.

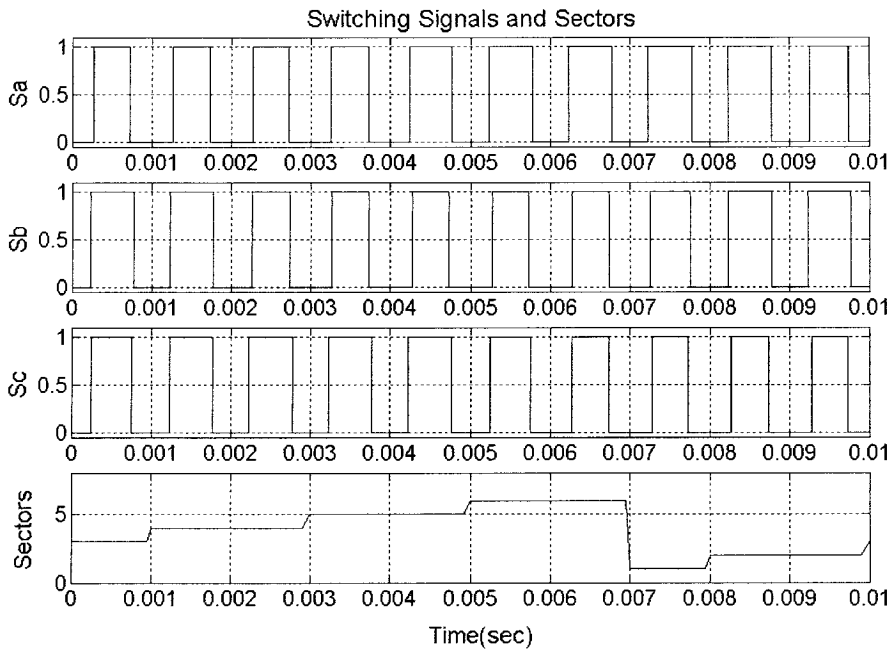

Figure 4.11: Switching signals and sectors

When the frequency of the input signals f=9.55Hz (60rad/sec), the pole voltage of phase a is shown in Figure 4.12, and the filtered pole voltage is shown in Figure 4.13.

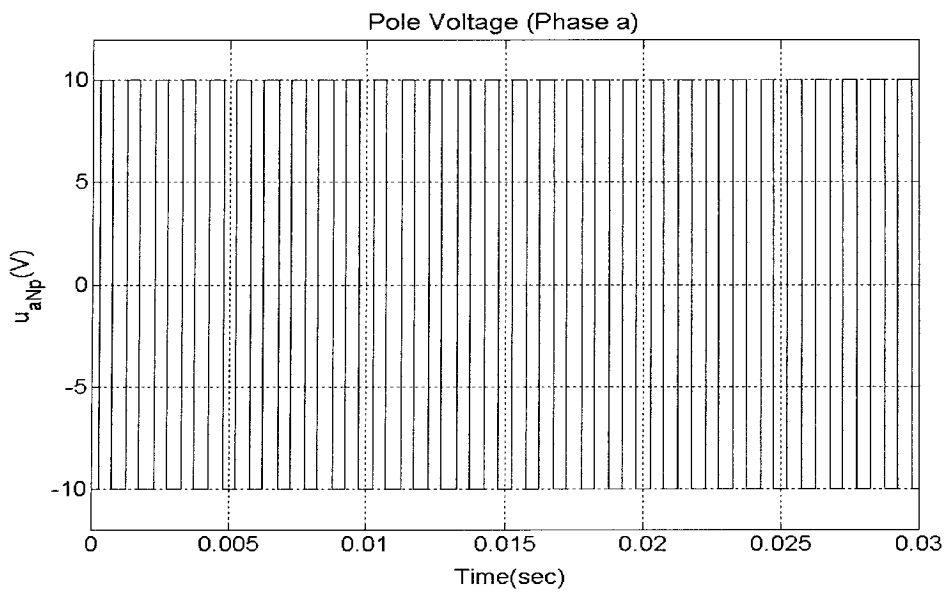

Figure 4.12: Pole voltage

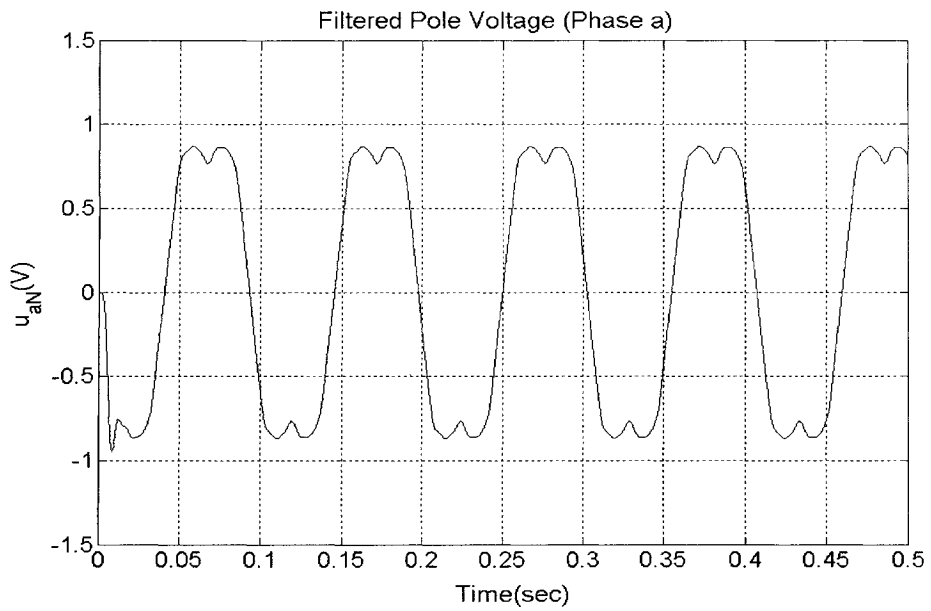

Figure 4.13: Filtered pole voltage

When the frequency of the input signals f=9.55Hz (60rad/sec), the input voltage of phase a, which is the reference input voltage, and the filtered phase voltage of phase a, which is the filtered phase voltage of the inverter's load, are shown in Figure 4.14.

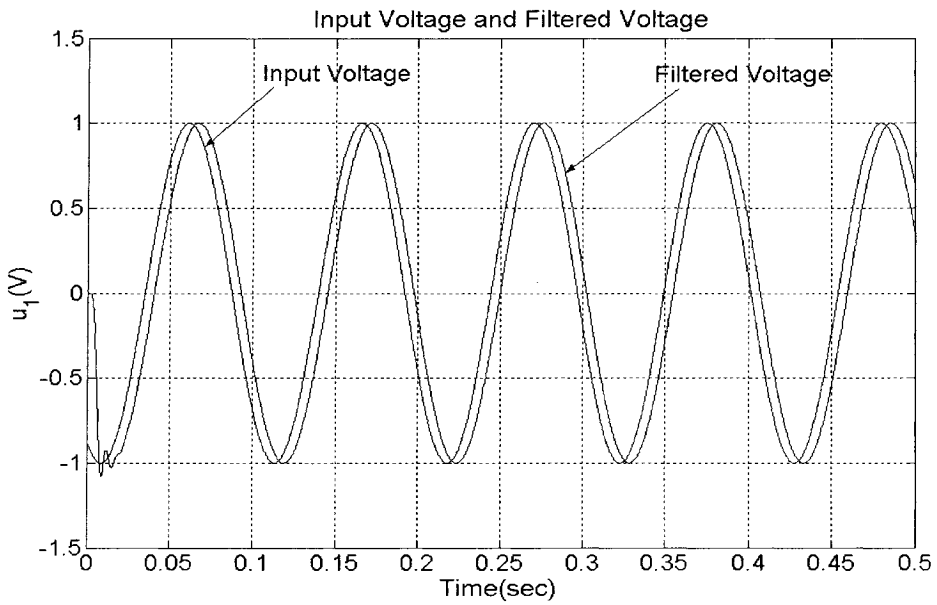

Figure 4.14: Input voltage and filtered phase voltage

4.5 Analysis of test results

From Figure 4.14, it is noted that the filtered phase voltage is nearly the same as the reference input voltage of the inverter except for small phase difference. It shows the SVM works well in signal transformation.

Figure 4.13 and Figure 4.14 show that even though the pole voltage includes the harmonic component, it doesn't appear in the phase voltage. Since the phase voltage is equal to the difference of the pole voltage and the neutral point potential, which contains exactly all the third harmonic components of the pole voltage, the third harmonics are eliminated from the phase voltage.

The simulation results show that the proposed SVM block gives less harmonic distortion and fast transient response.

Remark: Currently, two types of the PWM methods are mainly used in most applications. One is the carrier-based PWM method; another one is the SVM method. The relationship between carrier-based PWM and SVM has been discussed in References [55, 59]. The analysis and comparison results [55, 59] of two PWM methods have theoretically demonstrated that the SVM has wide linear modulation range, less switching loss, and less THD in the spectrum of switching waveform compared with the carrier-based PWM.

Chapter 5
Controller Design

A novel SMC controller of induction motors for HEVs is proposed in this Chapter. The control principle is based on the SMC combined with SVM techniques. The SMC contributes to the robustness of induction motor drives, and the SVM improves the torque, flux, and current steady-state performance by reducing the ripple. The Lyapunov direct method is used to ensure the reaching and sustaining of the sliding mode and stability of the control system.

5.1 Selection of sliding surfaces

The SMC design objective is to make the modulus of the rotor flux vector ψ_r, and torque T track to their reference value ψ_{ref} and T_{ref}, respectively.

The transient dynamic response of the system is dependent on the selection of the sliding surfaces. The selection of the sliding surfaces is not unique. According to References [68, 69], the higher-order sliding modes can be selected; however it demands more information in implementation. Considering the SMC design for an induction motor supplied through an inverter (Figure 4.3), we define two sliding surfaces:

$$s_1 = T_{ref} - \hat{T}\,, \tag{5.1}$$

$$s_2 = K(\psi_{ref} - \hat{\psi}_r) + \frac{d}{dt}(\psi_{ref} - \hat{\psi}_r)\,. \tag{5.2}$$

The positive constant K determines the convergent speed of rotor flux. Once the system is driven into sliding surfaces, the system behavior will be determined by $s_1 = 0$ and $s_2 = 0$ in Equations (5.1) and (5.2). The objective of control design is to force the system into sliding surfaces so that the torque and rotor flux signal will follow the respective reference signals.

5.2 Projection of the system motion

In order to simplify the design process, the time derivative of sliding surfaces' function s can be decoupled with respect to the two-phase stator voltage vectors $\boldsymbol{u}_s$.

The time derivative of the torque in Equation (2.11) can be derived as:

$$\dot{T} = \frac{3P}{2}\frac{L_m}{L_r}(\dot{i}_\beta\psi_\alpha + \dot{\psi}_\alpha i_\beta - \dot{i}_\alpha\psi_\beta + \dot{\psi}_\beta i_\alpha)$$

$$= \frac{3P}{2}\frac{L_m}{L_r}\left[\frac{1}{\sigma L_s}(-\frac{L_m}{L_r}\dot{\psi}_\beta - R_s i_\beta + u_\beta)\psi_\alpha - \frac{1}{\sigma L_s}(-\frac{L_m}{L_r}\dot{\psi}_\alpha - R_s i_\alpha + u_\alpha)\psi_\alpha \right.$$

$$\left. + \dot{\psi}_\alpha i_\beta - \dot{\psi}_\beta i_\alpha\right]$$

$$= \frac{3P}{2}\frac{L_m}{L_r}\left[-(\frac{L_m}{\sigma L_s L_r}\psi_\alpha + i_\alpha)\dot{\psi}_\beta + (\frac{L_m}{\sigma L_s L_r}\psi_\beta + i_\beta)\dot{\psi}_\alpha + \frac{R_s}{\sigma L_s}(\psi_\beta i_\alpha - \psi_\alpha i_\beta)\right.$$

$$\left. + \frac{1}{\sigma L_s}(\psi_\alpha u_\beta - \psi_\beta u_\alpha)\right]$$

$$= \frac{3P}{2}\frac{L_m}{L_r}\left[-\left(\frac{L_m}{\sigma L_s L_r}\psi_\alpha + i_\alpha\right)\left(-\frac{1}{\tau}\psi_\beta + \omega\psi_\alpha + \frac{L_m}{\tau} i_\beta\right) + \frac{R_s}{\sigma L_s}(\psi_\beta i_\alpha - \psi_\alpha i_\beta)\right.$$

$$\left. + \left(\frac{L_m}{\sigma L_s L_r}\psi_\beta + i_\beta\right)\left(-\frac{1}{\tau}\psi_\alpha - \omega\psi_\beta + \frac{L_m}{\tau} i_\alpha\right) + \frac{1}{\sigma L_s}(\psi_\alpha u_\beta - \psi_\beta u_\alpha)\right]$$

$$= \frac{3P}{2}\frac{L_m}{L_r}\left[-\frac{L_m}{\sigma L_s L_r}\omega\psi_r^2 + \frac{R_s L_r + R_r L_s}{\sigma L_s L_r}(\psi_\beta i_\alpha - \psi_\alpha i_\beta) - \omega(\psi_\beta i_\beta + \psi_\alpha i_\alpha)\right.$$

$$\left. + \frac{1}{\sigma L_s}(\psi_\alpha u_\beta - \psi_\beta u_\alpha)\right]. \qquad (5.3)$$

Consider

$$\dot{\psi}_r = \frac{d}{dt}\left(\sqrt{\psi_\alpha^2 + \psi_\beta^2}\right) = \frac{1}{\psi_r}(\psi_\alpha\dot{\psi}_\alpha + \psi_\beta\dot{\psi}_\beta)$$

$$= \frac{1}{\psi_r}\left(-\frac{1}{\tau}\psi_\alpha^2 - \omega\psi_\alpha\psi_\beta + \frac{L_m}{\tau}\psi_\alpha i_\alpha - \frac{1}{\tau}\psi_\beta^2 + \omega\psi_\alpha\psi_\beta + \frac{L_m}{\tau}\psi_\beta i_\beta\right)$$

$$= -\frac{1}{\tau}\psi_r + \frac{L_m}{\tau}\frac{(\psi_\alpha i_\alpha + \psi_\beta i_\beta)}{\psi_r}. \qquad (5.4)$$

The following equation can be obtained

$$(\psi_\alpha i_\alpha + \psi_\beta i_\beta) = \frac{\tau}{L_m}\psi_r\dot{\psi}_r + \frac{1}{L_m}\psi_r^2. \qquad (5.5)$$

Considering Equation (5.5) and the equation $T = \frac{3P}{2}\frac{L_m}{L_r}(i_\beta\psi_\alpha - i_\alpha\psi_\beta)$ (2.11), one can write Equation (5.3) as

$$\dot{T} = \frac{3P}{2}\frac{L_m}{L_r}\left[-(\frac{1}{L_m}+\frac{L_m}{\sigma L_s L_r})\omega\psi_r^2 - \frac{2}{3P}\frac{R_s L_r + R_r L_s}{\sigma L_m L_s}T - \omega\frac{\tau}{L_m}\psi_r\dot{\psi}_r\right.$$

$$\left.+\frac{1}{\sigma L_s}(\psi_\alpha u_\beta - \psi_\beta u_\alpha)\right]$$

$$= -\frac{3P}{2}\frac{1}{\sigma L_r}\omega\psi_r^2 - \frac{3P}{2}\frac{1}{R_r}\omega\psi_r\dot{\psi}_r - \frac{R_s L_r + R_r L_s}{\sigma L_s L_r}T$$

$$+\frac{3P}{2}\frac{L_m}{\sigma L_s L_r}(\psi_\alpha u_\beta - \psi_\beta u_\alpha). \tag{5.6}$$

The second derivative of the rotor flux ψ_r can be written as:

$$\ddot{\psi}_r = \frac{d}{dt}\left[\frac{d}{dt}(\sqrt{\psi_\alpha^2+\psi_\beta^2})\right]$$

$$= \frac{d}{dt}\left[(\psi_\alpha^2+\psi_\beta^2)^{-\frac{1}{2}}(\psi_\alpha\dot{\psi}_\alpha+\psi_\beta\dot{\psi}_\beta)\right] = \frac{d}{dt}\left[\psi_r^{-1}(\psi_\alpha\dot{\psi}_\alpha+\psi_\beta\dot{\psi}_\beta)\right]$$

$$= -\frac{1}{\psi_r^2}\dot{\psi}_r(\psi_\alpha\dot{\psi}_\alpha+\psi_\beta\dot{\psi}_\beta)+\frac{1}{\psi_r}\frac{d}{dt}(\psi_\alpha\dot{\psi}_\alpha+\psi_\beta\dot{\psi}_\beta). \tag{5.7}$$

From Equation (2.11), the following equations can be yielded

$$(\psi_\alpha\dot{\psi}_\alpha+\psi_\beta\dot{\psi}_\beta)$$

$$= \psi_\alpha(-\frac{1}{\tau}\psi_\alpha - \omega\psi_\beta + \frac{L_m}{\tau}i_\alpha) + \psi_\beta(-\frac{1}{\tau}\psi_\beta + \omega\psi_\alpha + \frac{L_m}{\tau}i_\beta)$$

$$= -\frac{1}{\tau}\psi_r^2 + \frac{L_m}{\tau}(\psi_\alpha i_\alpha + \psi_\beta i_\beta), \tag{5.8}$$

$$\frac{d}{dt}(\psi_\alpha \dot{\psi}_\alpha + \psi_\beta \dot{\psi}_\beta)$$

$$= -\frac{2}{\tau}\psi_r \dot{\psi}_r + \frac{L_m}{\tau}(\dot{\psi}_\alpha i_\alpha + \dot{i}_\alpha \psi_\alpha + \dot{\psi}_\beta i_\beta + \dot{i}_\beta \psi_\beta)$$

$$= -\frac{2}{\tau}\psi_r \dot{\psi}_r - \frac{L_m(R_s L_r + L_s R_r)}{\sigma\tau \cdot L_s L_r}(\psi_\alpha i_\alpha + \psi_\beta i_\beta) + \frac{L_m}{\tau}\omega(\psi_\alpha i_\beta - \psi_\beta i_\alpha)$$

$$+\left(\frac{L_m}{\tau}\right)^2 (i_\alpha^2 + i_\beta^2) + \frac{L_m^2}{\sigma\tau^2 L_s L_r}\psi_r^2 + \frac{L_m}{\sigma\tau \cdot L_s}(\psi_\alpha u_\alpha + \psi_\beta u_\beta). \qquad (5.9)$$

Using Equations (5.8), (5.9), and the equation $T = \frac{3P}{2}\frac{L_m}{L_r}(i_\beta \psi_\alpha - i_\alpha \psi_\beta)$ (2.11), one can write Equation (5.7) as:

$$\ddot{\psi}_r = -\frac{1}{\psi_r^2}\dot{\psi}_r\left[-\frac{1}{\tau}\psi_r^2 + \frac{L_m}{\tau}(\psi_\alpha i_\alpha + \psi_\beta i_\beta)\right]$$

$$+\frac{1}{\psi_r}\left[-\frac{2}{\tau}\psi_r \dot{\psi}_r - \frac{L_m(R_s L_r + L_s R_r)}{\sigma\tau \cdot L_s L_r}(\psi_\alpha i_\alpha + \psi_\beta i_\beta) + \frac{L_m}{\tau}\omega(\psi_\alpha i_\beta - \psi_\beta i_\alpha)\right.$$

$$\left.+\left(\frac{L_m}{\tau}\right)^2 (i_\alpha^2 + i_\beta^2) + \frac{L_m^2}{\sigma\tau^2 L_s L_r}\psi_r^2 + \frac{L_m}{\sigma\tau \cdot L_s}(\psi_\alpha u_\alpha + \psi_\beta u_\beta)\right]$$

$$= -\frac{1}{\tau}\dot{\psi}_r + \frac{L_m^2}{\sigma\tau^2 L_s L_r}\psi_r + \frac{2}{3P}R_r \omega \frac{1}{\psi_r}T + \frac{1}{\psi_r}\frac{L_m}{\sigma\tau \cdot L_s}(\psi_\alpha u_\alpha + \psi_\beta u_\beta)$$

$$-\left(\frac{1}{\psi_r}\frac{L_m}{\tau}\dot{\psi}_r + \frac{L_m(R_s L_r + L_s R_r)}{\sigma\tau \cdot L_s L_r}\right)\frac{\psi_\alpha i_\alpha + \psi_\beta i_\beta}{\psi_r} + \frac{1}{\psi_r}\left(\frac{L_m}{\tau}\right)^2 (i_\alpha^2 + i_\beta^2). \qquad (5.10)$$

From Equations (2.14), (2.20) and (5.10), the following equation can be yielded:

$$\ddot{\psi}_r = -\frac{2}{\tau}\dot{\psi}_r - \frac{R_s R_r}{\sigma L_s L_r}\psi_r + \frac{2}{3P}R_r\omega\frac{T}{\psi_r} + \left(\frac{2}{3P}\right)^2 R^2\frac{T^2}{\psi_r^3} + \frac{1}{\psi_r}\frac{L_m}{\sigma\tau\cdot L_s}(\psi_\alpha u_\alpha + \psi_\beta u_\beta). \quad (5.11)$$

Considering Equations (5.6) and (5.11), one can derive the projection of the system motion in the subspaces s_1 and s_2:

$$\dot{s}_1 = \dot{T}_{ref} - \dot{\hat{T}}$$

$$= \dot{T}_{ref} + \frac{3P}{2}\frac{1}{\sigma L_r}\hat{\omega}\hat{\psi}_r^2 + \frac{3P}{2}\frac{1}{R_r}\hat{\omega}\hat{\psi}_r\cdot\dot{\hat{\psi}}_r + \frac{R_s L_r + R_r L_s}{\sigma L_s L_r}\hat{T}$$

$$-\frac{3P}{2}\frac{L_m}{\sigma L_s L_r}(\hat{\psi}_\alpha u_\beta - \hat{\psi}_\beta u_\alpha), \quad (5.12)$$

$$\dot{s}_2 = K(\dot{\psi}_{ref} - \dot{\hat{\psi}}_r) + \frac{d}{dt}(\dot{\psi}_{ref} - \dot{\hat{\psi}}_r)$$

$$= K\dot{\psi}_{ref} + \ddot{\psi}_{ref} + (\frac{2}{\tau} - K)\dot{\hat{\psi}}_r + \frac{R_s R_r}{\sigma L_s L_r}\hat{\psi}_r - \frac{2}{3P}R_r\hat{\omega}\frac{\hat{T}}{\hat{\psi}_r} - \left(\frac{2}{3P}\right)^2 R_r^2\frac{\hat{T}^2}{\hat{\psi}_r^3}$$

$$-\frac{1}{\hat{\psi}_r}\frac{L_m}{\sigma\tau\cdot L_s}(\hat{\psi}_\alpha u_\alpha + \hat{\psi}_\beta u_\beta). \quad (5.13)$$

Therefore, the projection of system motion in the subspaces s_1, s_2 can be expressed as

$$\frac{d\boldsymbol{s}}{dt} = \boldsymbol{f} + \boldsymbol{A}\boldsymbol{u}, \quad (5.14)$$

where $\boldsymbol{f} = [f_1\ f_2]^T$, $\boldsymbol{u} = [u_\alpha\ u_\beta]^T$ and $\boldsymbol{s} = [s_1\ s_2]^T$.

From Equations (5.12) and (5.13), functions f_1, f_2 and matrix $\boldsymbol{A}$ can be obtained as follows:

$$f_1 = \dot{T}_{ref} + \frac{3P}{2}\left(\frac{1}{R_r}\hat{\psi}_r \cdot \dot{\hat{\psi}}_r + \frac{1}{\sigma L_r}\hat{\psi}_r^2\right)\cdot\hat{\omega} + \frac{1}{\sigma}\left(\frac{R_s}{L_s} + \frac{1}{\tau}\right)\hat{T}, \tag{5.15}$$

$$f_2 = K\dot{\psi}_{ref} + \ddot{\psi}_{ref} + \frac{R_s}{\sigma\tau \cdot L_s}\hat{\psi}_r - \frac{2}{3P}R_r\frac{\hat{T}}{\hat{\psi}_r}\hat{\omega} - \left(\frac{2}{3P}\right)^2 R_r^2\frac{\hat{T}^2}{\hat{\psi}_r^3} + \left(\frac{2}{\tau} - K\right)\dot{\hat{\psi}}_r, \tag{5.16}$$

$$\boldsymbol{A} = \begin{bmatrix} a_1\hat{\psi}_\beta & -a_1\hat{\psi}_\alpha \\ a_2\hat{\psi}_\alpha & a_2\hat{\psi}_\beta \end{bmatrix}, \tag{5.17}$$

where $a_1 = \frac{3P}{2}\frac{L_m}{\sigma L_s L_r}$ and $a_2 = -\frac{1}{\hat{\psi}_r}\frac{L_m}{\sigma\tau \cdot L_s}$; $\hat{\omega}$ is the estimated rotor angle velocity.

5.3 Invariant transformation of sliding surfaces

In order to solve the problem of motion stability in subspace $\boldsymbol{s}$, the invariant transformations of equations of discontinuity surfaces is necessary. Consider the following nonlinear system

$$\dot{\boldsymbol{x}} = \boldsymbol{g}(x,t) + \boldsymbol{B}(x,t)\boldsymbol{u}, \tag{5.18}$$

where $\boldsymbol{x} \in R^n$ and $\boldsymbol{u} \in R^m$; $\boldsymbol{g}(x,t)$ and $\boldsymbol{B}(x,t)$ are continuous vector and matrix of dimension $(n \times 1)$ and $(n \times m)$, respectively.

Formally, a standard statement of the control problems is to choose such a discontinuous control $\boldsymbol{u}$, functionally or operationally dependent upon the system state, time and disturbances, that brings an appropriate transformation of the solution to the initial system (5.18). According to Reference [31], a multivariable system may be decoupled into lower-dimensional independent subsystems by means of a deliberate introduction of sliding modes and use of their properties. In the system Equation (5.18) featured by the vector valued controls each component of which is discontinuous on the

corresponding surface, sliding motions occur in some domain belonging to the manifold of the intersection of m discontinuous surfaces $s_i(x)=0$ $(i=1,...,m)$ having the dimension (n-m). The motion occurring on the (n-m)-order manifold is the same as the m-order manifold, only the ways of organizing the sliding motion on the manifold are different [31]. It turns out that the sliding motion is invariant to the linear transformations of discontinuous surfaces and the initial control vector $\boldsymbol{u}$. Such transformations will be employed in designing this control system.

From Equations (5.15) and (5.16), it is noted that functions f_1 and f_2 do not depend on either u_α or u_β, and $\boldsymbol{A}$ is a nonsingular matrix. Therefore, the transformed sliding surfaces, $\boldsymbol{q}=[q_1 \ q_2]^T$, can be introduced to simplify the design process and to construct the candidate Lyapunov function in the next subsection. $\boldsymbol{q}$ and $\boldsymbol{s}$ are related by an invariant transformation:

$$\boldsymbol{q}=\boldsymbol{A}^T\boldsymbol{s}. \tag{5.19}$$

Remark 1: According to Reference [31], the purpose of invariant transformation is to choose the easiest implementation of the SMC technique from the entire set of feasible techniques. A linear invariant transformation of a discontinuous surface has no effect upon the equivalent control value on the manifolds $\boldsymbol{s}=0$ or $\boldsymbol{q}=0$.

5.4 Selection of the control law

A control system design should start with the stability problem traditionally posed throughout the entire history of the control theory. The Lyapunov function is one of the methods for controller design and stability analysis for nonlinear systems.

In this research, the direct Lyapunov method is used to design control law and analyze the stability. Considering the Lyapunov function candidate $v = 0.5\boldsymbol{s}^T\boldsymbol{s} \geq 0$, one obtains its time derivative as:

$$\dot{v} = \boldsymbol{s}^T(\boldsymbol{f} + \boldsymbol{A}\boldsymbol{u}). \tag{5.20}$$

Select the control law as

$$u_\alpha = -k_1\, sgn(q_1) - k_2 q_1, \tag{5.21a}$$

$$u_\beta = -k_1\, sgn(q_2) - k_2 q_2, \tag{5.21b}$$

where $\text{sgn}(q_i) = \begin{cases} +1\ , & q_i > 0 \\ -1\ , & q_i < 0 \end{cases}$, i=*1, 2* and k_1, k_2 are positive constants.

Theorem: Consider the induction motor (2.11), with the developed sliding-mode controller (5.21) and stable sliding surfaces (5.1) and (5.2). If k_1, k_2 are chosen so that $(k_1 + k_2 \mid q_i \mid) > \max(f_i^*)$, where i=*1, 2* and $[f_1^* \ \ f_2^*]^T = \boldsymbol{A}^{-1}\boldsymbol{f}$, the reaching condition of sliding surface $\dot{v} = \boldsymbol{s}^T\dot{\boldsymbol{s}} < 0$ is satisfied, and control system is stabilized.

Proof: From the time derivative of the Lyapunov function (5.20), the following equation can be derived:

$$\begin{aligned} \dot{v} &= \boldsymbol{s}^T(\boldsymbol{f} + \boldsymbol{A}\boldsymbol{u}) \\ &= \boldsymbol{q}^T\boldsymbol{A}^{-1}\boldsymbol{f} + \boldsymbol{q}^T\boldsymbol{u} \\ &= [q_1 \quad q_2]\cdot\begin{bmatrix} f_1^* \\ f_2^* \end{bmatrix} + [q_1 \quad q_2]\cdot\begin{bmatrix} -k_1\,\text{sgn}(q_1) - k_2 q_1 \\ -k_1\,\text{sgn}(q_2) - k_2 q_2 \end{bmatrix} \end{aligned}$$

$$= \left[q_1 f_1^* + q_2 f_2^*\right] + \left[-k_1 q_1 \operatorname{sgn}(q_1) - k_2 q_1^2 - k_1 q_2 \operatorname{sgn}(q_2) - k_2 q_2^2\right]$$

$$= \left[q_1 f_1^* + q_2 f_2^*\right] + \left[-k_1 |q_1| - k_2 q_1^2 - k_1 |q_2| - k_2 q_2^2\right]$$

$$= (q_1 f_1^* - k_1 |q_1| - k_2 q_1^2) + (q_2 f_2^* - k_1 |q_2| - k_2 q_2^2), \quad (5.22)$$

From Equation (5.22), it is noted that if one chooses $(k_1+k_2 |q_i|) > \max(f_i^*)$, where *i=1, 2*, then the time derivative of the Lyapunov function $\dot{v} < 0$. Thus, the origin in the space $\boldsymbol{q}$ (and in the space $\boldsymbol{s}$ as well) is asymptotically stable, and the reaching condition of the sliding surface is guaranteed. The torque $\hat{T}$ and rotor flux $\hat{\psi}_r$ will approach to the reference torque and reference rotor flux, respectively.

Remark 2: Since $\boldsymbol{A}$ is a nonsingular matrix, equation $[f_1^* \ f_2^*]^T = \boldsymbol{A}^{-1}\boldsymbol{f}$ exists. Therefore, the transformed sliding surfaces, $\boldsymbol{q} = [q_1 \ q_2]^T$, can be introduced to simplify the time derivative of the Lyapunov function.

Remark 3: From Equation (5.21), it is observed that the control command u_α is used to force the sliding mode arises in the manifold $q_1=0$, while u_β is used to force the sliding mode arises in the manifold $q_2=0$. The sliding mode arising in the manifold $q_i=0$ (i=1, 2) is equivalent to its occurrence on the manifold $s_i=0$ (i=1, 2). After the sliding mode arises on the intersection of both surfaces s_1=0 and s_2=0, then $\hat{T} = T_{ref}$ and $\hat{\psi} = \psi_{ref}$. Therefore, a complete decoupled control of torque and flux is obtained.

Remark 4: The selection of the control law is under consideration of the requirement of the SVM technique for VSI. The control law is the combination of a discontinuous function and a continuous function. The continuous function can improve the

performance of the SVM while the discontinuous function is used to ensure robustness of the control system.

Remark 5: In order to meet the requirements of HEV applications, the chattering phenomenon should be considered besides the stability of induction motor control systems. It is well known that sliding-mode techniques generate undesirable chattering and cause the torque, flux, and current ripple in the system. However, in the new control system, due to the SVM technique giving a large linear control range and the regular logic control signals for the inverter, which means less harmonic distortion, the chattering can be effectively reduced.

Chapter 6
Simulations

In this chapter, we present simulation results showing the efficacy of the proposed new speed-sensorless sliding-mode control method (SMC with SVM). Also, we present some comparative results with the classical PI (FOC) [25], the NSFC (FOC) [26], conventional SMC [36] and FSMC [34] control methods in terms of the current, flux, and torque performance, robustness and disturbance rejection ability.

For the proposed new control method, the sliding-mode observer discussed in Chapter 3 is used in simulation for the estimation of the rotor flux and the torque of an induction motor without speed sensors, and the SVM technique discussed in Chapter 4 is adopted to produce the logic control signals for the VSI. The scheme of control system is shown in Figure 6.

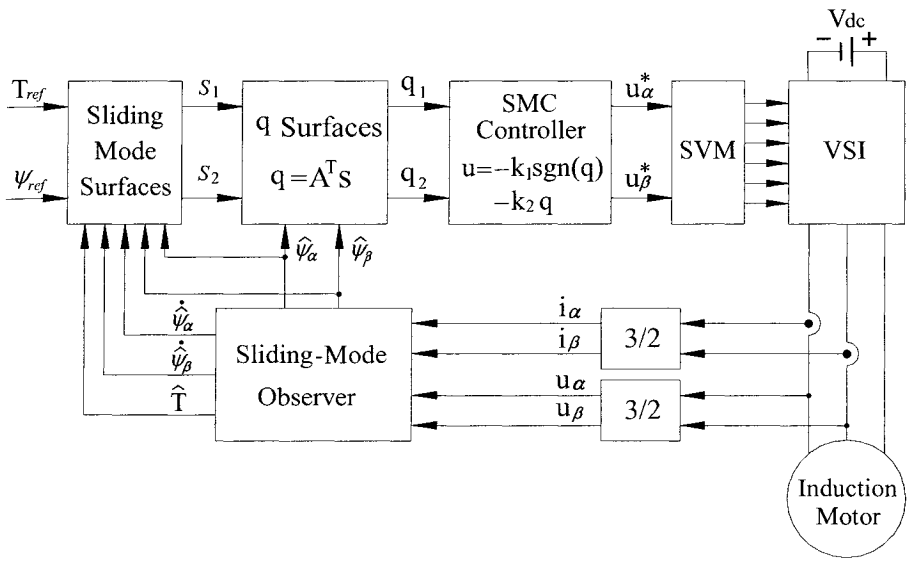

Figure 6.1: SMC with SVM control system

For other compared control systems, the same sliding-mode observer is adopted. In order to enhance the compared effect, the SVM is used in the classical PI control system to improve the system performance. For the NSFC control system and FSMC control system, in which fuzzy system is used to design the discontinuous SMC control terms, the SMC method is used to implement the logic signals control for the VSI. In the conventional SMC control system, the discontinuous system control signals are directly adopted as the logic control signals for the VSI, which is one of the advantages of the conventional SMC by means of the simple implementation for PWM. This also turns out to be one of the major differences between the conventional SMC and the proposed new SMC method with SVM. For the classical PI and the NSFC control systems, the parameters of the PI controller are tuned by trial and error method to achieve the "best" control performance. The schemes of control systems are shown in Figure 6.2, 6.3, 6.4 and 6.5.

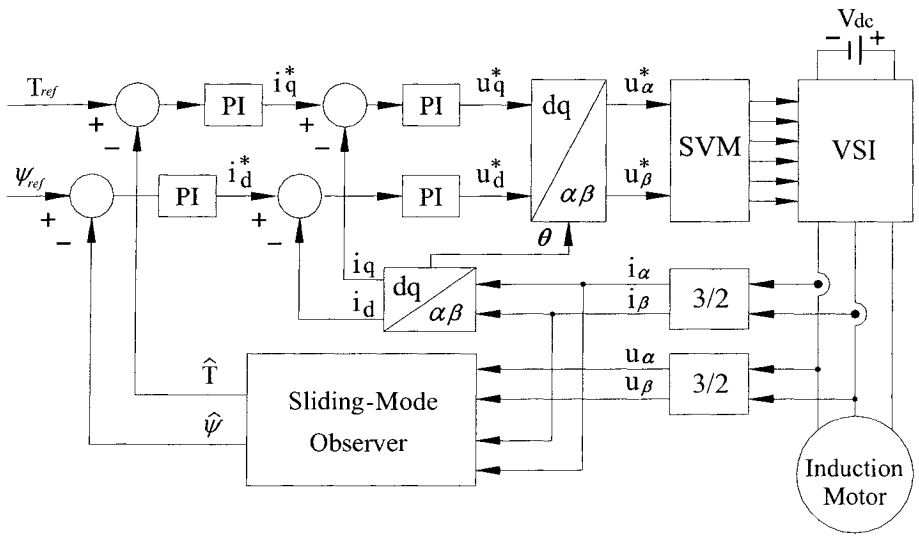

Figure 6.2: Classical PI control system

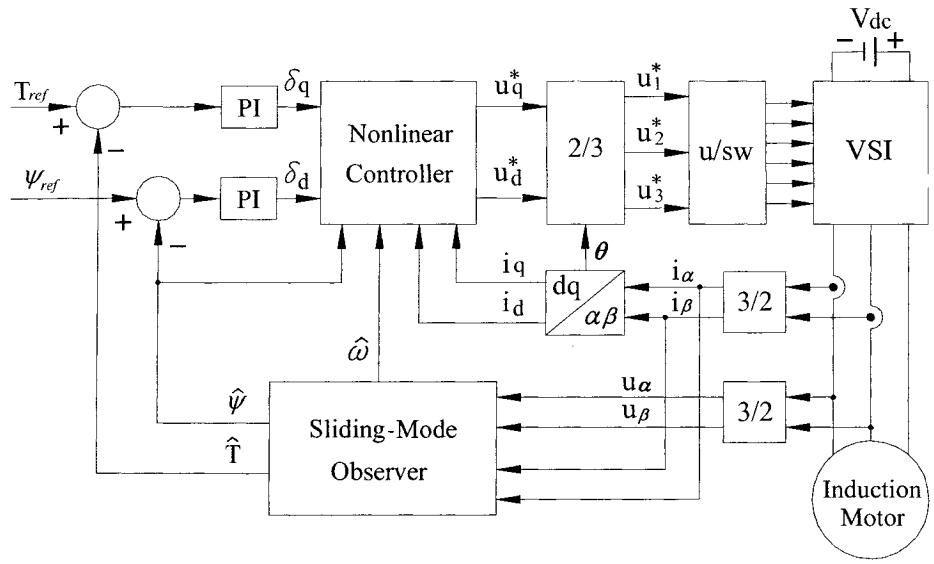

Figure 6.3: NSFC control system

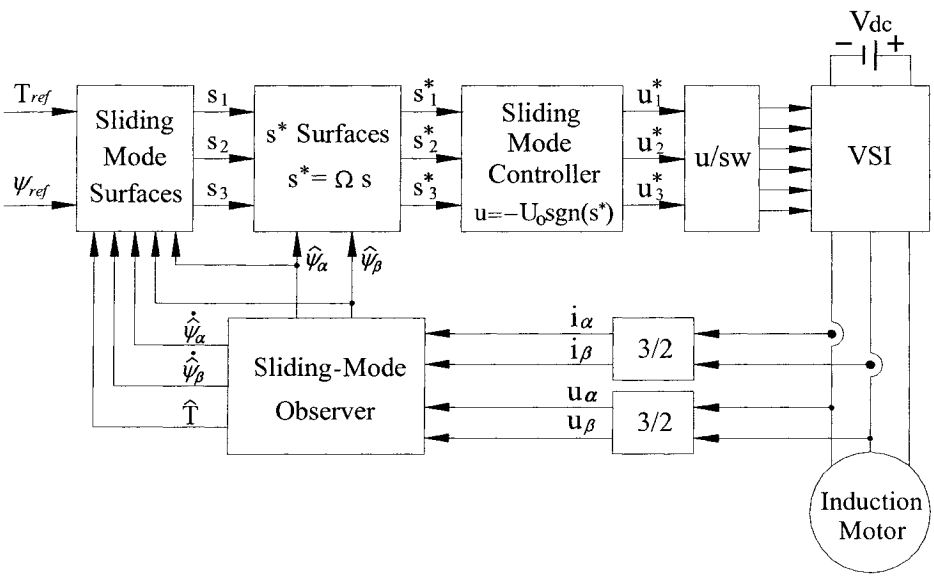

Figure 6.4: SMC control system

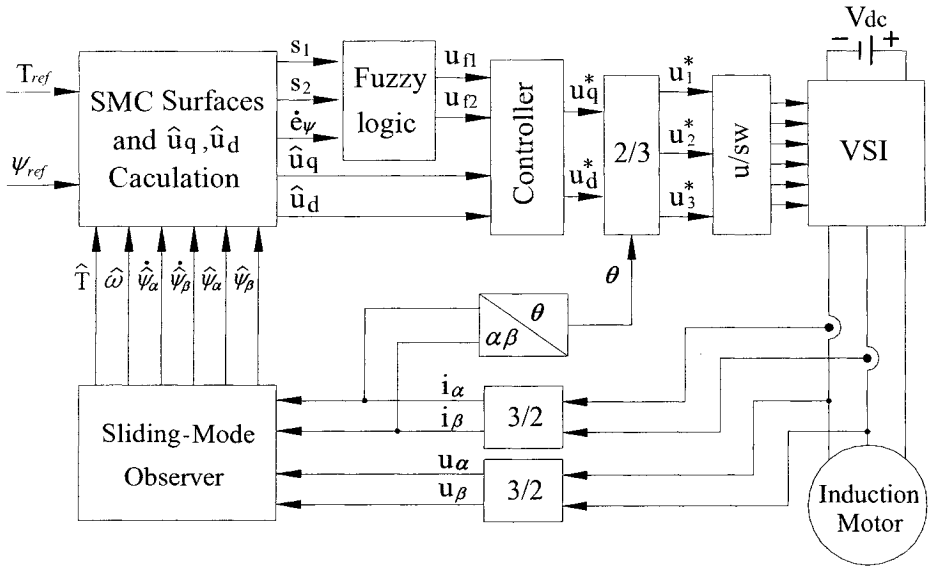

Figure 6.5: FSMC control system

The simulations are implemented by using MATLAB/SIMULINK. A 10-kHz fixed switching frequency for the inverter is used. For SMC with SVM, the constant K is given as K=400; parameters k_1 and k_2 are selected as k_1=0.1 and k_2=0.3. For the classical PI control system, the parameters of PI controllers are selected as k_{p1}= 4800, k_{i1}=800, k_{p2}=6e+6, k_{i2}=800, k_{p3}= 6000, k_{i3}=600, k_{p4}=3600 and k_{i4}=300. For the NSFC control system, the parameters of PI controllers are selected as k_{p1}= 2e+6, k_{i1}=5e+4, k_{p2}= 12e+6 and k_{i2}=5e+4. For the conventional SMC and FSMC control systems, the convergence factors are selected as c_2=400 and c_2=1600, respectively. For the sliding-mode observer used in all control systems, the constants are selected as $\omega_0 = 120$ and $\mu_0 = 200$; parameter C is chosen as C=*10*; the time constant of low-pass filter is selected as τ_f=0.0015. The nominal parameters of the induction motor listed in Table 3.1 are used in the following simulations.

6.1 Simulation results of stator current, rotor torque and rotor flux

Figures 6.6-6.11 show stator current i_α, rotor flux, torque and speed responses when the reference torque signal is a rectangular wave with frequency 2.5Hz.

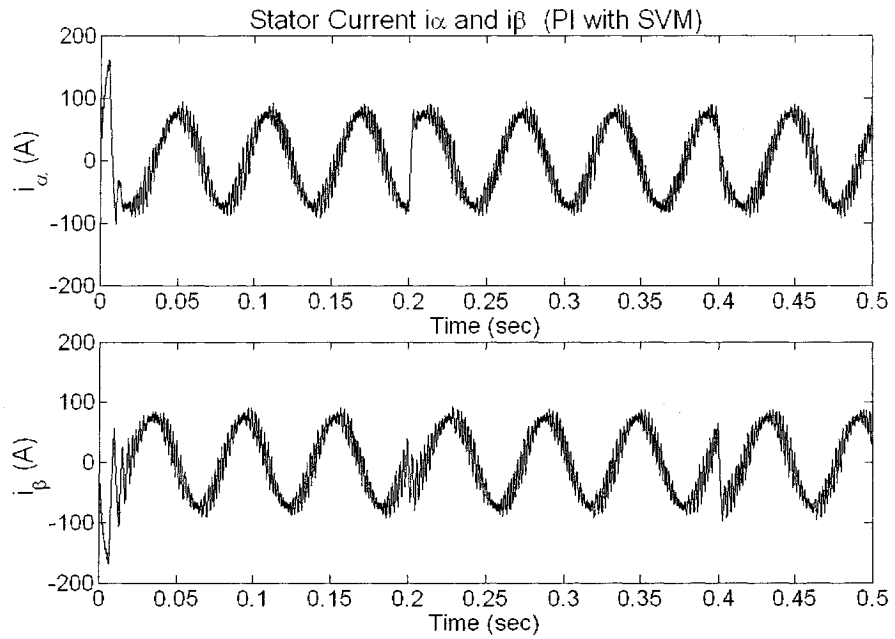

(a)

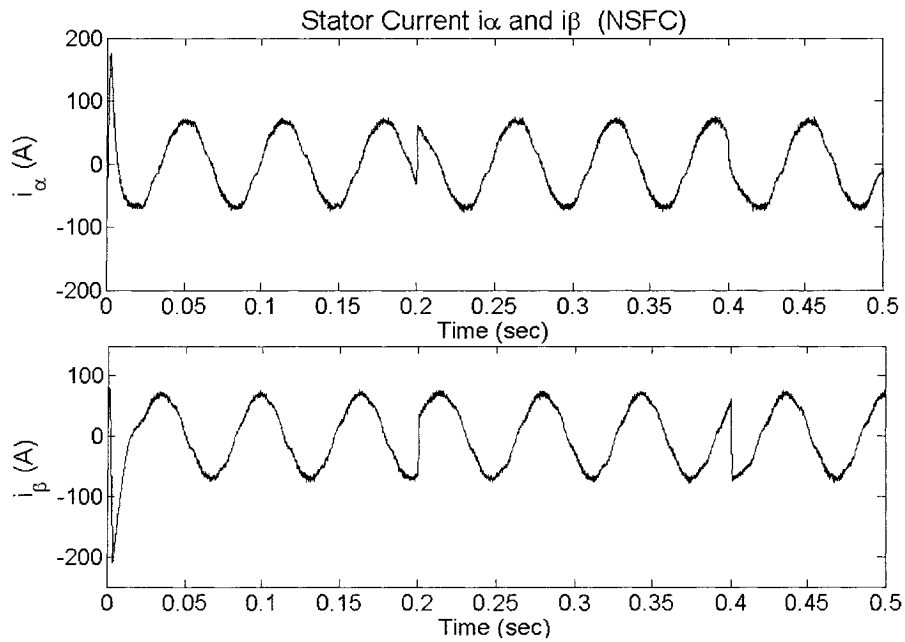

(b)

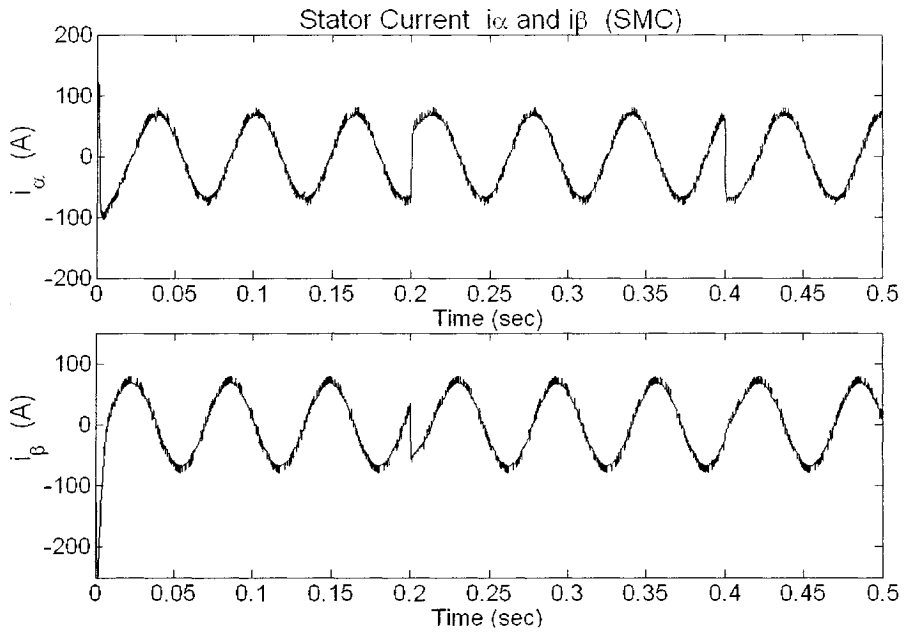
Stator Current iα and iβ (SMC)
200
100
0
-100
-200
i_α (A)
0 0.05 0.1 0.15 0.2 0.25 0.3 0.35 0.4 0.45 0.5
Time (sec)
100
0
-100
-200
i_β (A)
0 0.05 0.1 0.15 0.2 0.25 0.3 0.35 0.4 0.45 0.5
Time (sec)

(c)

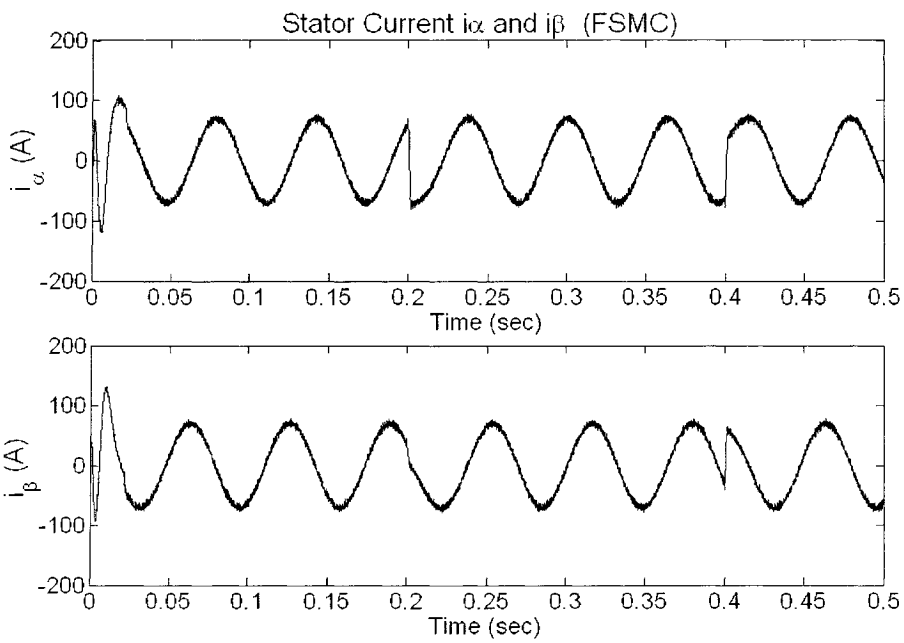
Stator Current iα and iβ (FSMC)
200
100
0
-100
-200
i_α (A)
0 0.05 0.1 0.15 0.2 0.25 0.3 0.35 0.4 0.45 0.5
Time (sec)
200
100
0
-100
-200
i_β (A)
0 0.05 0.1 0.15 0.2 0.25 0.3 0.35 0.4 0.45 0.5
Time (sec)

(d)

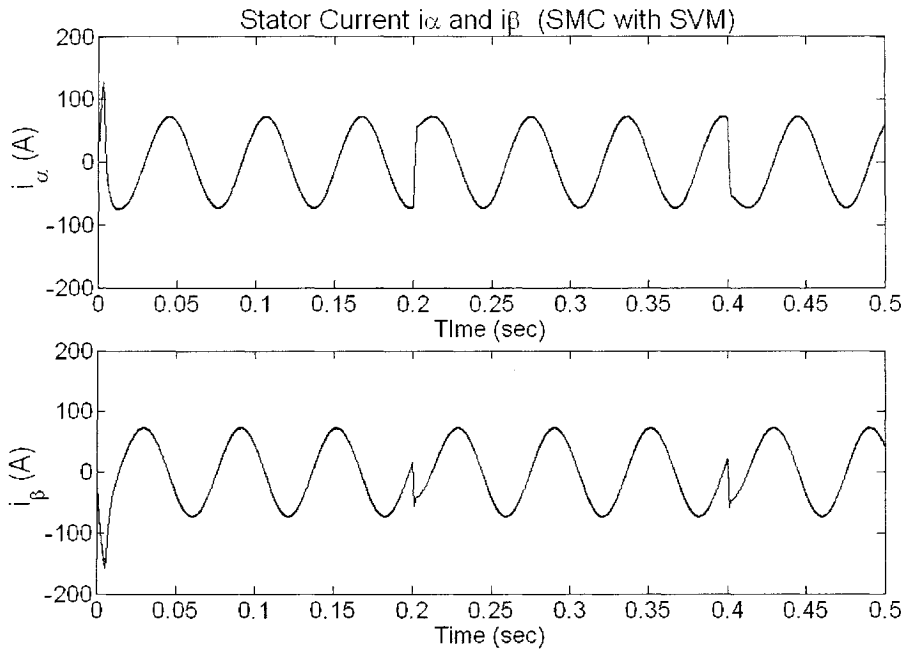

(e)

Figure 6.6: Stator current i_α and i_β (a) PI with SVM (b) NSFC (c) SMC (d) FSMC (e) SMC with SVM

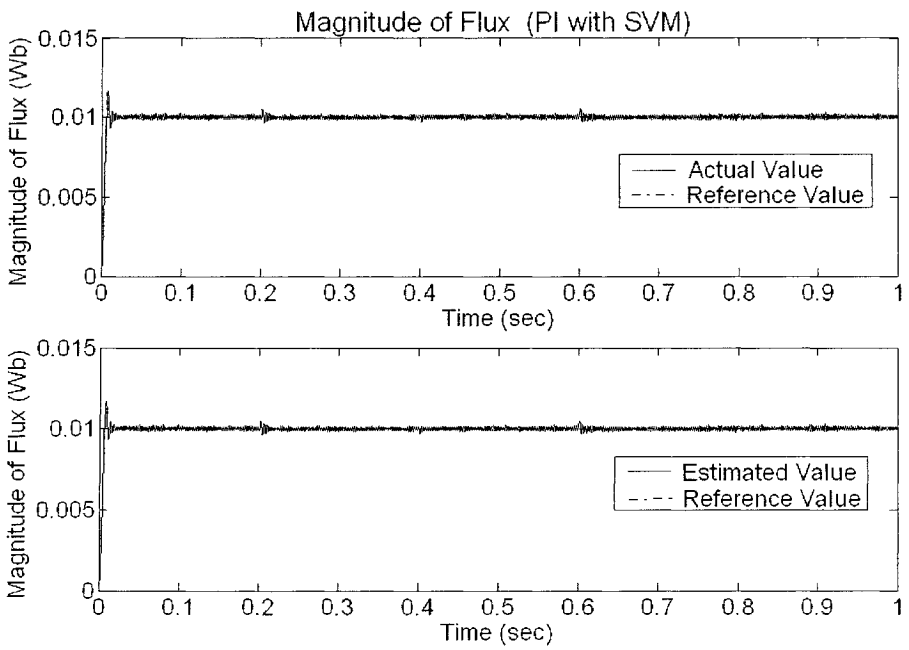

(a)

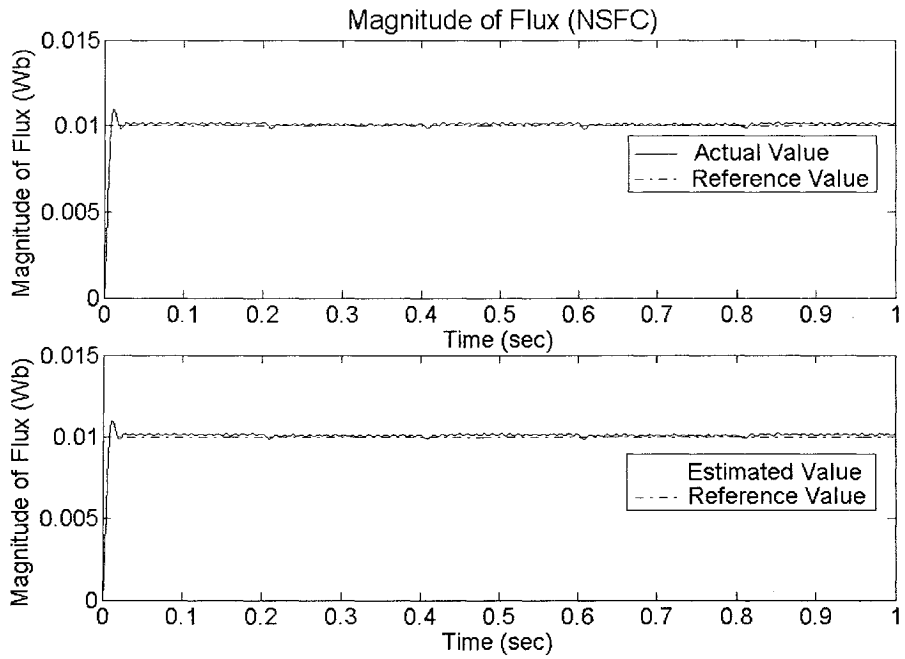
Magnitude of Flux (NSFC)
Magnitude of Flux (Wb)
0.015
0.01
0.005
0
Actual Value
Reference Value
0 0.1 0.2 0.3 0.4 0.5 0.6 0.7 0.8 0.9 1
Time (sec)
Magnitude of Flux (Wb)
0.015
0.01
0.005
0
Estimated Value
Reference Value
0 0.1 0.2 0.3 0.4 0.5 0.6 0.7 0.8 0.9 1
Time (sec)

(b)

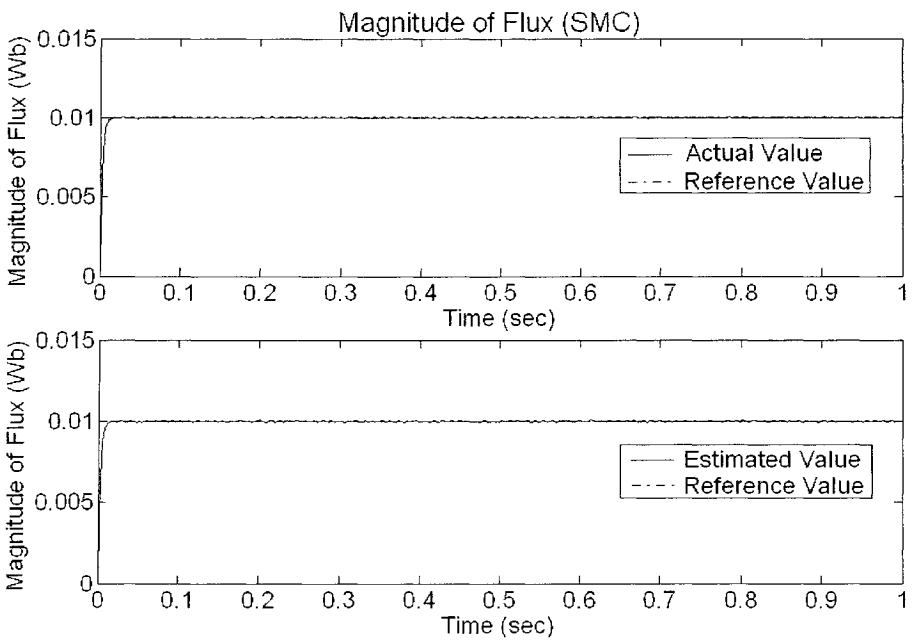
Magnitude of Flux (SMC)
Magnitude of Flux (Wb)
0.015
0.01
0.005
0
Actual Value
Reference Value
0 0.1 0.2 0.3 0.4 0.5 0.6 0.7 0.8 0.9 1
Time (sec)
Magnitude of Flux (Wb)
0.015
0.01
0.005
0
Estimated Value
Reference Value
0 0.1 0.2 0.3 0.4 0.5 0.6 0.7 0.8 0.9 1
Time (sec)

(c)

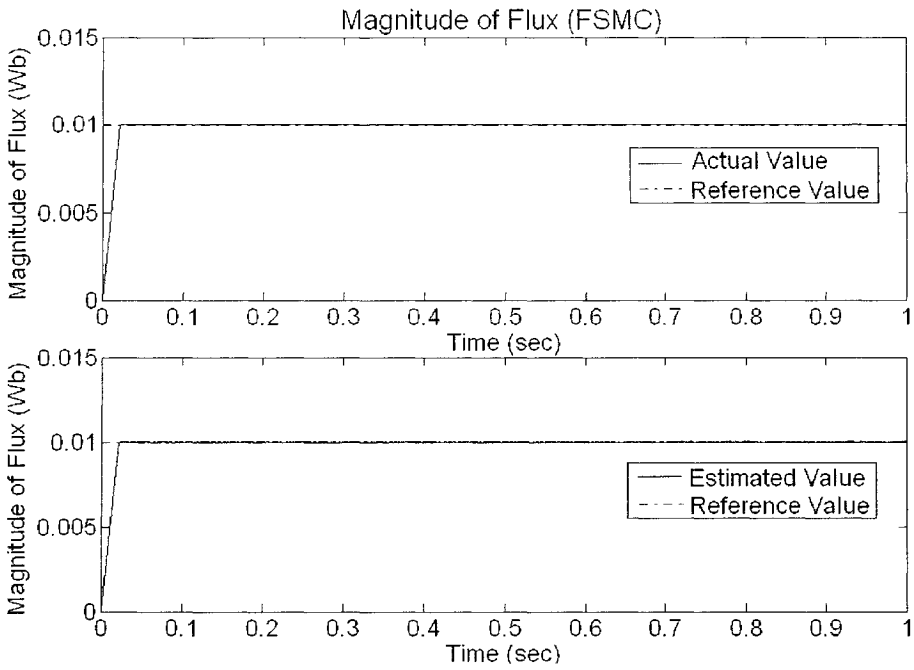

(d)

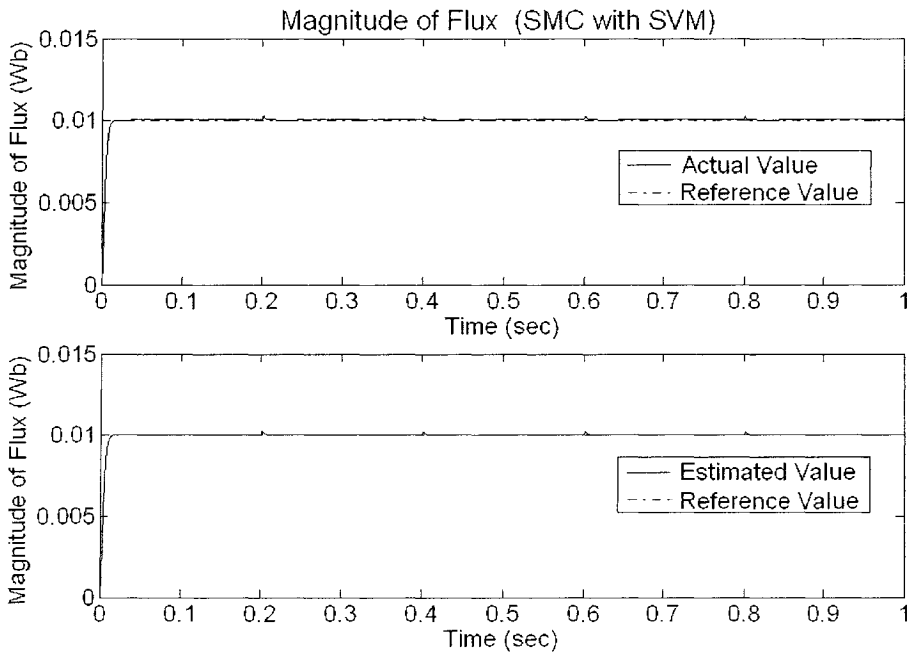

(e)

Figure 6.7: Rotor flux responses (a) PI with SVM (b) NSFC
(c) SMC (d) FSMC (e) SMC with SVM

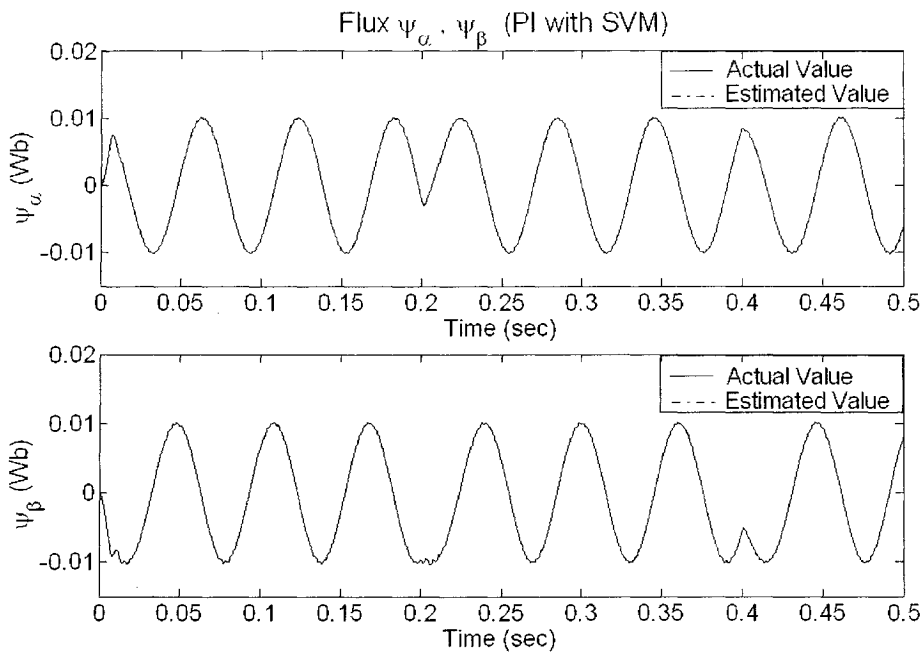
Flux ψ_α , ψ_β (PI with SVM)
Actual Value
Estimated Value
ψ_α (Wb)
ψ_β (Wb)
0.02
0.01
0
-0.01
0 0.05 0.1 0.15 0.2 0.25 0.3 0.35 0.4 0.45 0.5
Time (sec)

(a)

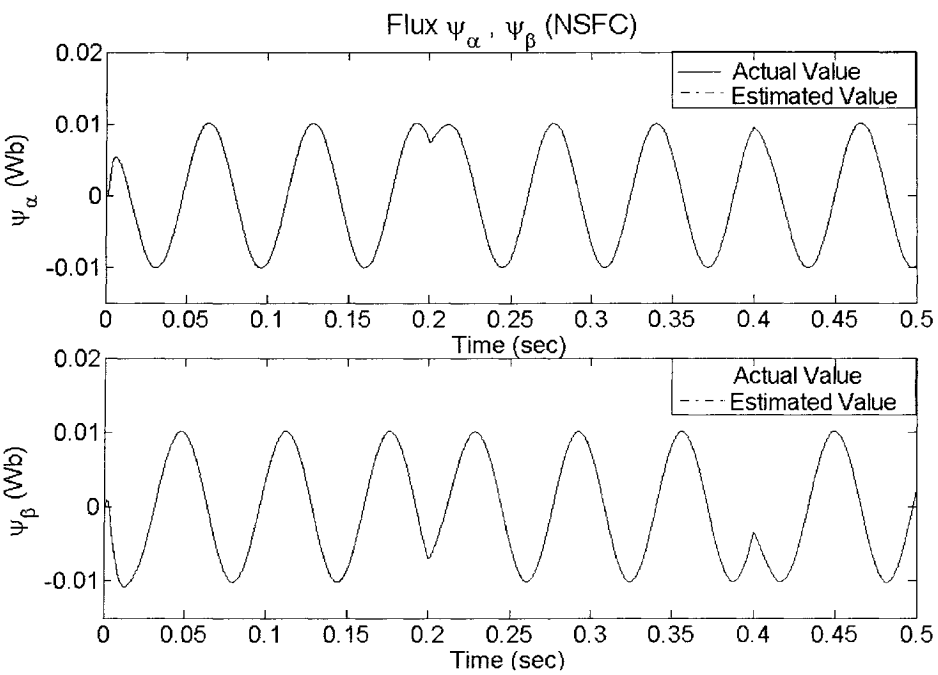
Flux ψ_α , ψ_β (NSFC)
Actual Value
Estimated Value
ψ_α (Wb)
ψ_β (Wb)
0.02
0.01
0
-0.01
0 0.05 0.1 0.15 0.2 0.25 0.3 0.35 0.4 0.45 0.5
Time (sec)

(b)

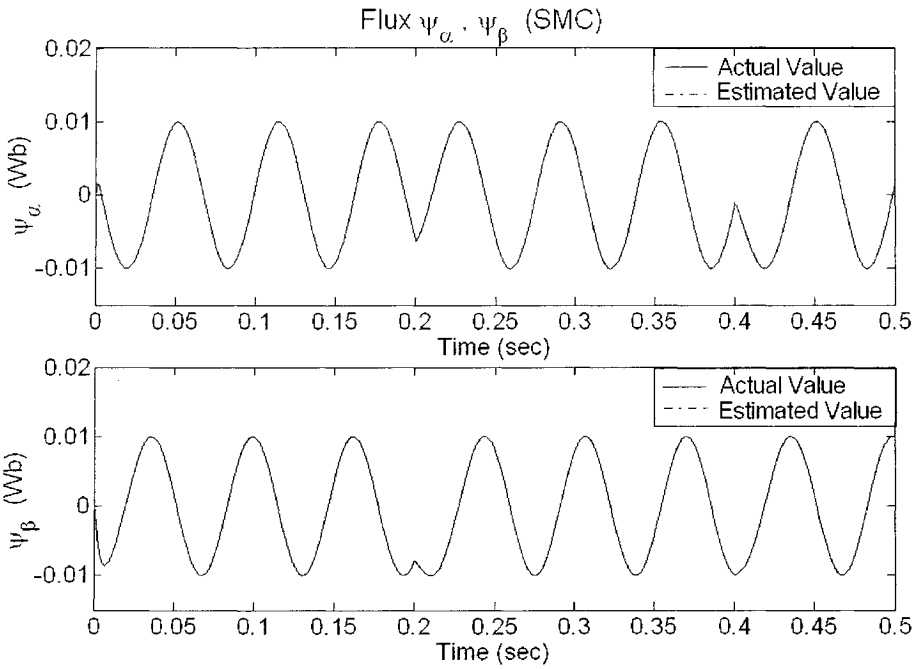
Flux ψ_α , ψ_β (SMC)
Actual Value
Estimated Value
ψ_α (Wb)
ψ_β (Wb)
0.02
0.01
0
-0.01
0 0.05 0.1 0.15 0.2 0.25 0.3 0.35 0.4 0.45 0.5
Time (sec)

(c)

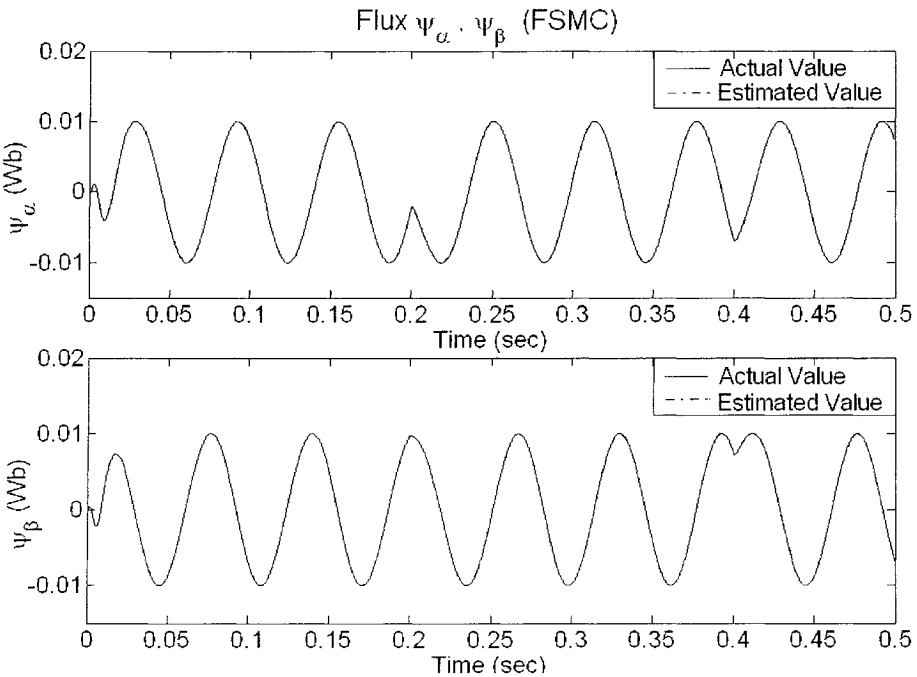
Flux ψ_α , ψ_β (FSMC)
Actual Value
Estimated Value
ψ_α (Wb)
ψ_β (Wb)
0.02
0.01
0
-0.01
0 0.05 0.1 0.15 0.2 0.25 0.3 0.35 0.4 0.45 0.5
Time (sec)

(d)

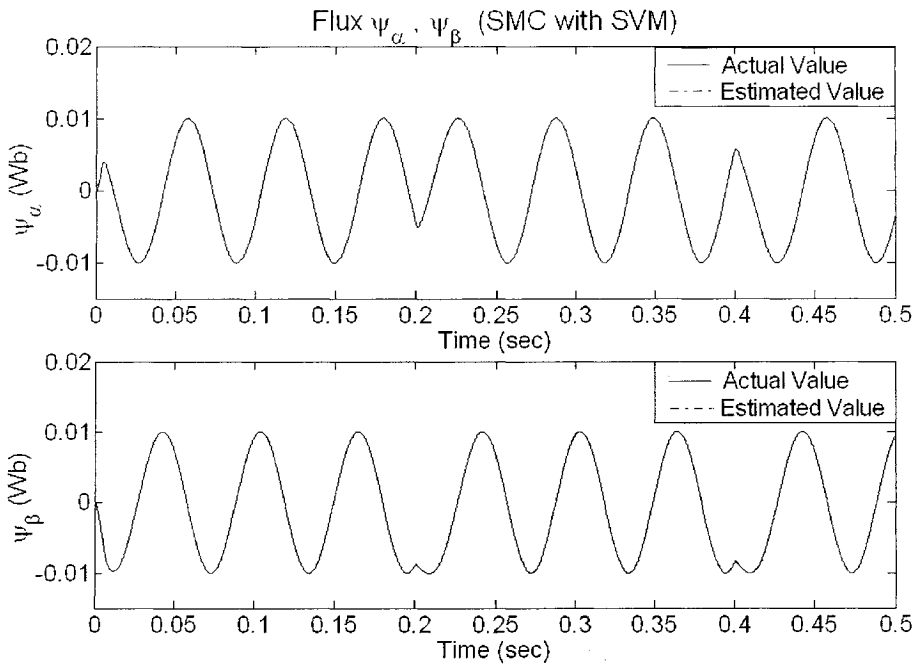

(e)

Figure 6.8: Rotor flux responses in (α, β) frame (a) PI with SVM (b) NSFC (c) SMC (d) FSMC (e) SMC with SVM

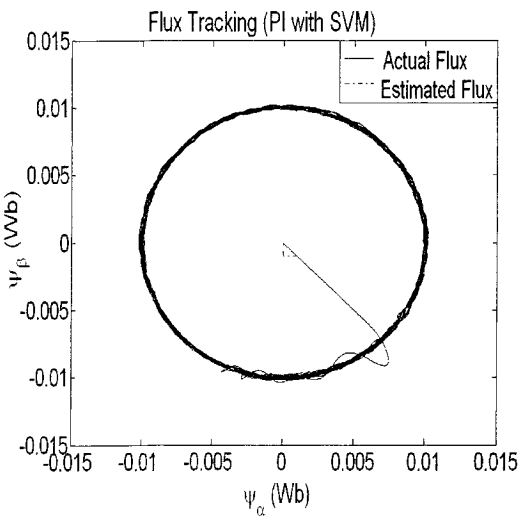

(a)

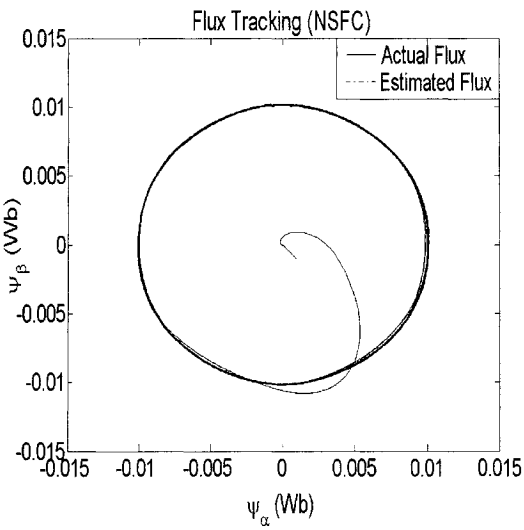

(b)

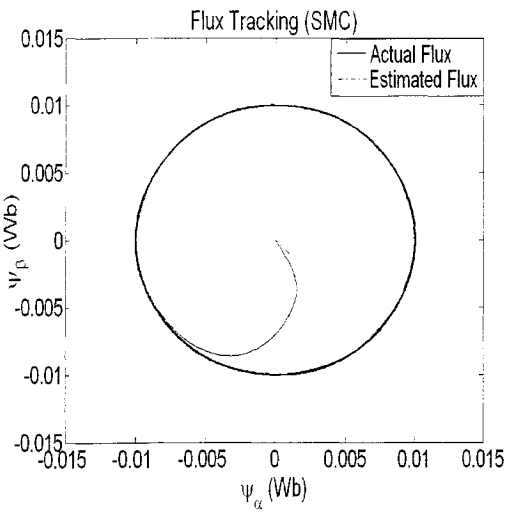

(c)

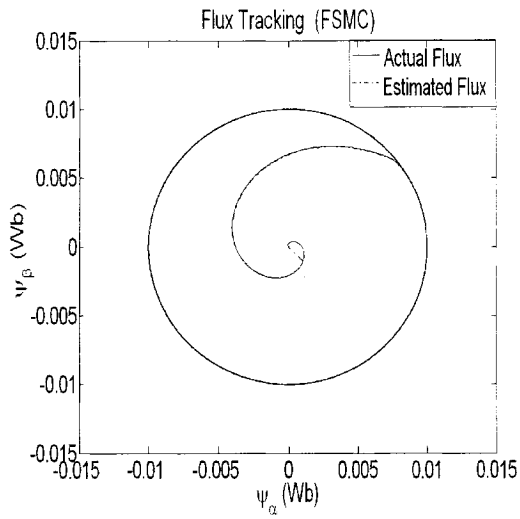

(d)

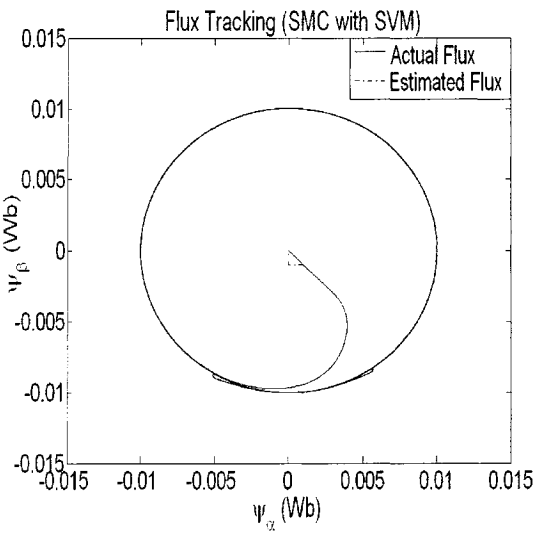

(e)

Figure 6.9: Rotor flux tracking (a) PI with SVM (b) NSFC
(c) SMC (d) FSMC (e) SMC with SVM

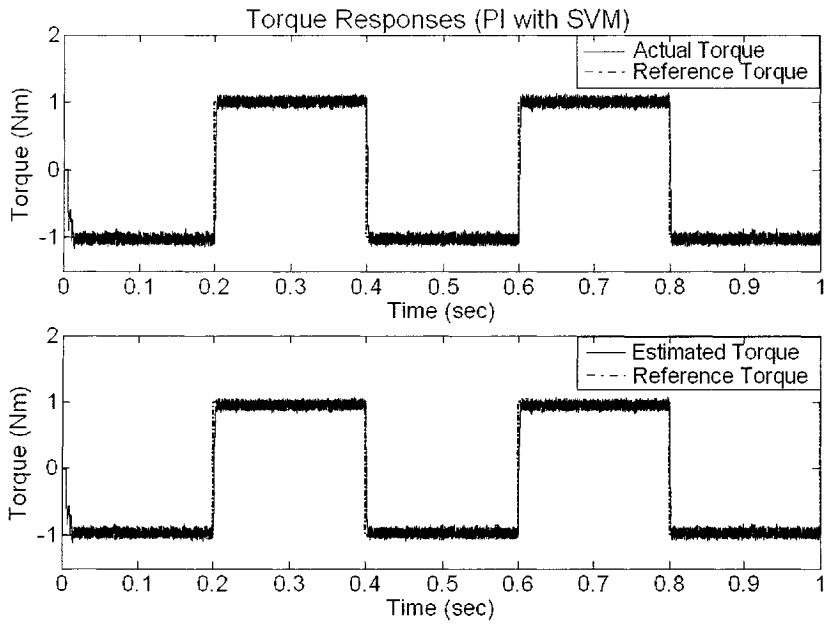
Torque Responses (PI with SVM)
Actual Torque
Reference Torque
Torque (Nm)
Time (sec)
Estimated Torque
Reference Torque
Torque (Nm)
Time (sec)

(a)

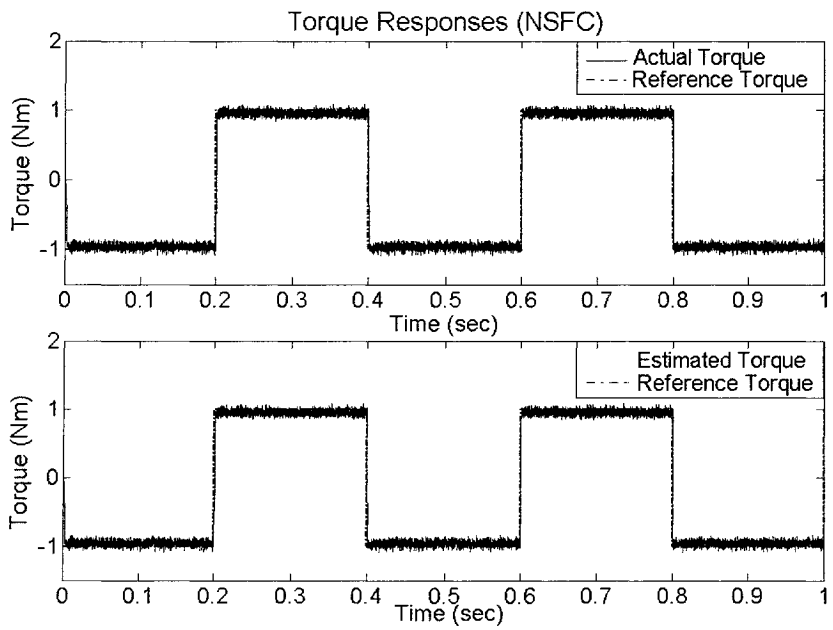
Torque Responses (NSFC)
Actual Torque
Reference Torque
Torque (Nm)
Time (sec)
Estimated Torque
Reference Torque
Torque (Nm)
Time (sec)

(b)

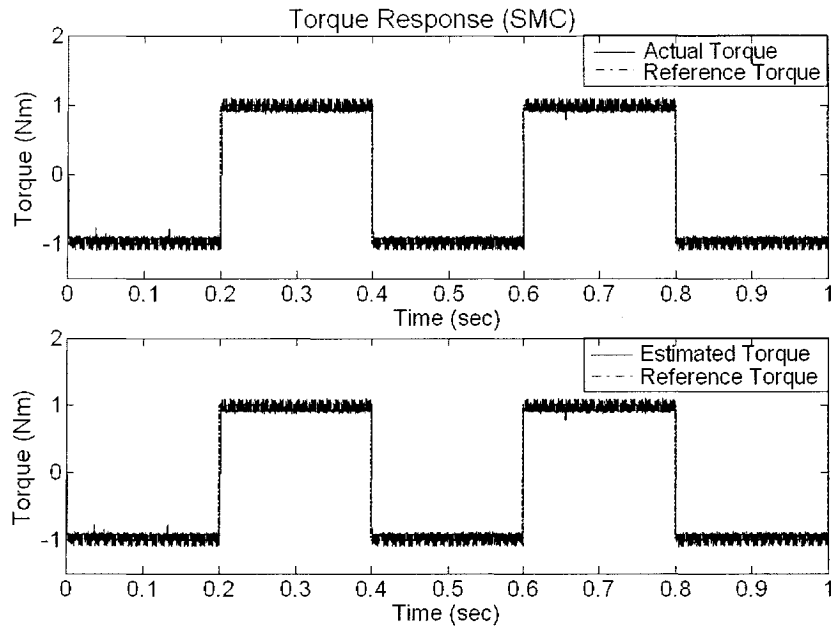
Torque Response (SMC)
Actual Torque
Reference Torque
Torque (Nm)
Time (sec)
Estimated Torque
Reference Torque
Torque (Nm)
Time (sec)

(c)

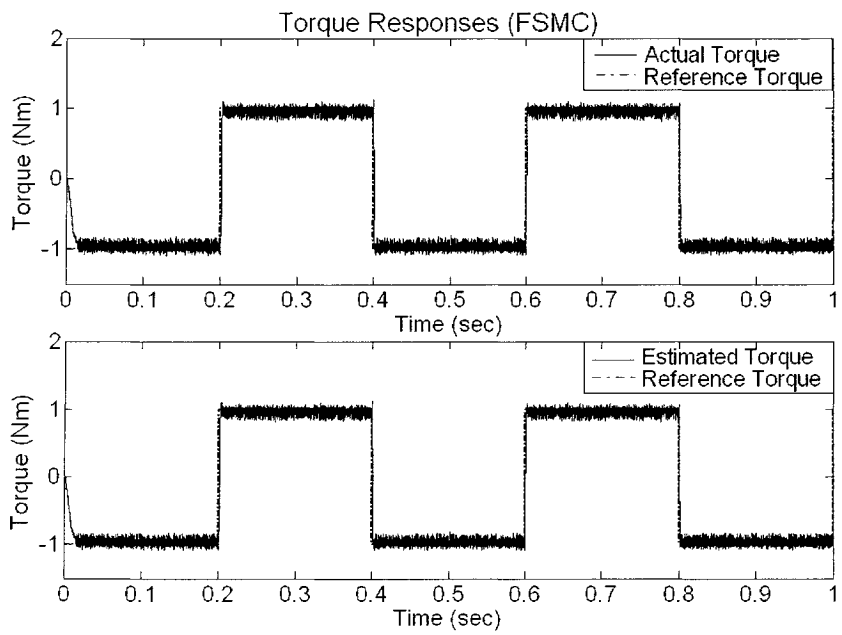
Torque Responses (FSMC)
Actual Torque
Reference Torque
Torque (Nm)
Time (sec)
Estimated Torque
Reference Torque
Torque (Nm)
Time (sec)

(d)

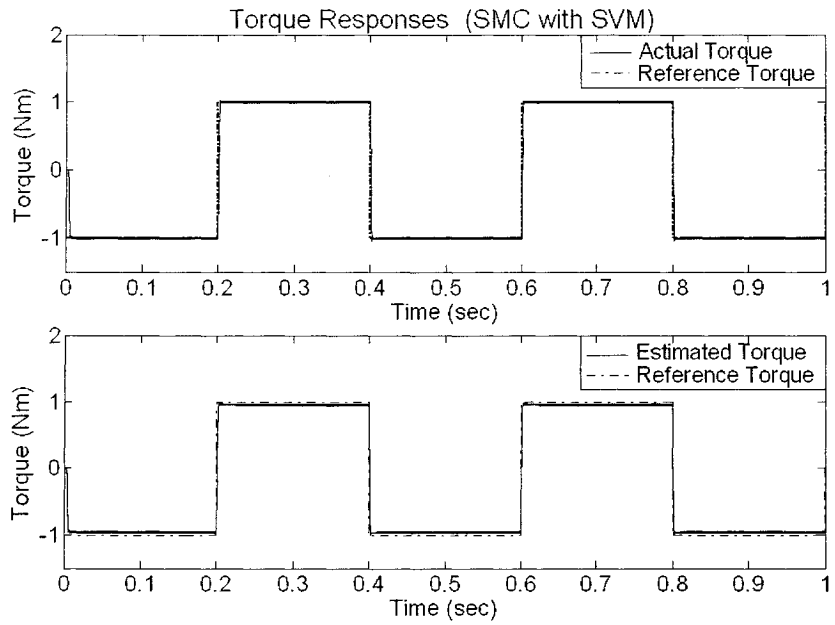

(e)

Figure 6.10: Torque responses (a) PI with SVM (b) NSFC (c) SMC (d) FSMC (e) SMC with SVM

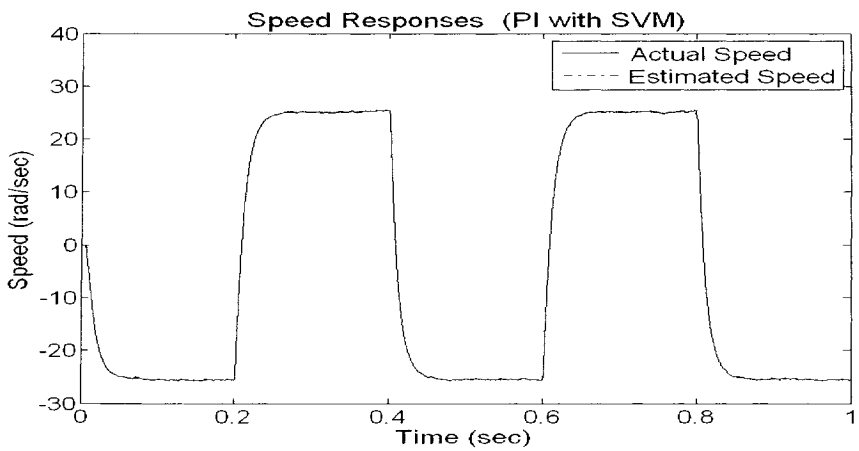

(a)

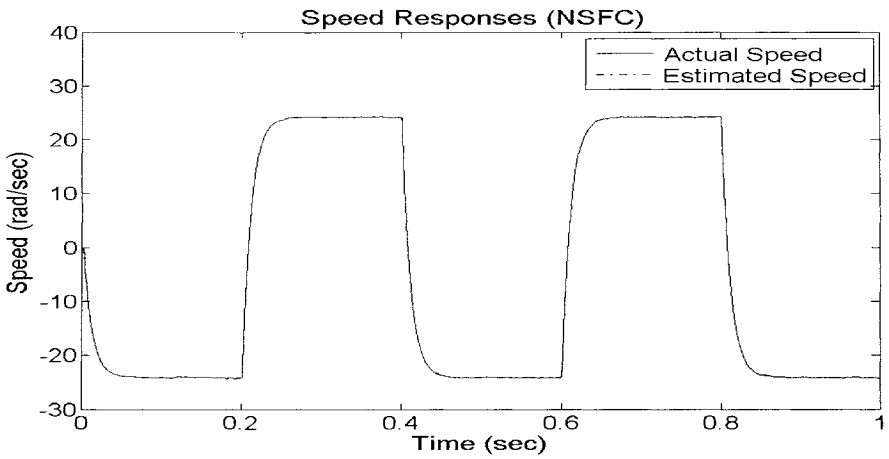
Speed Responses (NSFC)
Actual Speed
Estimated Speed
Speed (rad/sec)
Time (sec)
40
30
20
10
0
-10
-20
-30
0
0.2
0.4
0.6
0.8
1

(b)

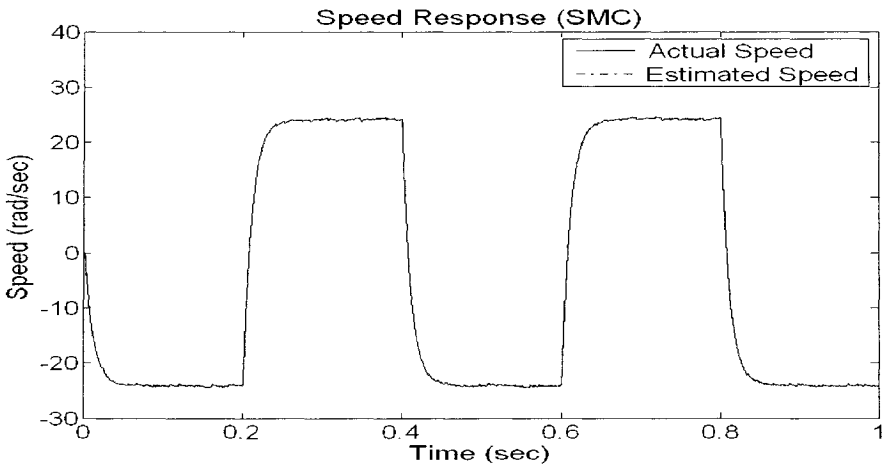
Speed Response (SMC)
Actual Speed
Estimated Speed
Speed (rad/sec)
Time (sec)
40
30
20
10
0
-10
-20
-30
0
0.2
0.4
0.6
0.8
1

(c)

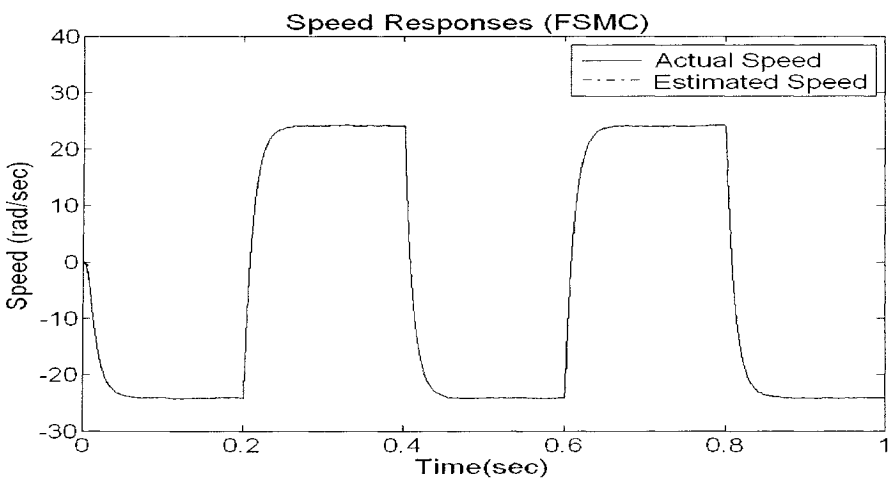
Speed Responses (FSMC)
Actual Speed
Estimated Speed
Speed (rad/sec)
Time(sec)
40
30
20
10
0
-10
-20
-30
0
0.2
0.4
0.6
0.8
1

(d)

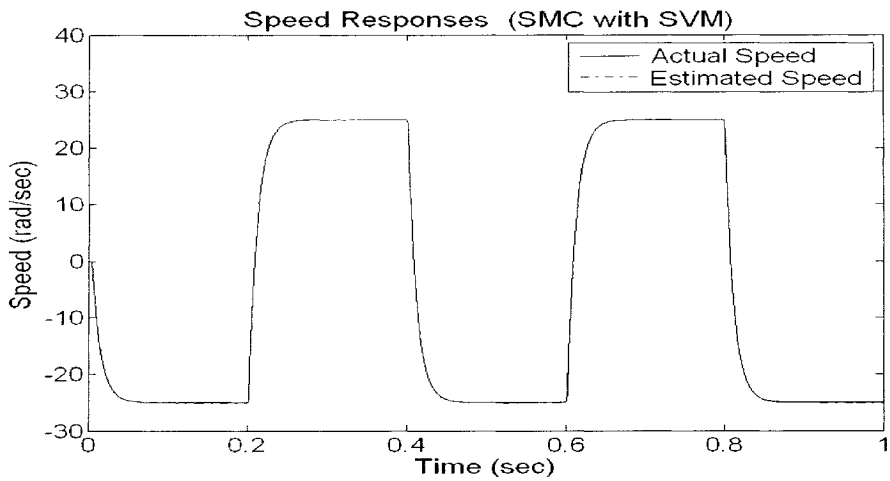

(e)

Figure 6.11: Speed responses (a) PI with SVM (b) NSFC
(c) SMC (d) FSMC (e) SMC with SVM

From Figure 6.6, it is noted that the resulting current has the largest harmonic distortion for PI with SVM, while the smallest harmonic distortion for SMC with SVM. Figures 6.7-6.9 show that the estimated rotor flux tracks the reference input or the actual value well in all five control methods, but PI with SVM control scheme has the most oscillation and biggest overshoot, while SMC with SVM has the least oscillation and no overshoot (Figure 6.7). Due to the large changed stator current, two disturbances appear at 0.2s and 0.4s in Figures 6.7a, 6.7b and 6.7e. However, no disturbances are found in Figure 6.7c and 6.7d. This demonstrates the fact of strong robustness of the conventional SMC system because of the usage of SMC in the observer, the controller, and even in the PWM. Also, this shows the disturbances rejection ability of a FSMC system. Although FSMC control system can reduce the current and flux ripple since the fuzzy control design relaxes the uncertainty bound of the SMC, it is difficult to reduce the torque ripple which mainly caused by the PWM logic control signals for the VSI.

Based on the simulation results shown in Figure 6.10, the output torque comparison of five control methods is shown as Table 6.1. The mean square error: $MSE = \frac{1}{m}\sum_{i=1}^{m}(x_i - R)^2$, where x_i is i^{th} value of a group of m values; R is reference value.

Table 6.1: Comparison of five control methods

Controllers	Mean Square Error of Output Torque	Torque Ripple
PI with SVM	0.64%	± 12%
NSFC	0.43%	+2% -13%
SMC	0.28%	± 8%
FSMC	0.69%	+5% -14%
SMC with SVM	0.004%	± 0.85%

Figure 6.10 and Table 6.1 show that, among five control methods, SMC with SVM has the best torque tracking performance with significant reduced torque ripple.

Figure 6.11 shows that the estimated speed tracks the actual speed very well in all five control methods. This proves the sliding-mode observer has good performance for speed estimation. The simulation results demonstrate that the proposed control approach can achieve the exact decoupling of torque and rotor flux, and owns satisfactory dynamic performance.

6.2 The comparison of logic signals for the inverter

The inverter's logic control signals of SMC and SMC with SVM control systems are shown in Figure 6.12.

Figure 6.12 shows that the proposed control system has regular logic signals for the inverter due to the proposed SVM technique while the SMC control system has irregular

logic signals because of the usage of direct sliding control signals as logic signals. This is the reason why the SMC with SVM control system has small torque ripple while the pure SMC control system has not.

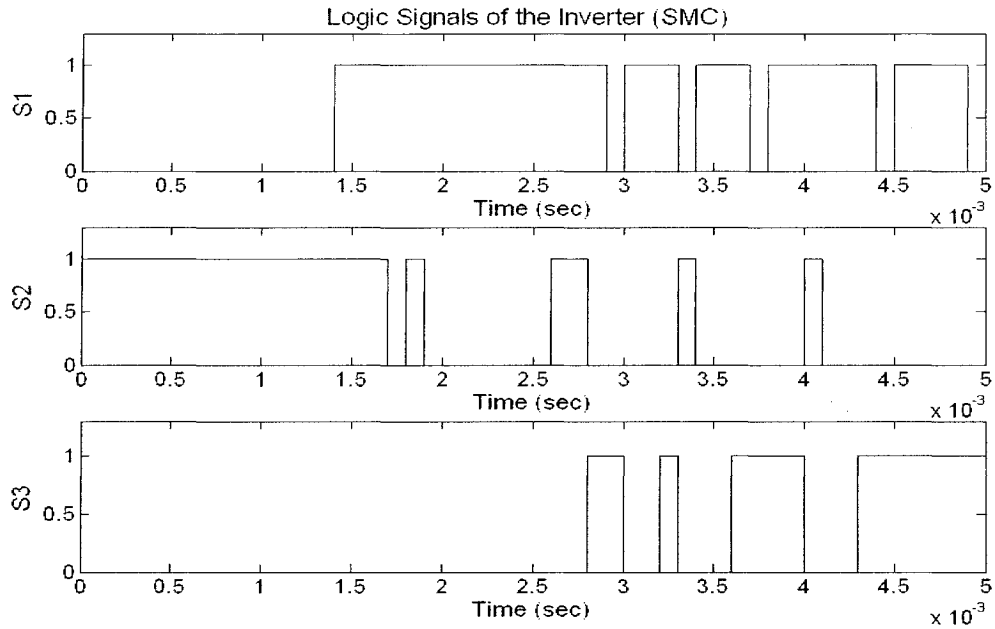

(a)

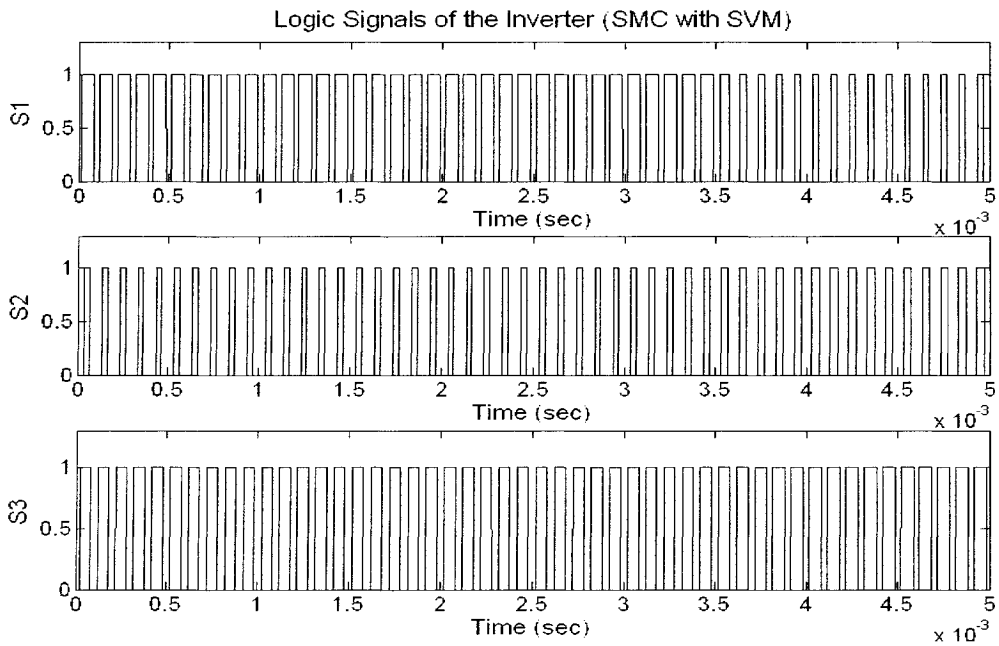

(b)

Figure 6.12: Logic signals of the inverter (a) SMC (b) SMC with SVM

6.3 Torque tracking

In order to test the torque tracking convergence to various reference torque signals, different kinds of waves are selected as the reference torque signals in simulations. Figures 6.13 - 6.14 show torque responses of five control methods when the reference torque signals are sine wave and piecewise wave, respectively.

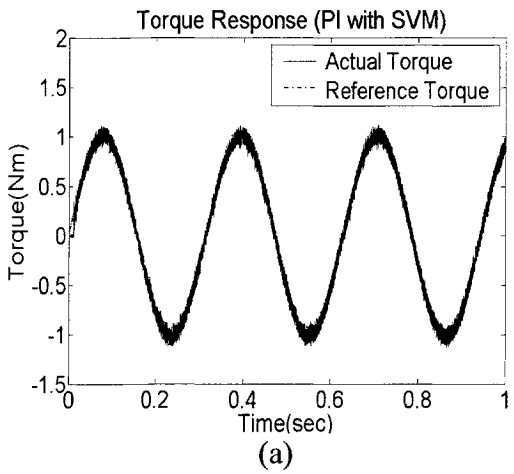

(a)

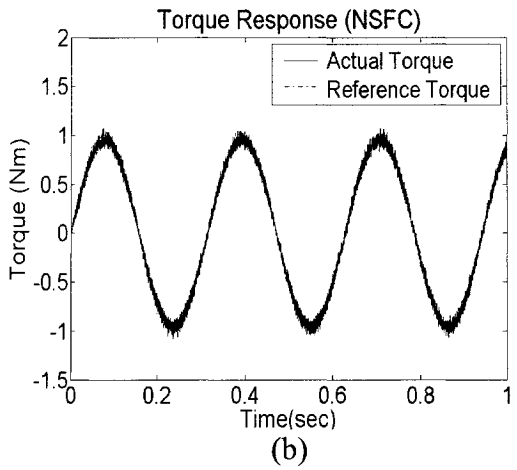

(b)

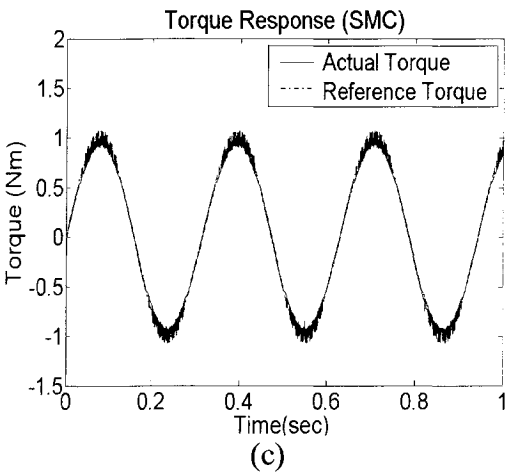

(c)

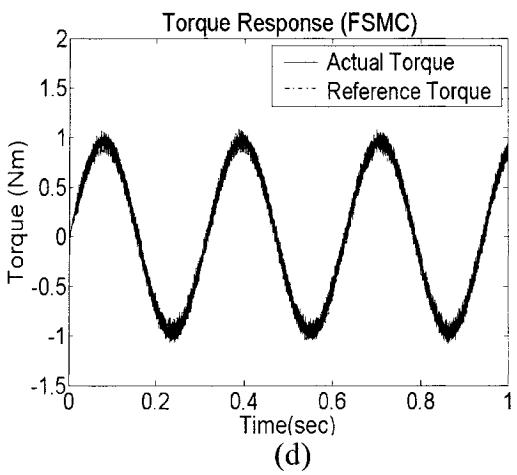

(d)

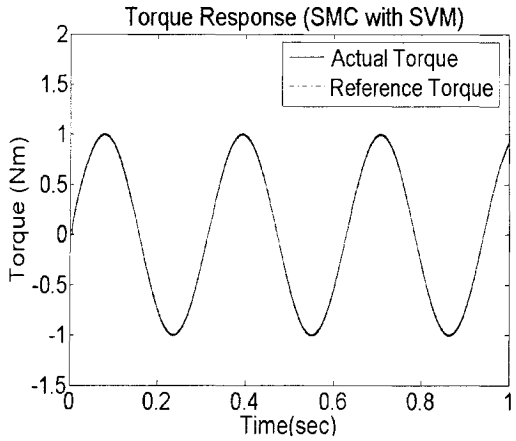

(e)

Figure 6.13: Torque responses with a sine wave reference signal (a) PI with SVM (b) NSFC (c) SMC (d) FSMC (e) SMC with SVM

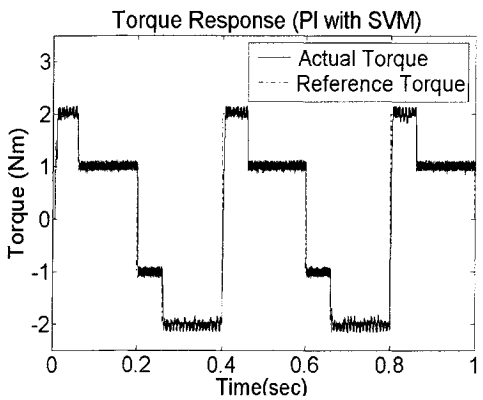

(a)

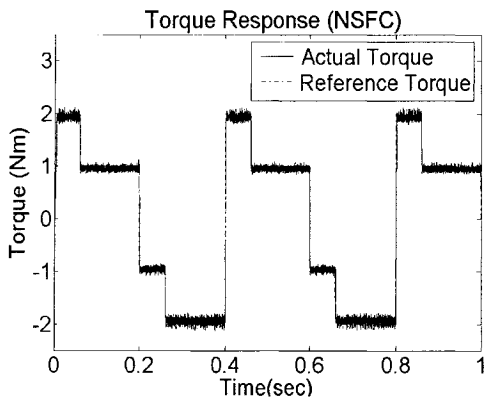

(b)

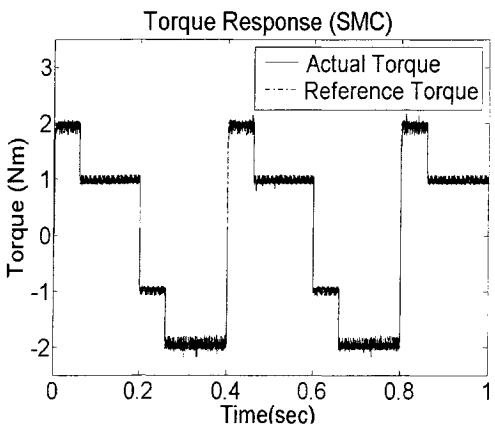

(c)

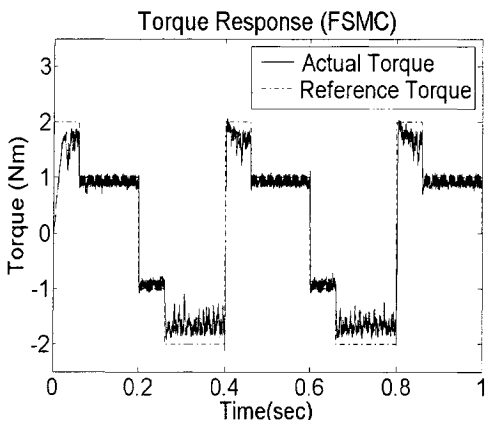

(d)

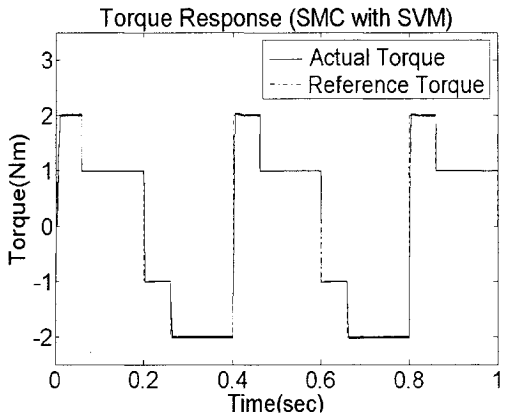

(e)

Figure 6.14: Torque responses with a piecewise wave reference signal (a) PI with SVM (b) NSFC (c) SMC (d) FSMC (e) SMC with SVM

From Figures 6.13 and 6.14, it is noted that the proposed new control method exhibits high accuracy in torque tracking when the reference torque signal is changed to different signals. PI with SVM, NSFC and SMC control systems also have good characteristic of torque tracking. However, Figure 6.14 shows that it is difficult for a FSMC control system to track a piecewise wave reference signal for torque control.

6.4 Load disturbances

To test the robustness of developed control method, the external load disturbance has been introduced to the proposed control system. Figure 6.15 shows torque and speed responses of five control methods when external load disturbance is white noise. Parameters of this white noise are: noise power [0.1]; sample time=0.0125; seed=[23321].

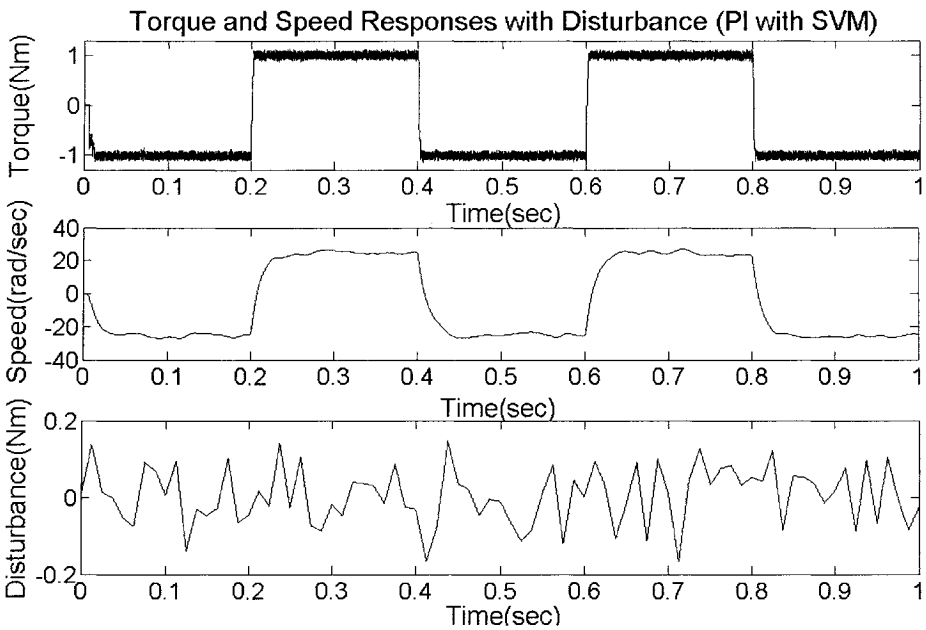
Torque and Speed Responses with Disturbance (PI with SVM)
Torque(Nm)
Speed(rad/sec)
Disturbance(Nm)
Time(sec)

(a)

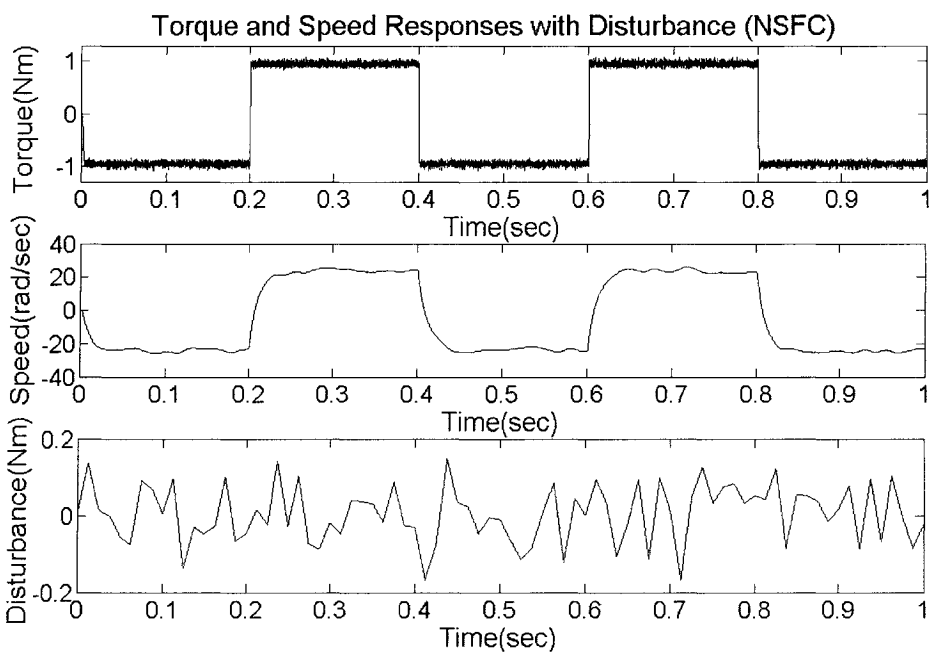
Torque and Speed Responses with Disturbance (NSFC)
Torque(Nm)
Speed(rad/sec)
Disturbance(Nm)
Time(sec)

(b)

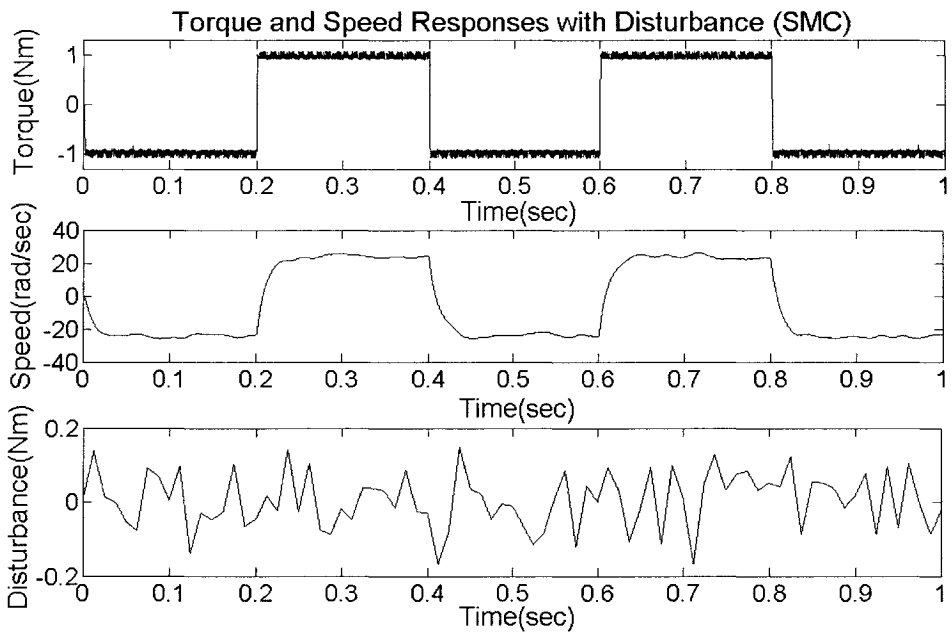
Torque and Speed Responses with Disturbance (SMC)
Torque(Nm)
Time(sec)
Speed(rad/sec)
Time(sec)
Disturbance(Nm)
Time(sec)

(c)

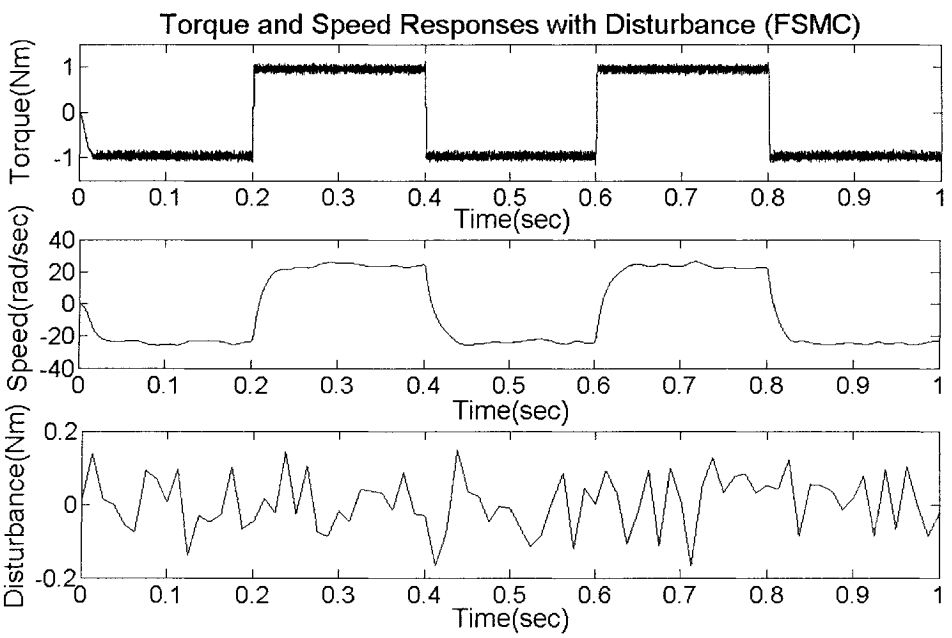
Torque and Speed Responses with Disturbance (FSMC)
Torque(Nm)
Time(sec)
Speed(rad/sec)
Time(sec)
Disturbance(Nm)
Time(sec)

(d)

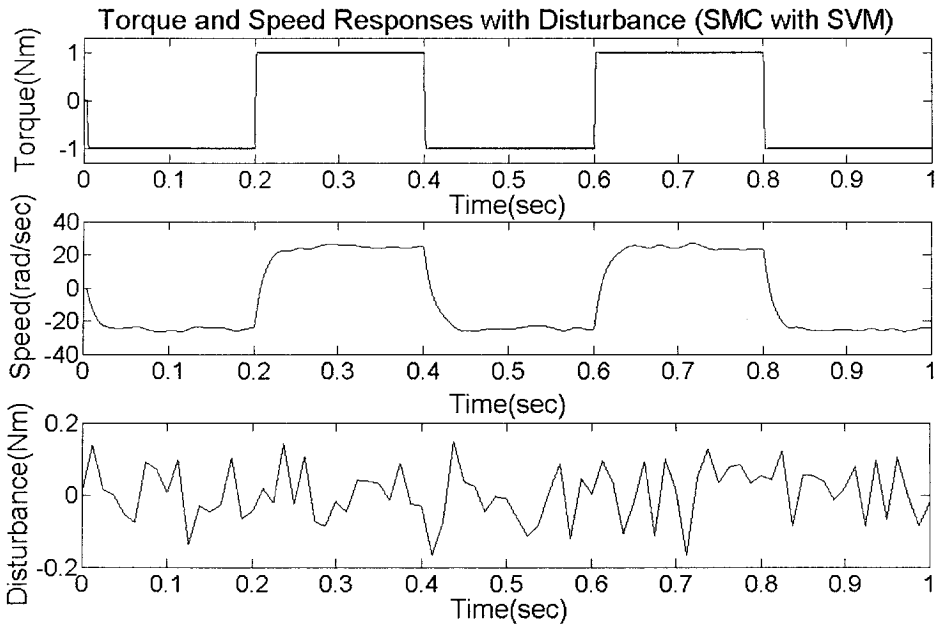

(e)

Figure 6.15: Torque and speed responses with disturbance (a) PI with SVM (b) NSFC (c) SMC (d) FSMC (e) SMC with SVM

From Figure 6.15, it is demonstrated that the torque response of the proposed new control system is insensitive to external load perturbation. Although the speed has small oscillation because of the disturbance, the new control system is stable and robust.

6.5 Summary

Simulation results show that the proposed control scheme provides high-performance dynamic characteristics with small current, flux and torque ripple. This scheme provides high accuracy in torque tracking to various reference torque signals and strong robustness to external load disturbances.

The tested performances of the induction motor control system are important for HEV applications. Unlike the traditional industrial setting, in which the induction motor

operates mostly at steady state, the HEV applications require high performance control of electric motors to obtain fast transient responses and energy efficiency. Important characteristics of a HEV motor include good drive control and fault tolerance, as well as low noise with high efficiency. When a series/parallel HEV is accelerated from start or low to mid-range speeds, it runs entirely on power generated by the motor. During sudden acceleration, extra power is immediately supplied from the battery to the electric motor to drive the vehicle at a high speed. Therefore, the torque tracking characteristics of the induction motor control system can ensure to provide a good response and smooth drive, as well as to improve acceleration performance of the vehicle. Small current and flux ripple mean low motor noise and high motor efficiency. Small torque ripple and the load disturbance rejection ability can provide good driving control and fault tolerance, and thus give more comfortable ride.

Chapter 7
Conclusions and Recommendations for Future Work

7.1 Conclusions

In this thesis, a novel speed-sensorless torque control of an induction motor for HEVs has been presented and extensively tested by simulation. This new control system can achieve the complete decoupled control of torque and flux and significant torque ripple reduction. Compared with the classical FOC, conventional SMC, and FSMC control methods, it has low torque ripple, low current distortion and high-performance dynamic characteristics. Moreover, this new control scheme can also achieve fast and accurate torque tracking to various reference torque signals and own very strong robustness to external load disturbances. The proposed novel induction motor control method is simple, accurate and robust, and meets the requirement of HEV applications. The important results of this research work are summarized as follows.

1) A chattering-free sliding-mode observer has been implemented. The analysis and simulation results show the sliding-mode observer owns strong robustness and accurate estimation performance over the full speed range. A boundary layer around the switching surface is introduced to reduce the chattering of the observer. The benefits of the boundary layer approach are that sliding-mode design methodologies can be exploited to derive a continuous control and the invariance property of sliding-mode control is

preserved at same times. Although the flux/speed observer is of the fourth order, the error equations of the sliding-mode observer are reduced to the second order after sliding mode arises on the surfaces. The order reduction is one of the important properties of the sliding modes.

2) The SVM technique has been implemented in this new control system for the VSI control. The objective of SVM techniques is to approximate the output voltage vector by a combination of the eight switching patterns. It simplifies the digital implementation of PWM modulations. The analysis and simulation results show the SVM technique is more preferable scheme to the PWM voltage source inverter since it gives a large linear control range, less harmonic distortion and fast transient response. The test results also show that even though the pole voltage of the inverter includes the harmonic component, it doesn't appear in the phase voltage of the motor. Since the phase voltage of the motor is equal to the difference of the pole voltage of the inverter and the neutral point potential of the motor, which contains exactly all the third harmonic components of the pole voltage, the third harmonics are removed from the phase voltage. The SIMULINK blocks and the M-file S-function methods have been developed to implement the SVM. An M-file S-function representation displays faster execution time than the same system built using SIMULINK blocks, while the SIMULINK blocks have clear structure.

3) A new sliding-mode controller is implemented. This controller has been proved to be robust and provide high accurate torque tracking. A control law has been chosen to meet the requirement of the SVM technique for the inverter. The control law is the combination of a discontinuous function and a continuous function. The continuous

function can improve the performance of the SVM while the discontinuous function is used to ensure robustness of the control system. With this control law, the complete decoupled control of torque and flux has been obtained.

7.2 Recommendations for future work

1) Experimental test of new control system

The experimental setup has been established. A DMC1500 digital control board [70] and eZdsp^{TM}F2812 DSP board [71] have been used in this experimental setup. A test of open loop system has been done. The test results have shown the hardware setup worked well (See Appendix A). However, due to the time and experimental equipments limitation, and Lab unavailability because of moving, the new control system has not been tested. The following points about the experiment are recommended for future works.

- The parameters of motor, such as rotor resistance, stator inductance, rotor inductance and mutual inductance, are basic information for the observer of a speed-sensorless control of the induction motor. However, the motor used in this experiment is old type one, and the information about parameters are missing. So a new induction motor with reference parameters supplied by the manufacturer is needed for future works.

- The isolated transformer used in current experimental setup is a 120/37V transformer. It can only be used to test the hardware setup. A 120/120V isolated transformer is necessary.

- A XDS510 emulator developed by Texas Instruments, Inc. (TI) is necessary for future works. The XDS510 emulator is tightly integrated with the Code Composer Studio™ (CCS) debugger interface, making all of TI's real time emulation control and visualization capabilities available to the developer. These range from single-stepping and register visibility to software and hardware breakpoints, and cycle-accurate benchmarking. All of these are supported without requiring a debug monitor.

The figures of the currently established experimental setup are shown in Figure 7.1 and Figure 7.2.

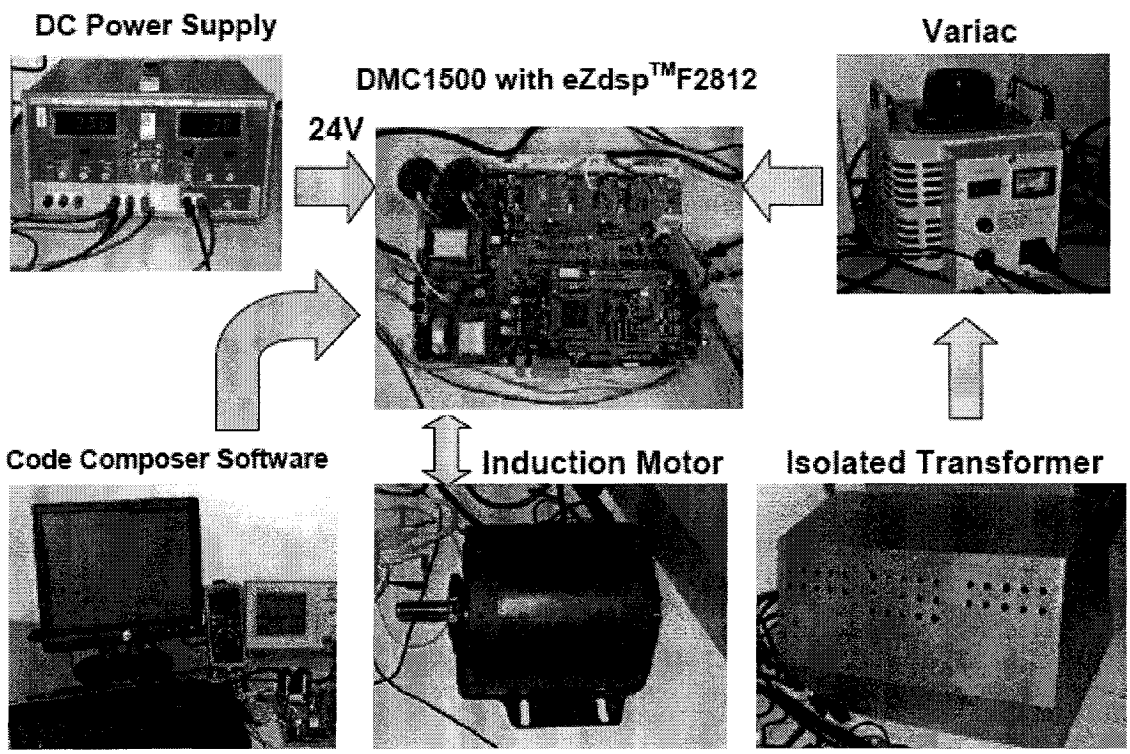

Figure 7.1: Components of experimental setup

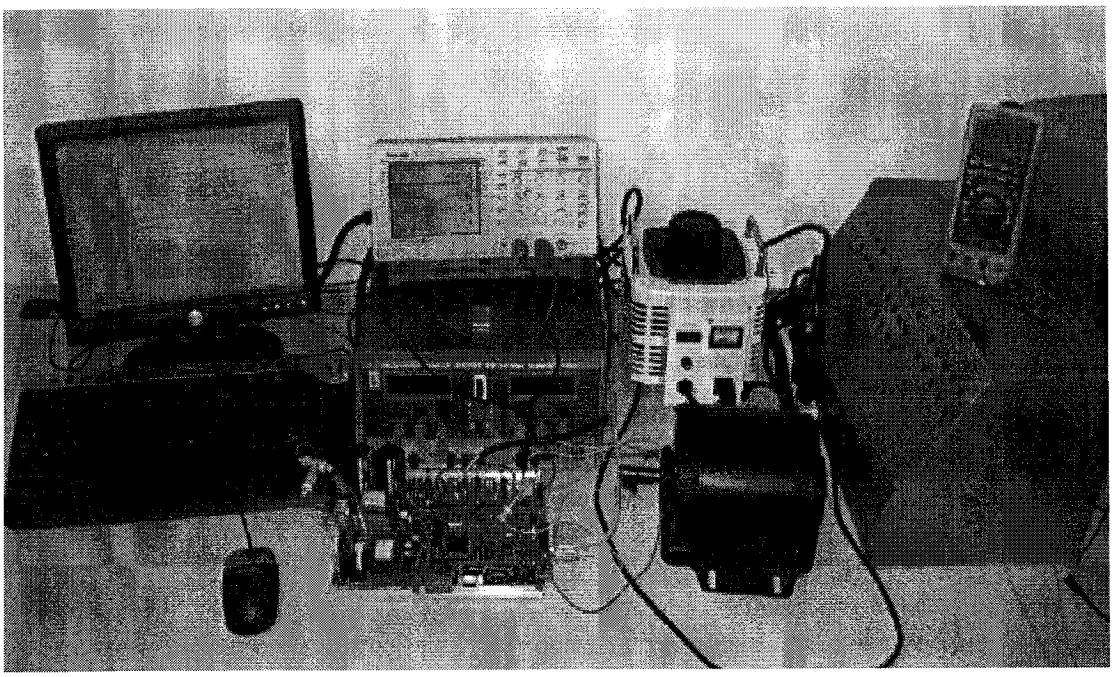

Figure 7.2: Experimental setup

2) The parameters identification of induction motors.

Speed-sensorless control techniques require the knowledge of the motor parameters. Although the new control method is strongly robust, due to the unmeasurable rotor parameters and the parameters variation with the operating conditions, the big mismatch in parameters may occur. A big mismatch in parameters will lead to control errors. Therefore, an adaptive online parameters estimator may reduce the control errors, and enhance the accuracy of the control system.

References

[1] Husain, I., *Electric and Hybrid Vehicles Design Fundamentals*. CRC Press, 2003.

[2] Won, J.S. and Langari, R., "Intelligent energy management agent for a parallel hybrid vehicle", IEEE Proceedings of the American Control Conference Denver, Colorado, pp. 2560-2565, Jun. 4-6, 2003.

[3] Leblanc, N., Kern, J., Duoba, M., Bohn, T. and Larsen, R., "Analysis of performance results from future truck 2001", SAE Technique Paper Series, 2002-01-1209, 2002.

[4] Rajagopalan, A. and Washington, G., "Intelligent control of hybrid electric vehicles using GPS information", SAE Technique Paper Series, 2002-01-1936, 2002.

[5] Schouten, N. J., Salman, M. A., and Kheir, N. A., "Fuzzy logic control for parallel hybrid vehicles", IEEE Trans. on Control Systems Technology, Vol.10, No.3, May 2002.

[6] Glenn, B., Washington, G. and Rizzoni, G., "Operation and control strategies for hybrid electric automobiles", SAE Technique Paper Series, 2000-01-1537, 2000.

[7] Brown, P., Jackson, N., Sykes, L., Wheals, J. and Wiseman, M., "A hybrid and fuel cell vehicle future", SAE Technique Paper Series, 2002-01-1908, 2002.

[8] Kim, J., Jung, J. and Nam, K., "Dual-inverter control strategy for high-speed operation of EV induction motors", IEEE Trans. Ind. Electron., Vol. 51, pp. 312-320, Apr. 2004.

[9] Rahman, Z., Butler, K. L. and Ehsani, M., "A comparison study between two parallel hybrid control concepts", SAE Technical Paper Series, 2000-01-0994, 2000.

[10] Powell, B. K., Bailey, K. E. and Cikanek, S. R., "Dynamic modeling and control of hybrid electric vehicle powertrain systems", IEEE Control Systems, pp. 17-33, Oct. 1998.

[11] Gregory A. H. and Kamal, Y. T., "Modeling and simulation of a hybrid-electric vehicle drivetrain", Proceedings of the American Control Conference, pp. 636-640, Jun. 1997.

[12] Proca, A. B., "Induction motor control for hybrid electric vehicle applications", OHIO State Univ. PHD thesis, ISBN 0-493-34200-1, 2001.

[13] Jefferson, C. M. and Barnard, R. H., *Hybrid Vehicle Propulsion*. WIT Press, 2002.

[14] Braham, A., Guezennec, Y., and Rizzoni, G., "Optimal energy management in series hybrid electric vehicles", Proceedings of the American Control Conference, Chicago, Illinois, Jun. 2000.

[15] Coffey, R. A. and Sorenson, S. C., "A comparison of new technology vehicle airborne emissions and energy usage", Int. J. Environmental Technology and Management, Vol.1, No.1/2, 2001.

[16] Johnson, V. H., Wipke, K. B. and Rausen, D. J., "HEV control strategy for real-time optimization of fuel economy and emissions", SAE Technical Paper Series, 2001-01-1543, 2000.

[17] http://www.ott.doe.gov/hev/.

[18] http://www.toyota.co.jp/en/tech/environment/ths2/.

[19] Lin, C. C. *et al.*, "Integrated, feed-forward hybrid electric vehicle simulation in SIMULINK and its use for power management studies", SAE technical paper series, 2001-01-1334, 2001.

[20] http://www.fordvehicles.com/suvs/escapehybrid/.

[21] http://www.toyota.com/vehicles/2005/prius/.

[22] http://automobiles.honda.com/models/specifications_full_specs.asp/.

[23] http://worldwide.hyundai-motor.com/.

[24] http://www.cip.csiro.au/Machines/.

[25] Tursini, M., Petrella, R. and Parasiliti, F., "Adaptive sliding-mode observer for speed-sensorless control of induction motors", IEEE Trans. Ind. Appl., Vol. 36, pp. 1380-1387, 2000.

[26] Benchaib, A., Rachid, A. and Audrezet, E., "Sliding mode input-output linearization and field orientation for real-time control of induction motors", IEEE Trans. Power Electron., Vol. 14, pp. 3-13, 1999.

[27] Chen, F. and Dunnigan, M.W., "Sliding-mode torque and flux control of an induction machine", *IEE Proc.-Electr. Power Appl.*, Vol. 150, pp. 227-236, Mar. 2003.

[28] Barrero, F., Gonzalez, A., Torralba, A., Galvan, E. and Franquelo, L. G., "Speed control of induction motors using a novel fuzzy sliding-mode structure", *IEEE Trans. Fuzzy Sys.*, Vol. 10, pp. 375-383, Jun. 2002.

[29] Depenbrock, M., "Direct self control for high dynamics performance of inverter feed AC machines", ETZArchiv, Vol. 7, No. 7, pp. 211-218, 1985.

[30] Takahashi, I. Noguchi, T., "A new quick response and high efficiency strategy of an induction motor", Conf. Rec. IEEE-IAS Annual Meeting, pp. 495-502, 1985.

[31] Utkin, V. I., *Sliding Modes in Control and Optimization*. Springer-Verlag, Berlin, Germany, 1992.

[32] Utkin, V. I., "Sliding mode control design principles and applications to electric drives", IEEE Trans. Ind. Electron., Vol. 40, pp. 23-36, Feb. 1993.

[33] Shieh, H. J. and Shyu, K. K., "Nonlinear sliding-mode torque control with adaptive backstepping approach for induction motor drive", IEEE Trans. Ind. Electron., Vol. 46, pp. 380-389, 1999.

[34] Kaletsanos, A., Xepapas, S. Hl. and Manias, S. N., "A novel sliding mode fuzzy logic control technique for induction motor drive systems", IEEE 0-7803-7067-8/01, 2001.

[35] Soto, R. and Yeung, K. S., "Sliding-mode control of induction motor without flux measurement", IEEE Trans. Ind. Appl., Vol. 31, pp. 744-750, 1995.

[36] Yan, Z., Jin, C. X. and Utkin, V. I., "Sensorless sliding-mode control of induction motors", IEEE Trans. Ind. Electron., Vol. 47, pp. 1286-1297, 2000.

[37] Benchaib, A., Rachid, A. and Audrezet, E., "Real-time sliding-mode observer and control of an induction motor", IEEE Trans. Ind. Electron., Vol. 46, pp. 128-137, 1999.

[38] Kang, J. K. and Sul, S. K., "New direct torque control of induction motor for minimum torque ripple and constant switching frequency", IEEE Trans. Ind. Applicat., Vol. 35, pp. 1076-1082, 1999.

[39] Lascu, C. and Trzynadlowski, A. M., "Combining the principles of sliding mode, direct torque control, and space-vector modulation in a high-performance sensorless AC drive", IEEE Trans. Ind. Appl., Vol. 40, pp.170-176, 2004.

[40] Vas, P., *Sensorless Vector and Direct Torque Control*. Oxford Univ. Press, Oxford, UK, 1998.

[41] Atkinson, D.J., Acarnley, P. P., and Finch, J. W., "Observer for induction motor state parameter estimation", IEEE Trans. Ind. Appl., Vol. 27, pp.1119-1127, 1991.

[42] Schroedl, M., "Sensorless control of AC machines at low speed and standstill based on the 'INFORM' method", Proc. IEEE-IAS Annual meeting, Vol.1, pp.270-277, 1996.

[43] Jansen, P.L., and Lorentz, R.D., "Transducer-less position and velocity estimation in induction and salient AC machines", IEEE Trans. Ind. Appl., Vol. 31, pp. 240-247, 1995.

[44] Schauder, C., "Adaptive speed identification for vector control without rotational transducers", IEEE Trans. Ind. Appl., Vol. 28, 1992.

[45] Peng, F. Z., and Fukao, T., "Robust speed identification for speed-sensorless vector contro of induction motors", IEEE Trans. Ind. Appl., Vol. 30, 1994.

[46] Maes, J., and Melkebeek, J. A., "Speed-sensorless direct torque control of induction motor using an adaptive flux observer", IEEE Tran. Ind. Appl., Vol. 36, 2000.

[47] Kubota, H., and Matsuse, K., "Speed-sensorless field-oriented control of induction motor with rotor resistance adaptation", IEEE Trans. Ind. Appl., Vol. 30, 1994.

[48] Hennenberg, G., Brunsbach, B. J., and Klepsch, T., "Field oriented control of synchronous and asynchronous drives without mechanical sensors using Kalman filter", Proc. European Conf. on Power electronics and applications (EPE), Florence, Italy, Vol. 3, pp. 664-671, 1991.

[49] Kim, R., Sul, S. K., and Park, M. H., "Speed sensorless vector control of induction motor using extended Kalman filter", IEEE Trans. Ind. Appl., Vol. 30, pp.1225-1233, 1994.

[50] Kim, H. W. and Sul, S. K., "A new motor speed estimator using Kalman filter in low-speed range", IEEE Trans. Ind. Electron., Vol. 43, pp. 498-504, Aug. 1996.

[51] Hurst, K. D., and Habetler, T. G., " Sensorless speed measurement using current harmonic spectral estimation in induction machines drives", IEEE Trans. Power Electron., Vol. 11, 1996.

[52] Vas, P., *Artificial-intelligence-based Electrical Machines and Drives Application of Fuzzy, Neural, Fuzzy-neural and Genetic-algorithm-based Techniques*. Oxford Univ. Press, Oxford, UK, 1999.

[53] Lin, F. J., Wai, R. J., and Lin, P. C., "Robust speed sensorless induction motor drive", IEEE Trans. Aero. and Electron. Syst., Vol. 35, pp. 566-578, Apr. 1999.

[54] Houldsworth, J. A and Grant, D. A., "The use of harmonic distortion to increase the output voltage of a three-phase PWM inverter", IEEE Trans. Ind. Appl., Vol. 20, pp. 1224-1228, Sept/Oct. 1984.

[55] Holtz, J., "Pulsewidth modulation for electronic power conversion", Proc. IEEE, Vol. 82, pp. 1194-1214, Aug. 1994.

[56] Agelidis, V. G., Ziogas, P. D. and Joos, G., "Dead-band PWM switching patterns", IEEE Trans. Power Electron., Vol. 11, pp. 523-531, July 1996.

[57] Trznadlowski, A. and Legowski, S., "Minimum-loss vector PWM strategy for three-phase inverter", IEEE Trans. Power Electron., Vol. 9, pp. 26-34, Jan. 1994.

[58] Ziogas, P. D., Moran, L., Joos, G. and Vincenti, D., "A refined PWM scheme for voltage and current source converter", Proc. IEEE PESC'90, pp. 977-983, 1990.

[59] Zhou, K. and Wang, D., "Relationship between space-vector modulation and three-phase carrier-based PWM: a comprehensive analysis", IEEE Trans. Ind. Electron., Vol. 49, pp. 186-195, 2002.

[60] Bose, B. K., *Power Electronic and Variable Frequency Drives: Technology and Applications*. IEEE Press, New York, 1996.

[61] Holtz, J., "Sensorless control of induction motor drives", Proc. IEEE Vol. 90, pp. 1359-1394, Aug. 2002.

[62] "Field orientated control of 3-phase AC-motors", Texas Instruments Application Note, BPRA073, Feb. 1998.

[63] Novotny, D. W., and Lipo, T. A., *Vector Control and Dynamics of AC Drives*. Oxford Univ. Press, London, U.K., 1996.

[64] Kokotovic, P., Khalil, H. K. and O'Reilly, J., *Singular Perturbation Methods in Control: Analysis and Design*. New York: Academic, 1986.

[65] Slotine, J. J. and Sastry, S. S., "Tracking control of nonlinear systems using sliding surfaces, with application to robot manipulators", Int. Journal of Control, Vol. 38, No. 2, pp. 465-492, 1983.

[66] Slotine, J. J., "Sliding controller design for nonlinear systems", Int. Journal of control, Vol. 40, No. 2, pp. 421-434, 1984.

[67] Yu, Z.Y., Mohammed, A. and Panahi, I., "A review of three PWM techniques", Proceedings of the American Control Conference, pp. 257-261, Jun. 1997.

[68] Perruquetti, W., *et al.*, *Sliding Mode Control in Engineering*. Marcel Dekker, Inc., New York, 2002.

[69] Utkin, V. I. and Chang, H. C., "Sliding mode control on electro-mechanical systems", Mathematical Problems in Engineering, Vol. 8(4-5), pp. 451-473, Taylor & Francis Group, 2002.

[70] *DMC1500 Technical Reference*. 504915-0001 Rev. A, Spectrum Digital, Inc., USA, 2000.

[71] *eZdsp^{TM}F2812 Technical Reference*. 506265-0001 Rev. F, Spectrum Digital, Inc., USA, 2003.

[72] Fu, T. J. and Xie, W. F., "A novel sliding-mode control of induction motor using space vector modulation technique", ISA Transactions on the Instrumentation, Systems, and Automation, Vol. 44, No. 4, 2005.

Appendix A
Experimental Setup

DSP provides high speed, high resolution and sensorless algorithms in order to reduce system costs. In this experimental setup, a scheme of DMC150 digital motor controller with eZdsp^{TM}F2812 card is adopted. A test based on the open loop control system has demonstrated the experimental setup is preferred for induction motor control.

A.1 Overview of the eZdsp^{TM}F2812

The eZdsp^{TM}F2812 produced by Spectrum Digital, Inc., USA is a stand-alone card allowing evaluators to examine the TMS320F2812 DSP developed by Texas Instruments, Inc., USA (TI) to determine if it meets their application requirements. Furthermore, the module is an excellent platform to develop and run software for the TMS320F2812 processor. The TMS320F2812 is a 32-bit fixed-point DSP. It is preferred for motor control since the fixed-point DSP cost much less than the floating-point DSP and if and when needed, the dynamic range can be increased in a fixed-point processor by doing floating-point calculations in software.

To simplify code development and shorten debugging time, a C2000 Tools Code Composer driver is provided. In addition, an onboard JTAG connector provides interface to emulators, operating with other debuggers to provide assembly language and 'C' high level language debug.

The eZdsp^{TM}F2812 has the following features [71]:

- TMS320F2812 DSP
- 150 MIPS operating speed
- 18K words on-chip RAM
- 128K words on-chip Flash memory
- 64K words off-chip SRAM memory
- 30MHz clock
- 2 Expansion connectors (analog, I/O)
- Onboard IEEE 1149.1 JTAG controller
- 5-volt only operation with supplied AC adapter
- TI F28xx Code Composer Studio tools driver
- On board IEEE 1149.1 JTAG emulation connector

A.2 Overview of the DMC1500

The DMC1500 is versatile digital motor controller that allows ones examine certain characteristics of the TMS320F2xxx DSPs to determine the application requirements. Furthermore, the module is a powerful platform to develop and run motor control software for the TMS320F2xxx processors. The DMC1500 uses a Starter Kit (DSK) or eZdsp^{TM} board as the computer engine to run algorithms. The DMC1500 along with a DSK or eZdsp^{TM} allows full speed verification of TMS320F2xxx code.

The DMC1500 has the following features [70]:

- Compatible with the DSKs or eZdsp^{TM} from Spectrum Digital, Inc.
- Allows development of algorithms for the induction, DC Brushless, or SRM motors
- Rated for Bus voltages of 350VDC
- Onboard control power supply (115-230VAC)
- Onboard bus supply (Bridge + Capacitors + Voltage doubler)
- Optically isolated digital I/O
- Optically isolated RS-232 port

- Optically isolated CAN interface
- Onboard Power Factor Correction Logic

A.3 Experimental setup

Figure A.1 shows the experimental setup and connection. Some key points should be considered in the experimental setup.

1) The isolated transformer is very important in the experimental setup. It isolates the neutral point of the power supply and the common points of the DSP board. Without it, the DSP board can be damaged.

2) The input power must be fused externally for safe operation. The fuse should be sized to the voltage and current requirements of the load.

3) The DMC1500 has 12 test points. A scope should not be tie to ground unless an isolated transformer is used for Bus power.

4) The eZdsp should be powered up first and powered down last to prevent latch-up conditions.

5) The TMS320F2812 supports +3.3V Input/Output levels which are not +5V tolerant. Connecting the eZdsp to a system with +5V Input/Output levels will damage the DSP board.

6) If the motor is being operating in the regenerative braking situation, a voltage regulator must be put across the Bus terminals to absorb the energy. Otherwise the bus voltage may rise above the maximum voltage and destroy the inverter board.

7) There is not only one selection for the power supply of DMC1500. But when the 220V is selected, the voltage doubler must not be used. Otherwise the DC bus voltage will exceed the maximum value.

8) The operation steps of stopping the motor are: reducing voltage at variac to zero, and then halt or stop the program.

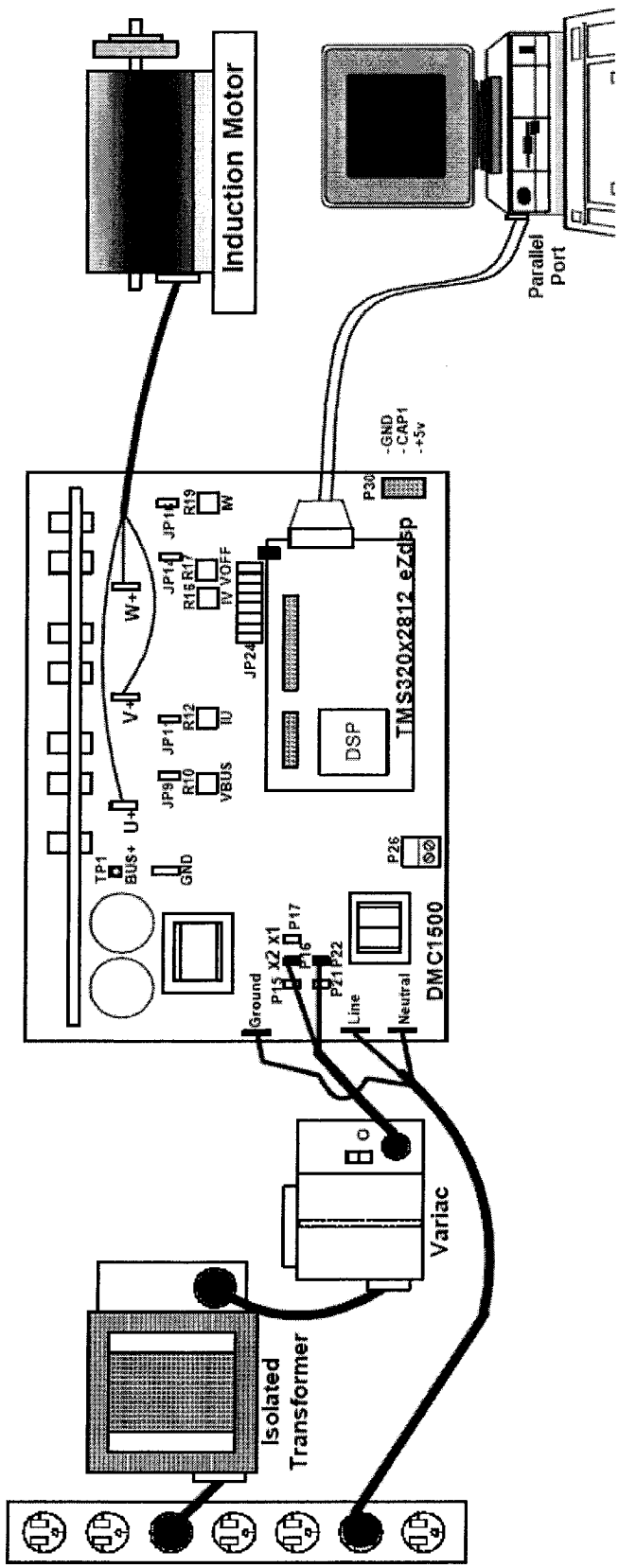

Figure A.1: Experimental setup and connection

A.4 Test results

The experimental setup has been shown in Figure 7.1 and Figure 7.2. The isolated transformer is a 120/37V transformer. The input/output voltages of variac are 120/(0-140V). The power supply is single-phase 120VAC. The nameplate data of induction motor are listed in Table A.1.

Table A.1: Nameplate data of induction motor

Tamper AC motor	
H.P.: 1/3HP	R.P.M.: 3450rpm
V.: 220V	PH.: 3
CYC.: 60Hz	0.62A
RATING: CONT.	CODE: 6511
TYPE: K-4499A	D. P.: ENCL.
MOD.: HFD-H56R-HSF-BP733-K2	

The test block diagram of open-loop system is shown in Figure A.2.

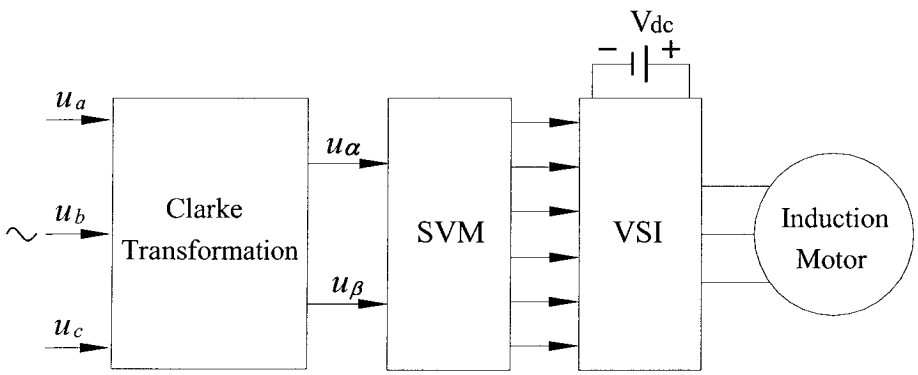

Figure A.2: Test block diagram of open-loop system

The reference inputs are 110V 20Hz three-phase balance sinusoidal signals. A 10-kHz sampling frequency for the control system is selected.

A.4.1 Logic switching signals for the inverter

The logic switching signals for the inverter are shown in Figure A.3.

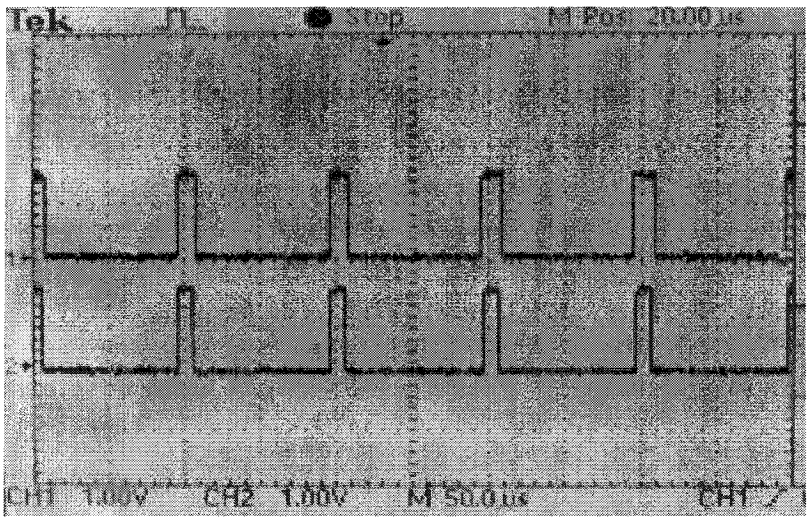

(a)

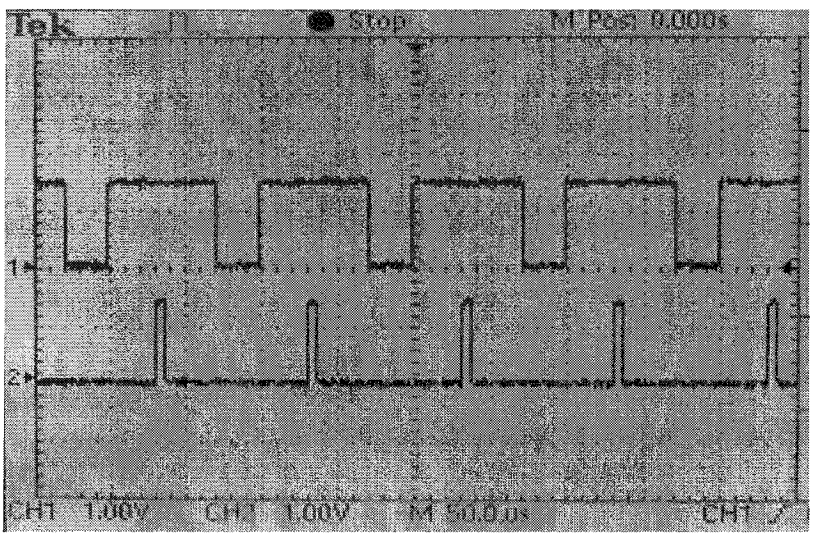

(b)

Figure A.3: Logic switching signals for the inverter (a) PWM1 and PWM3 (b) PWM5 and PWM3

A.4.2 V sense voltages of the inverter

It is difficult to obtain waves of the motor's phase voltage by an oscilloscope since the neutral point of the motor is connected inside for a star-connection motor. Instead the wave of V sense voltage is tested for the real case. The V sense voltage is the voltage of the top transistor with respect to Bus-. (For details, see the circuit schematics in [70]). It equals pole voltage plus the half of DC link voltage ($u_{sei} = u_{Li} + V_{dc}/2$, i=1, 2, 3). In DMC1500 board, the V sense voltage is divided by a resistive divider consisting of 400 $k\Omega$ and 4.99 $k\Omega$ for the purpose of A/D converting. This gives a division of 81. Each channel also contains a filter with a cutoff frequency of 3.2kHz. In this experiment, the tested voltages are obtained from the A/D ports of DMC1500. The maximum voltage is set as 170V for the calculation of the gain and the adjustment of the potentiometers [70]. The V sense voltages are adjusted to 0-3.3V to meet the requirement of input voltages of the A/D. The V sense voltages of the inverter are shown in Figure A.4.

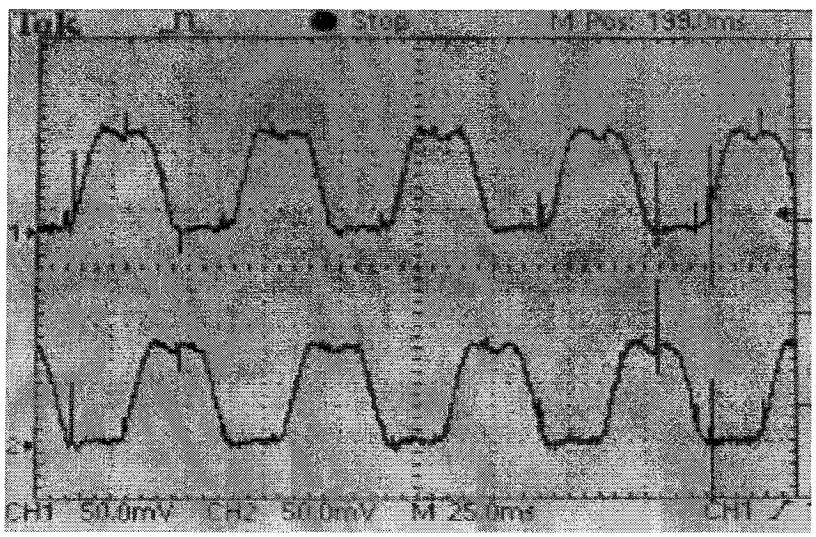

(a)

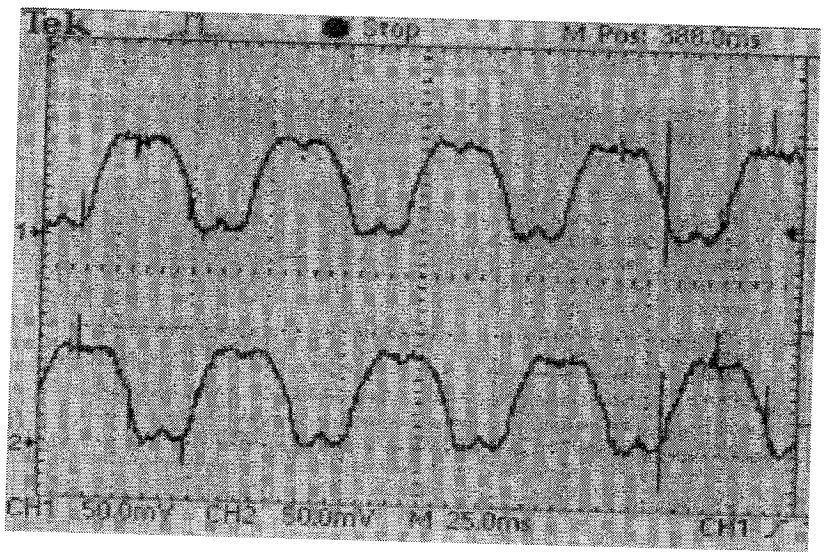

(b)

Figure A.4: V sense voltages of the inverter (a) Phase a and Phase b (b) Phase a and Phase c

A.4.3 Phase currents of the motor

The DMC1500 supports reading the phase current in the lower transistor leg. The currents are measured across three $0.04\,\Omega$ resistors. These sense signals are then filtered for a 40kHz cutoff frequency, clamped to the rails and applied to the non inverting input to an op-amplifier. In this experiment, the tested phase currents are also obtained from the A/D ports of DMC1500. The bipolar current measurements are chosen and the maximum current is chosen as $\pm 3.5A$ for the calculation of the gain and the adjustment of the potentiometers [70]. The phase currents have been adjusted to 0-3.3V to meet the requirement of input voltages of the A/D, i.e., -3.5A corresponds to 0V, and 3.5A corresponds to 3V. The phase current waveforms of the motor obtained from A/D ports of DMC1500 are shown in Figure A.5.

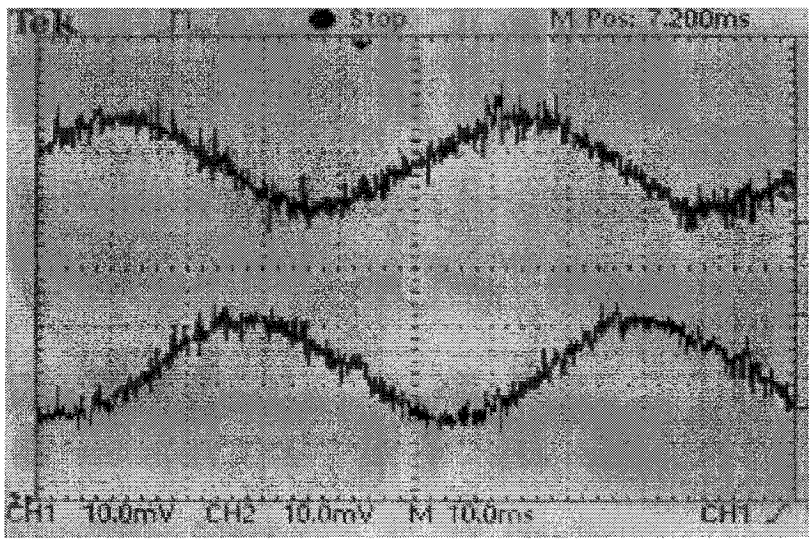

(a)

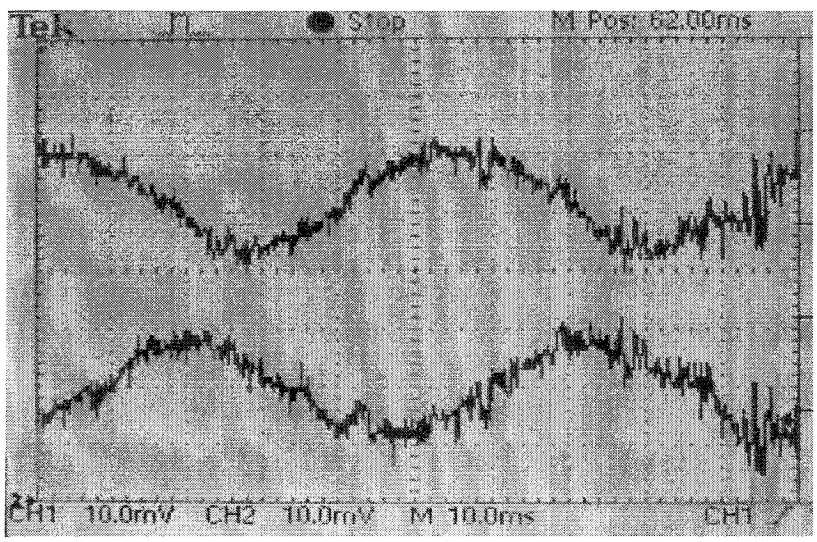

(b)

Figure A.5: Phase current waveforms of the motor (a) Phase *a* and Phase *b* (b) Phase *a* and Phase *c*